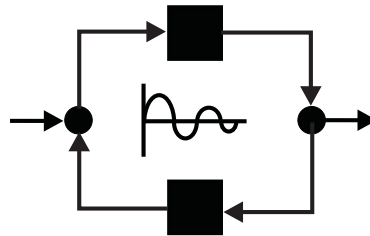


The International Congress for global Science and Technology



***ICGST International Journal on Automatic
Control & System Engineering
(ACSE)***

***Volume (14), Issue (II)
December 2014***

***www.icgst.com
www.icgst-amc.com
www.icgst-ees.com***

***© ICGST LLC, 2014
Delaware, USA***

ACSE Journal
ISSN: Print 1687-4811
ISSN Online 1687-482X
ISSN CD-ROM 1687-4838
© ICGST LLC, 2014, Delaware, USA

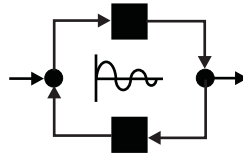
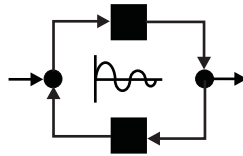


Table of Contents

Papers	Pages
P1111410320, Simon O. Omekanda and Todd Perkins and Mohamed A. Zohdy, "Robustness Analysis of Linear Time-Invariant Dynamic State Observers",	1--8
P1111351312, N.SambaSivaRao and J.Amarnath and V.PurnaChandrarao, "Comparison of Voltage Stability Using FACTS Devices in Deregulated Power System",	9--16
P1111431335, Sridevi Tirunagari and Ramesh Reddy Kolli, "Suppression & Comparison of Magnetizing Current of a Transformer with PWM Voltage Source Converter",	17--23
P1111438344, T. A. Perkins and M.A. Zohdy, "Nonlinear State Control Optimized by Lyapunov and Riccati via Piecewise Linear Transformations Applied to Transmission Torque Converter Clutches",	25--33
P1111440346, P Srinath Rajesh and J Amarnath, "Dynamics of Metallic Particle movement in a Gas Insulated Substation Employing SF6/N2, SF6/CO2 and SF6/Air Dielectric Gas Mixtures ",	35--41
P1111444352, Jala M. El-Azab and Hamed M. Kandel and Mohamed A. Khedr , "Numerical Study of Auto-Control and Stabilization of Pulse Repetition Rate of Passively Q-Switched Laser Systems",	43--52



***ICGST International Journal on Automatic Control & System Engineering -
(ACSE)***

***A Publication of the International Congress for global Science and Technology -
(ICGST)***

ICGST Editor in Chief: Dr. rer. nat. Ashraf Aboshosha

www.icgst.com, www.icgst-amc.com, www.icgst-ees.com

editor@icgst.com



Robustness Analysis of Linear Time-Invariant Dynamic State Observers

S.O. Omekanda*, T. Perkins**, M.A. Zohdy***

**Department of Electrical and Computer Engineering, Oakland University, Rochester, Michigan, U.S.A.*

somekand@oakland.edu, taperk@oakland.edu**, zohdyma@oakland.edu****

http://www.oakland.edu/ece

Abstract

In this paper, we investigate the effect of state and measurement variations on linear time-invariant state (LTI) observers' performance robustness and error dynamics. These observers are widely used in control engineering, and, more recently, modern automotive powertrain applications. Their approach is analogous to Kalman Filters except that the perturbations are deterministic as opposed to stochastic. They have a proven and well documented degree of reliability and efficiency in the approximation of systems' states. When well designed, they exhibit negligible steady state errors. In this study, we apply observer theory to an internal combustion engine (ICE) model. We also investigated state and sensor measurement disturbances that occur during common operation of the system. An analysis of the change in the observer error dynamics, and subsequent performance robustness is presented.

Keywords: *Linear observers; Control theory; Internal combustion engines modeling; State disturbance; Sensor disturbance; Estimation methods.*

1. Introduction

There has been much work done on LTI state observers and their results are well known in control engineering. The concept was first introduced by Luenberger in 1971 [1]. Observers were presented both for the continuous and discrete-time cases. Since then, state observers have revolutionized control theory by enabling the approximation of the state vector using readily available measurements of the system's outputs. These outputs come directly from measurements. In some systems however, not all of the state variables can be easily observed through direct measurement. In such cases, costly measurement devices might also be needed to measure these states. In other systems, some of the state variables may be inaccessible for direct measurement. For the aforementioned cases, a state observer provides a good solution by approximating the states for which information would otherwise not be available. This makes the state observer inherently invaluable as a

model-based method for state-feedback control of any control system. In the four decades following the introduction of the LTI state observer methodology, its use has been extended through various disciplines of engineering, including computer-aided software design and has been utilized in modern control structures to implement state observers in the manner depicted in Fig. 1.

One of the recent fields that has been a beneficiary of the state observer is automotive powertrain. Specifically, we discuss its impact on ICE powertrain control. It is widely known that due to government mandates modern ICEs will have to improve their fuel efficiency and decrease their emissions if they are to remain the primary propulsion source [2]. As a result, new technologies, such as 'engine start-stop', and more modern control strategies, such as advanced idle-speed control schemes (ISC), have been employed [3-4]. The more popular method to solving efficiency issues has been to utilize the wealth of knowledge and proven effectiveness of model-based methods, which use state observers [5-11].

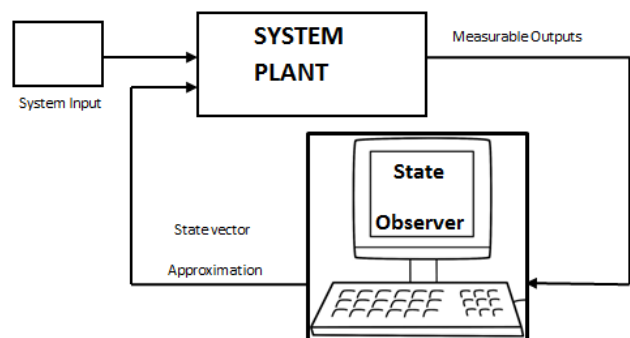


Figure 1: State observer feedback loop flow diagram

The long established method of model-based controllers in the automotive industry to achieve fuel savings through better idle speed control (ISC) was first pioneered by Hrovate [12] in the mid 1990s. Around the same time, Zohdy and Karam began using optimal control to develop a more robust controller that addresses



the influences of the unmolded dynamics of ICS [13]. These unmolded dynamics include measurement noise, external disturbances, transient loads and model inaccuracies. To address these, the control community has developed methods such as Adaptive Controllers [14], nonlinear adaptive Fuzzy Logic [15], and Kalman filter [16] controllers. Kalman filters are most often used due to their inherent ability to deal with noise [17-18]. They have shown great success in many applications [19-23]. However, they are limited in many areas where the assumption that the noise has Gaussian distribution does not hold. Also, Kalman filters can be computationally complex to implement. Adaptive control schemes are limited by their need for high-fidelity models running in multi kHz switching frequency range and by the fact that they are highly nonlinear. These limitations have kept them out of the automotive market.

One solution is the lower order, robust, linear time-invariant state observer model addressed in this paper which is computationally efficient enough to run in real-time in typical powertrain control modules (PCM). State observers are attractive in control schemes because they enable linear control schemes to be implemented on nonlinear systems. Unlike nonlinear control schemes, linear control schemes do not demand powerful processors; therefore, they minimize computational delays. While observer theory is well known in the literature, observers performance under non-ideal conditions and disturbance hasn't been fully investigated. In this work, we include the influence of variations due to inaccuracies in the state space model and include measurement errors due to sensor errors. Model state disturbances and sensor measurement disturbances are investigated by analyzing their effects on observer error dynamics and overall state observer performance. Observer model designed to estimate the system states will be discussed in Section 2 and specifically applied to an internal combustion engine (ICE) model as introduced in [24] in Section 3. The results and explicit analysis of the findings are provided in Section 4 with our conclusion in Section 5.

2. Observer Model

In this section, a thorough derivation of the LTI state observer error dynamics is presented. The state observer is designed in order to reconstruct the states of a linear system [25-26]. The state space representation of the system includes the state and output equations, respectively presented in (1-2),

$$\dot{x}(t) = Ax(t) + Bu(t) + d \quad (1)$$

$$y(t) = Cx(t) + \eta \quad (2)$$

where x is the state vector of dimensions $n \times n$ and y is the output vector of dimension $m \times n$. The number of states in the state vector and output are denoted by n and m , respectively. The constant state, input and output matrices of appropriate dimensions are denoted by A , B and C , respectively. The input u has dimensions $r \times 1$, where r is the number of inputs to the system. This state space system includes the effect of the state disturbance,

d , and sensor (output) noise, η . This is very similar to the state space model a Kalman filter would be applied to [27-28]. The effect of variations is of interest in this work and is represented in the model. The state space model mathematically demonstrates that dynamic changes in the state vector are affected by its current values at some time, t , the system's input and disturbances on the state vector itself. The outputs of the system are measurements from the state vector, which take the errors of the measuring device into account.

The state observer model is very similar to the state space model presented in (1-2) and is shown in (3-4).

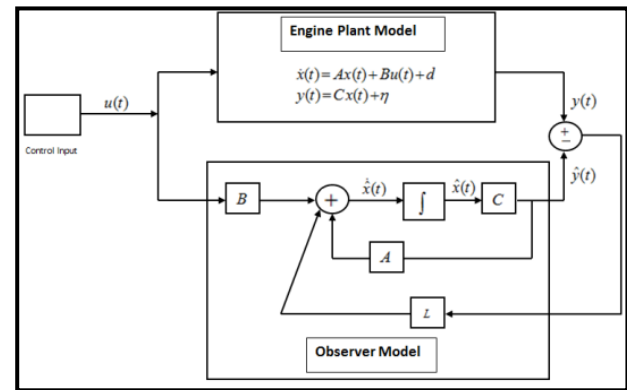
$$\dot{\hat{x}}(t) = A\hat{x}(t) + Bu(t) + L(y(t) - \hat{y}(t)) \quad (3)$$

$$\hat{y}(t) = C\hat{x}(t) \quad (4)$$

where $\hat{x}(t)$ denotes the estimate of the state vector and $\hat{y}(t)$ is the estimated output of the state observer model, which is comprised of the estimated state vector. It is easy to see that the observer state equation in (3) differs from (1) because the observer gain, L , is used as a correction term for the output error ($y(t) - \hat{y}(t)$). One can notice that if the output error $y(t) - \hat{y}(t)$ is very small, then (3) and (1) are identical. However, if the output error is large, then L is used to correct the error in a way that will drive the overall state observer error dynamics to zero.

There are well known methods to determine the observer gain, most notably the pole placement method [29-30] and the Linear Quadratic Regulator (LQR) method [31]. A block diagram of the state observer system is shown in Fig. 2. The state observer performance is determined by the error dynamics of the observer. A well designed observer has error dynamics that converge to zero quickly. How quickly depends on the criteria of the observer application.

Figure 2: Block Diagram of state observer system



The state observer error dynamics are derived as follows,

$$e(t) = x(t) - \hat{x}(t) \quad (5)$$

$$\dot{e}(t) = \dot{x}(t) - \dot{\hat{x}}(t) \quad (6)$$

$$\dot{e}(t) = (Ax(t) + Bu(t) + d) - (A\hat{x}(t) + Bu(t) + L(Cx(t) + \eta - C\hat{x}(t))) \quad (7)$$

$$\dot{e}(t) = Ax(t) + Bu(t) + d - A\hat{x}(t) - Bu(t) - LCx(t) - L\eta + LC\hat{x}(t) \quad (8)$$

$$\dot{e}(t) = (A - LC)(x(t) - \hat{x}(t)) + d - L\eta \quad (9)$$

$$\dot{e}(t) = (A - LC)e(t) + d - L\eta \quad (10)$$



where (10) is the LTI state observer error dynamics. Our aim is to look at the effect variations of \hat{d} and η have on the observer error dynamics and overall observer performance.

3. Internal Combustion Engine

The model used for the state observer error dynamics analysis is similar to the one presented by C.E. Baumgartner et al. in [24], where it was created and first implemented for ISC of the Dodge Neon (ICE). The model represents the intake dynamics of the engine in order to use engine speed to control idling mode. The initial model had three inputs and three states. Later, the model was modified by Omekanda and Zohdy in their work published to this publication [32]. It was reduced to only one input for simplicity and used for the design of a reduced order observer. The latter model is used here, with the input $u(t)$ and the state vector $x(t)=[x_1(t) \ x_2(t) \ x_3(t)]$ seen in Table 1.

Table 1: Input and State vector

$u(t)$:	Commanded Throttle Angle (degrees)
$x_1(t)$:	Throttle angle (degrees)
$x_2(t)$:	Intake manifold Pressure (Torr)
$x_3(t)$:	Engine speed (RPM)

It has been modified in such a way that an open loop throttle request of 7 degrees commands an idle speed of 680 RPM. The state space of the ICE is presented as,

$$\dot{x}(t) = \begin{bmatrix} -35 & 0 & 0 \\ 4.212 & -3.822 & -6.552 \\ 0 & 3.2 & 1.84 \end{bmatrix} x(t) + \begin{bmatrix} 35 \\ 0 \\ 0 \end{bmatrix} u(t) \quad (11)$$

$$y(t) = [0 \ 0 \ 1] x(t) + \eta \quad (12)$$

An LTI state observer was designed for this ICE model when no state and measurement noise are taken into account. The gain, L, for this system was determined using the pole placement method. Figure 3 depicts the observer state approximation of the system states. Figure 4 shows the state observer dynamics. The state observer has great dynamics, which converge very quickly and have no steady state error. During most of the first second of simulation, it appears that the intake manifold pressure is positive. Knowing this is physically impossible for a naturally aspirated ICE, we attribute this to a reduced order non bounded mathematical modeling error, resulting from an extremely transient step input of the original system of equations.

To determine the model's robustness and to evaluate the performance and effect on error dynamics, this paper will evaluate the ICE model's response to measurement and modeling disturbance, often called error-in-variables (EIV). Much has been written on the difficulty of designing controllers to address EIV [33-35]. This leads to the belief that prior knowledge of states and several assumptions about the system must be made to control a system laden with EIVs [36-37]. These solutions are

often too computationally complex to implement within the limitations of an automobile PCM. Our approach to the EIV problem is to design a computationally efficient controller robust enough to operate with error variations. Thus, we reduce the need to make assumptions about noise and make the controller more implementable in a modern PCM. In order to look into the effect of disturbance, \hat{d} is assumed to be a random disturbance on the state that could be caused by faults or other unexpected variations. The output of the model is engine speed, and we depict sensor measurement disturbance as η .

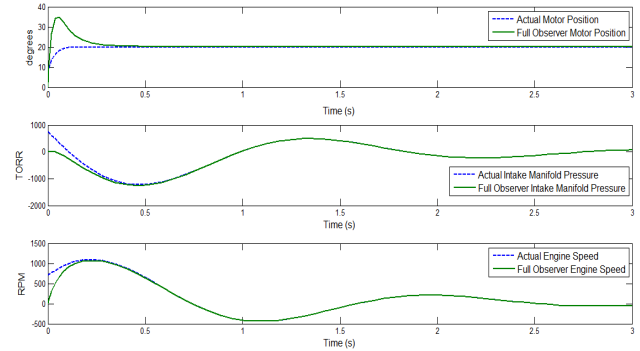


Figure 3: State Observer approximation of the ICE system with no disturbance

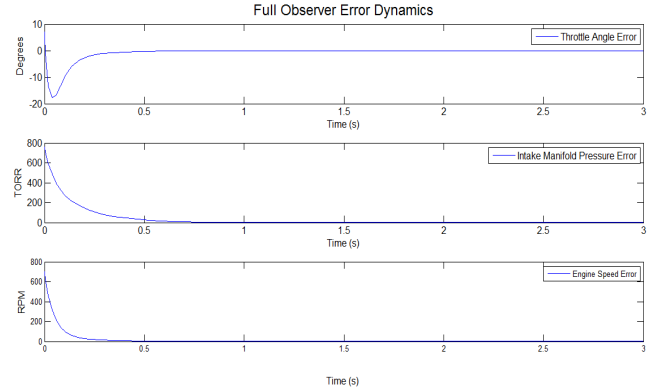


Figure 4: State observer error dynamics

4. Results and Analysis

The state disturbance is quantified as an assumed random disturbance bounded by a percent error (+/-) of the actual state (throttle angle, manifold pressure and engine speed), while the measurement disturbance is bounded by a percent error (+/-) of the engine speed sensor measurement. We first examined the effect of the state disturbance, \hat{d} , and the measurement disturbance, η , by themselves, on the observer error dynamics and state observer performance. Then, we mixed different amounts of state and measurement disturbances and analyzed the resulting effects. The disturbances used for the singular disturbance tests and their results are shown in Table 2 below.



Table 2: Tests points for Figure 5 (a-d)

Measurement Disturbance (η) %	State Disturbance (d) %
0	2
0	2
0	10
0	15
2	0
5	0
10	0
15	0

Figures 5 (a-d) shows state observer error dynamics behavior caused by varying the state disturbance on the system by $\pm 2, 5, 10$ and 15% , respectively. There is no measurement disturbance assumed present in these tests. This means that engine speed measurements from the plant (ICE) used by the state observer to estimate the state vector are not corrupted. One should notice right away that the intake manifold pressure and engine speed have been scaled by a factor of 100. This was done to more easily demonstrate the instantaneous state and measurement disturbance included in the plots. It is immediately visible that the state observer is very sensitive to state disturbance. This is expected because an observer is a model-based method, which relies on an accurate model of the system to approximate the state vector. To account for state disturbance, we could adjust the gain in order to correct the error dynamics. Such methods have been implemented in literature by using gain scheduling schemes [38-45]. But in this study, we chose to leave the gains constant to illustrate the effects of the noise on the system response. As the state disturbance increased, the state observer error was unable to converge, and the oscillations and instability of the dynamics increased. In figure. 5a, the states try to converge but the observer seems to be marginally working. This means that it keeps the error within a bounded error range but never converges to zero or lost control. The throttle angle is the least affected by the 2% state disturbance. However, by figure. 5d the observer loses all controllability and the oscillations are as high as ~ 10 degrees, ~ 2000 Torr and ~ 2000 RPM for the throttle angle, manifold pressure and engine speed, respectively.

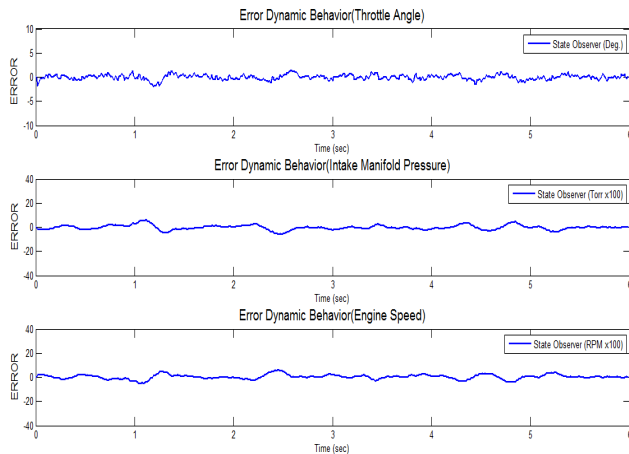


Figure 5a: 2% state disturbance

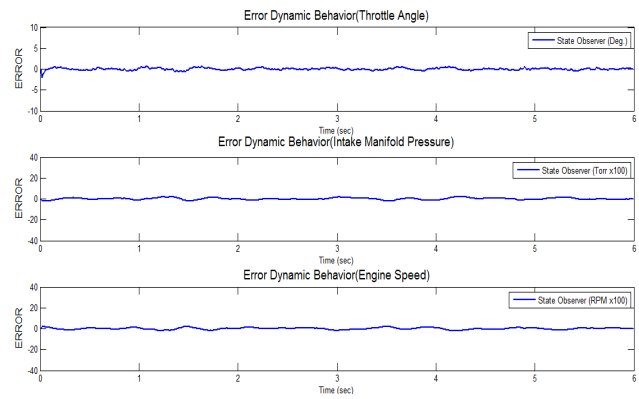


Figure 5b: 5% state disturbance

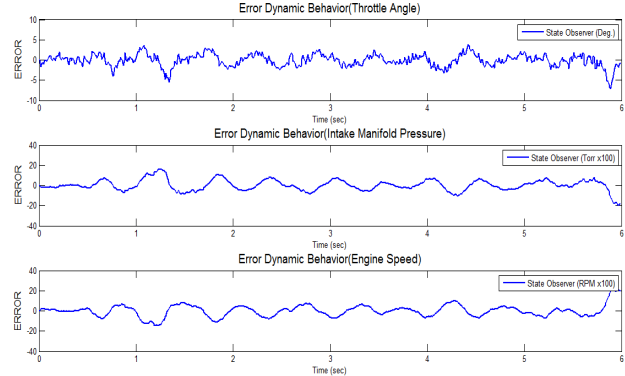


Figure 5c: 10% state disturbance

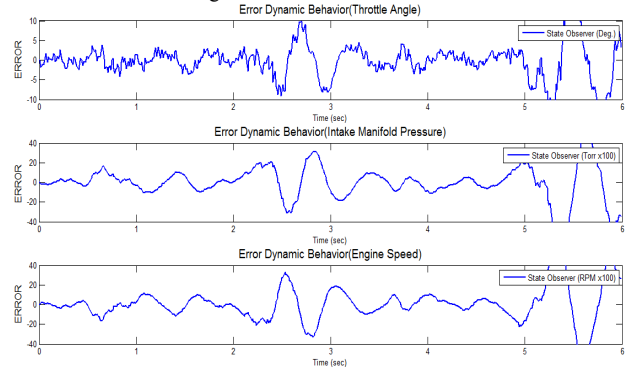


Figure 5d: 15% state disturbance

In the next set of tests, no state disturbance was input into the system. Rather, the effect of measurement disturbance was analyzed. Our measurement disturbance was applied to the speed sensor, which is our output signal. Figure 6 (a-d) depict the error dynamics performance of each test when the measurement error on the speed was varied from $\pm 2, 5, 10$ and 15% , respectively. Compared to the effect of state disturbance only, the measurement disturbance seems to be less sensitive. This is evident in the lesser bounded oscillations at each disturbance percentage in comparison to those of Figure 5 (a-d). Here, the throttle angle approximation again seems to be the least sensitive to the disturbance.

In Figure. 6a, the error converges and only oscillates about zero during certain ranges of operation. Even in Figure. 6b, small oscillations are evident and start to have larger bounds on the oscillations. From Figure. 6c to



Figure. 6d, the error bounds for the oscillations barely demonstrate change. With greater than 5% measurement disturbance, the error dynamics become uncontrollable bounded by a certain error bound.

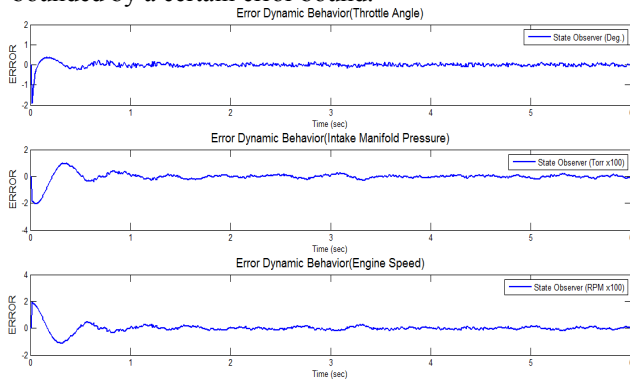


Figure 6a: 2% measurement disturbance

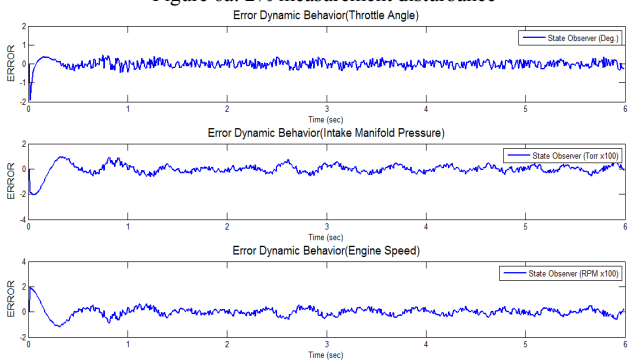


Figure 6b: 5% measurement disturbance

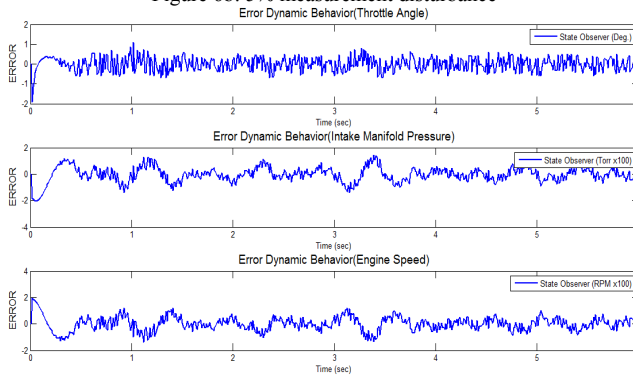


Figure 6c: 10% measurement disturbance

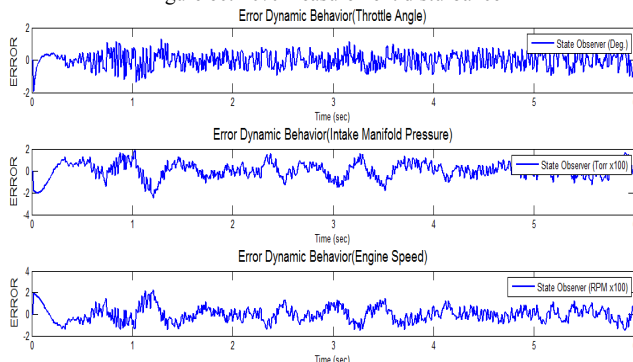


Figure 6d: 15% measurement disturbance

A final set of conditions was when both measurement disturbance and state disturbance were introduced to the

system together. Table three shows 4 points that were investigated.

Table 3: Tests points for Figure 6 (a-d)

Measurement Disturbance(η) %	State Disturbance (d) %
2	2
5	5
10	10
15	15

Through casual observations, one can see that these results are very similar to the state only classification of disturbances. These results confirm earlier findings that the system is much less sensitive, to an order of 10 magnitudes, to measurement noise than state disturbance. Further analysis of these results was achieved by repeating the test with different sets of random noise. By capturing and comparing the state error between tests, it was shown that the relationship of the two statistically independent disturbances has a causal effect of the state observer. The variance of the state observer error was greater that with state disturbances alone, indicating that the two disturbances interacted to randomly increase or decrease their combined effect on the state error. The results of one of these random simulations are shown in figure 7.

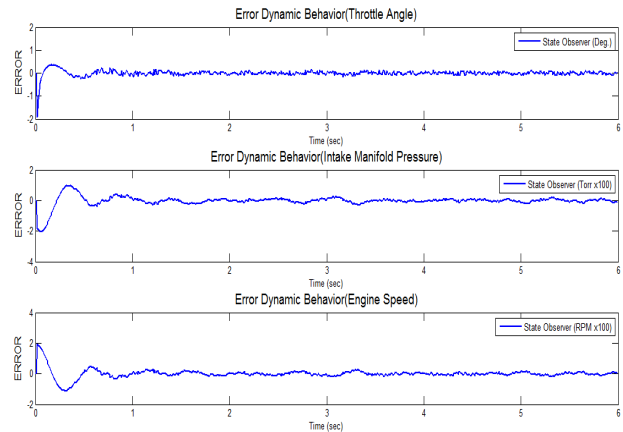


Figure 7a: 2% state and measurement disturbance

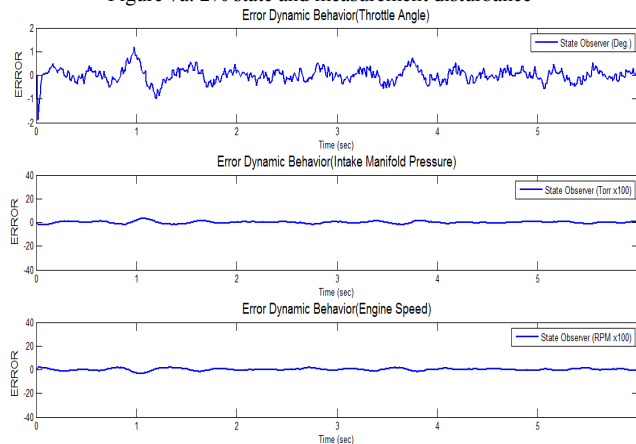


Figure 7b: 5% state and measurement disturbance



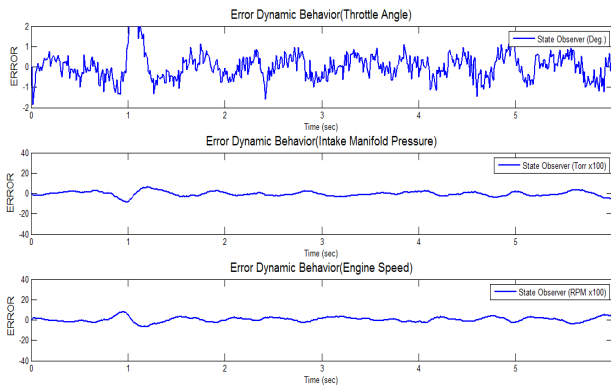


Figure 7c: 10% state and measurement disturbance

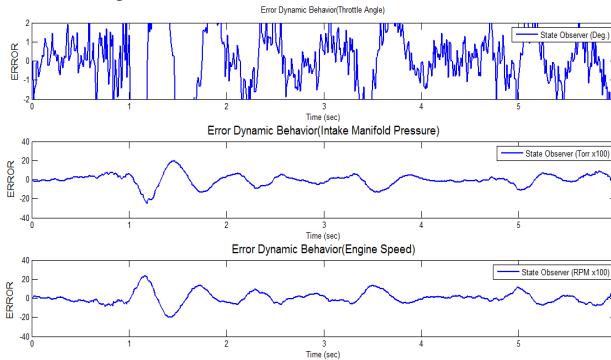


Figure 7d: 15% state and measurement disturbance

5. Conclusion

Our results demonstrate that state observers are very sensitive and susceptible to disturbance. This is in large part due to the fact that, unlike the Kalman filter, state observers do not take into account possible disturbances in their algorithm. On the contrary, any disturbance in the system directly affects the observer. However, state observers, as we demonstrated, are great state approximation tools for any system. In practice, they continue to be utilized because the control of systems is not based solely on the observed state(s) but also on the other sensor measurements and state observer approximations to control systems. Moreover, state observers are often used in steady state conditions where any disturbance is dampened or filtered by the system after transient conditions have been addressed. Measurement disturbance can be reduced and accounted for with the use of a reliable sensor with proven durability and low error range. With these system improvements the engine speed approximation can be ensured to stay within the desired percentage of the idle RPM that is considered the industry range for allowable speed deviations of ISC. Our work shows how state and measurement disturbance affects the error dynamics of a LTI state observer. Through simulation, we identified the effect of these disturbances and provided a thorough analysis of our findings.

References

- [1] D. Luenberger, "An Introduction to Observers," *Automatic Control*, IEEE Transactions on, vol. 16, pp. 596-602, 1971.
- [2] (August 2012). EPA and NHTSA Set Standards to Reduce Greenhouse Gases and Improve Fuel Economy for Model Years 2017-2025 Cars and Light Trucks. Available: <http://www.epa.gov/OTAQ/climate/documents/420f12051.pdf>.
- [3] C. Silva, M. Ross and T. Farias, "Analysis and simulation of "low-cost" strategies to reduce fuel consumption and emissions in conventional gasoline light-duty vehicles," *Energy Conversion and Management*, vol. 50, pp. 215-222, 2, 2009.
- [4] S. Di Cairano, D. Yanakiev, A. Bemporad, I. V. Kolmanovsky and D. Hrovat, "Model Predictive Idle Speed Control: Design, Analysis, and Experimental Evaluation," *IEEE Trans. Control Syst. Technol.*, vol. 20, pp. 84-97, Jan, 2012.
- [5] J. H. Buckland, J. Freudenberg, J. W. Grizzle and M. Jankovic, "Practical observers for unmeasured states in turbocharged gasoline engines," in *American Control Conference*, 2009. ACC '09. 2009, pp. 2714-2719.
- [6] Derong Tan, Zeyan Liu and Jihua Wang, "Study on optimum estimate method for gasoline engine intake flowrate based on state observer," in *Intelligent Control and Automation*, 2006. WCICA 2006. the Sixth World Congress on, 2006, pp. 4734-4737.
- [7] Hansheng Wu, "Adaptive Robust State Observers for a Class of Uncertain Nonlinear Dynamical Systems With Delayed State Perturbations," *Automatic Control*, IEEE Transactions on, vol. 54, pp. 1407-1412, 2009.
- [8] E. Hendricks, J. Poulsen, M. B. Olsen, P. B. Jensen, M. Fons and C. Jepsen, "Alternative observers for SI engine air/fuel ratio control," in *Decision and Control*, 1996., Proceedings of the 35th IEEE Conference on, 1996, pp. 2806-2811 vol.3.
- [9] S. Ibaraki, S. Suryanarayanan and M. Tomizuka, " H_{∞} optimization of luenberger state observers and its application to fault detection filter design," in *Decision and Control*, 2001. Proceedings of the 40th IEEE Conference on, 2001, pp. 1011-1016 vol.2.
- [10] Ling-Yuan Hsu and Tsung-Lin Chen, "Vehicle Full-State Estimation and Prediction System Using State Observers," *Vehicular Technology*, IEEE Transactions on, vol. 58, pp. 2651-2662, 2009.
- [11] G. Rizzoni, S. Drakunov and Yue-Yun Wang, "On-line estimation of indicated torque in IC engines via sliding mode observers," in *American Control Conference*, Proceedings of the 1995, 1995, pp. 2123-2127 vol.3.
- [12] D. Hrovat, "MPC-based idle speed control for IC engine," in *Prague*, Czech Republic, 1996.
- [13] M. A. Zohdy and M. Karam, "Idle speed engine optimal control" Center for Robotics and Advanced Automation, Electrical and Systems Engineering, Oakland University, May 1996.
- [14] Y. Yildiz, A. M. Annaswamy, D. Yanakiev and I. Kolmanovsky, "Spark-Ignition-Engine Idle Speed Control: An Adaptive Control Approach," *IEEE*



- Trans. Control Syst. Technol., vol. 19, pp. 990-1002, 2011.
- [15] M. Thornhill, S. Thompson and H. Sindano, "A comparison of idle speed control schemes," *Control Eng. Pract.*, vol. 8, pp. 519-530, 2000.
- [16] D. Pavkovic, J. Deur and I. Kolmanovsky, "Adaptive Kalman Filter-Based Load Torque Compensator for Improved SI Engine Idle Speed Control," *IEEE Trans. Control Syst. Technol.*, vol. 17, pp. 98-110, JAN, 2009.
- [17] Kalman, R.E. and Bucy, R.S., "New Results in Linear Filtering and Prediction Theory," *Journal of Basic Engineering*, vol. 1, pp. 95-108, 1961.
- [18] R. E. Kalman, "A New approach to Linear Filtering and Prediction Problem," vol. No.82 (Series D), pp. 35-45, 1960.
- [19] S. Bolognani, R. Oboe and M. Zigliotto, "DSP-based extended kalman filter estimation of speed and rotor position of a PM synchronous motor," in *Industrial Electronics, Control and Instrumentation, 1994. IECON '94.*, 20th International Conference on, 1994, pp. 2097-2102 vol.3.
- [20] N. Meskin, H. Nounou, M. Nounou, A. Datta and E. R. Dougherty, "Parameter estimation of biological phenomena modeled by S-systems: An extended kalman filter approach," in *Decision and Control and European Control Conference (CDC-ECC), 2011 50th IEEE Conference on*, 2011, pp. 4424-4429.
- [21] R. Panigrahi, S. Rauta and P. C. Panda, "Robust extended complex kalman filter applied to distorted power system signals for frequency estimation," in *Power Systems, 2009. ICPS '09. International Conference on*, 2009, pp. 1-6.
- [22] K. Reif, S. Gunther, E. Yaz and R. Unbehauen, "Stochastic stability of the discrete-time extended Kalman filter," *Automatic Control, IEEE Transactions on*, vol. 44, pp. 714-728, 1999.
- [23] S. Omekanda, J. Omekanda, H. Abdel-Aty-Zohdy and M. Zohdy, "Use of the extended kalman filter for biological models accuracy," in *Circuits and Systems (MWSCAS), 2013 IEEE 56th International Midwest Symposium on*, 2013, pp. 608-611.
- [24] C.E. Baumgartner, H.P. Geering, C.H. Onder and E. Shafal, "Robust Multivariable Idle Speed Control," *American Control Conference (ACC)*, pp. 258-265, June 1986.
- [25] K. Ogata, "Modern Control Engineering," Prentice Hall, Upper Saddle River, New Jersey, 2010.
- [26] T. Kailath, "Linear Systems," Prentice-Hall, Englewood Cliffs, New Jersey, 1980.
- [27] N. K. Sinha, *Control Systems*. New York: Holt, Rinehart & Winston, 1986.
- [28] Shinnars, S.M., *Modern Control System Theory and Design*. New York: Wiley, 1992.
- [29] S. Omekanda, J. Omekanda, H. Abdel-Aty-Zohdy and M. Zohdy, "Use of the extended kalman filter for biological models accuracy," in *Circuits and Systems (MWSCAS), 2013 IEEE 56th International Midwest Symposium on*, 2013, pp. 608-611.
- [30] R. E. Kalman, "A New approach to Linear Filtering and Prediction Problem," vol. No.82 (Series D), pp. 35-45, 1960.
- [31] P. Dorato, C. Abdallah and V. Cerone, "Linear-Quadratic Control, An Introduction," Prentice Hall, Englewood Cliffs, New Jersey, 1995.
- [32] S. Omekanda and M.A. Zohdy, "An Efficient Novel Reduced Order Observer for State Estimation of an Internal Combustion Engine", *ICGST Journal of Automatic Control and Systems Engineering*, 2014.
- [33] H. Hjalmarsson, J. Mrtensson, C. R. Rojas, T. Söderström, Skolan för elektro- och systemteknik (EES), Centra, KTH, ACCESS Linnaeus Centre and Reglerteknik, "On the accuracy in errors-in-variables identification compared to prediction-error identification," *Automatica*, vol. 47, pp. 2704-2712, 2011.
- [34] J. C. Agüero and G. C. Goodwin, "Identifiability of errors in variables dynamic systems," *Automatica*, vol. 44, pp. 371-382, 2, 2008.
- [35] T. Söderström, "A generalized instrumental variable estimation method for errors-in-variables identification problems," *Automatica*, vol. 47, pp. 1656-1666, 8, 2011.
- [36] B. D. O. Anderson, "Identification of scalar errors-in-variables models with dynamics," *Automatica*, vol. 21, pp. 709-716, 11, 1985.
- [37] T. Söderström, "Errors-in-variables methods in system identification," *Automatica*, vol. 43, pp. 939-958, 6, 2007.
- [38] T. Söderström, M. Hong, J. Schoukens and R. Pintelon, "Accuracy analysis of time domain maximum likelihood method and sample maximum likelihood method for errors-in-variables and output error identification," *Automatica*, vol. 46, pp. 721-727, 4, 2010.
- [39] S.O. Omekanda and M.A. Zohdy, "Application of Extended Observer with Gain Scheduling Control to Internal Combustion Engine Model," *Journal of Automation and Systems Engineering*, vol. 6, pp. 149-163, 2012.
- [40] W.E. Leithead and D. J. Leith, "Survey of Gain-Scheduling Analysis and Design," *International Journal of Control*, Vol. 73, Issue 11, pp. 1001-1025, 2000.
- [41] A. Kwiatkowski et al., "Application of LPV Gain Scheduling to Charge Control of a SI Engine," *IEEE International Symposium on Intelligent Control*, Oct. 2006, pp. 2327-2331.
- [42] Nohra et al., "A Nonlinear Approach with Gain Schedule Control Adaptation for a Complete-Model Diesel-Engine Diagnosis," *3rd International Symposium on Communications, Control and Signal Processing ISCCSP*, Mar. 2008, pp. 689-696.
- [43] F. Syed et al., "Rule-Based Fuzzy Gain-Scheduling PI Controller to Improve Engine Speed and Power Behavior in a Power-Split Hybrid Electric Vehicle," *Fuzzy Information Processing Society (NAFIPS)*, June 2006, pp. 284-289.
- [44] F. Syed et al., "Fuzzy Gain-Scheduling Proportional-Integral Control for Improving



Engine Power and Speed Behavior in a Hybrid Electric Vehicle," IEEE Transactions on Vehicular Technology, Vol. 58, No. 1, Jan. 2009, pp. 69-84.

- [45] W. Xiukun and L. del Re, "Gain Scheduled Control for Air Path Systems of Diesel Engines using LPV Techniques," IEEE Transactions on Control Systems Technology, Vol. 15, No. 3, May 2007, pp. 406-415.

Biographies



Simon O. Omekanda was born in Rabat, Morocco, on September 15, 1984. He received his Bachelor in Science (B.S.) degree in electrical engineering from Pennsylvania State University, State College, in 2009 and the Masters in Science (M.S.) degree

in electrical and computer engineering from Oakland University, Rochester, MI, in 2011. He is currently getting his Ph.D in controls engineering from Oakland University. He has been working as a teaching and research assistant for the electrical and computer engineering department at Oakland University during this time. He has taught and helped students in the areas of controls and estimation theory as well as using matlab/simulink for simulation. His research areas primarily include design, implementation and simulation of nonlinear observers for state estimation and control, multivariable control, subsystem interconnection with application to internal combustion engines and electric machine in automotive applications. He has published one paper titled "Application of Extended Observer with Gain Scheduling Control to Internal Combustion Engine Model" in a similar area as the one presented here.



Todd A. Perkins is a Ph.D. student in the Electrical and Computer Engineering department. He earned his B.S. in Electrical Engineering at Howard University. After spending nearly 20 years in the

broadcast, automotive and telecommunications industry, he left to pursue a M.S. and Ph.D. at Oakland University so he could teach engineering. Under the 'coaching' of Dr. M.A. Zohdy, his working dissertation title is *Adaptive Nonlinear Control of Clutch Engagement in Modern Automotive Transmissions*. His current research includes piecewise linear (PWL) modeling, State Space modeling, nonlinear Adaptive Controls and Simulink modeling. Todd enjoys working as a Teaching Assistant and teaching *Science, Technology, Engineering and Math* (STEM) outreach camps to K-12 students.



Mohamed A. Zohdy was born in Caro, Egypt. He received B.Sc. degree in Electrical Engineering, Cairo University, Egypt in 1968. He received his M.S. and Ph.D. degrees in Electrical Engineering, University of Waterloo, Canada in 1974, and 1977 respectively. He is

currently a Professor at Oakland University, Rochester Hills, Michigan, U.S.A. His research interests are in areas of Controls and Soft Computing.





Performance of FACTS Devices on Voltage Stability in a Deregulated Power System

N.Sambasiva Rao¹, Dr.J.Amarnath², Dr.V.Purnachandra Rao³

¹Associate Professor & Head, Department of EEE, NRI Institute of Technology, Vijayawada, A.P, India.

²Professor, Department of EEE, Jawaharlal Nehru Technological University, Hyderabad, A.P, India

³Professor, Department of EEE, Andhra University, Visakhapatnam, A.P, India

nsraohodeee@gmail.com, amarnathjinka@yahoo.com, venigandlaprao@rediffmail.com

Abstract

In a deregulated power system structure, power producers and customers share a common transmission network for wheeling power from the point of generation to the point of consumption. All parties in this open access environment may try to produce the energy from the cheaper source for greater profit margin, which may lead to overloading and congestion of certain corridors of the transmission network. This may result in violation of line flow, voltage and stability limits. In power system environment voltage stability plays major role, it is integral part of the power system stability. In general Voltage stability problems occur more frequently in a heavily loaded system. Lack of voltage stability may develop severe problems in the power system, which might lead to system black out in the form of sudden voltage dips at the load buses. The cause of voltage instability could be numerous. The control of voltage levels can be accomplished using FACTS Controllers like Static Var Compensator (SVC), Thyristor-controlled phase angle regulator (TCPAR). This paper focuses on the enhancement Voltage Stability using FACTS devices. The optimal location of FACTS devices were determined based on Sensitivity methods. The effectiveness of proposed method is demonstrated on modified IEEE-9 bus system using power world simulator 8.0.

Keywords: Deregulation, Voltage Stability , TCPAR, SVC, Power world Simulator.

1. Introduction

In deregulation it is expected that the product will be exchanged at several points along the generation, transmission and distribution systems. Hence it is the responsibility of the power suppliers to supply safe and economical electric power to customers with the existing transmission line efficiently.

“Voltage stability is the ability of a power system to maintain steady acceptable voltages at all buses in the system under normal operating conditions and after being

subjected to a disturbance”. In power system environment voltage stability plays major role, it is integral part of the power system stability. In general Voltage stability problems occur more frequently in a heavily loaded system.

2. Causes of Voltage Instability

The main reason for voltage instability is the lack of sufficient reactive power in a system. Generator reactive power limits and reactive power requirements in transmission lines are the main causes of insufficient reactive power.

2.1 Reactive Power Limits of Generators

Synchronous generators are the main devices for voltage control and reactive power control in power systems. In voltage stability analysis active and reactive power capabilities of generators play an important role. The active power limits are due to the design of the turbine and the boiler. Therefore, active power limits are constant. Reactive power limits of generators are more complicated than active power limits. There are three different causes of reactive power limits that are; stator current, over-excitation current and under-excitation limits. The generator field current is limited by over-excitation limiter in order to avoid damage in field winding. In fact, reactive power limits are voltage dependent. However, in load flow programs they are taken to be constant in order to simplify analysis.

2.2 Reactive Power Requirements in Transmission Lines

Transfer of active and reactive power is provided by transmission lines. Since transmission lines are generally long, transfer of reactive power over these lines is very difficult due to significant amount of reactive power requirement.

The characteristics of voltage stability and the effect of transmission lines are illustrated by 2-bus simple test system that is shown in Figure 1.



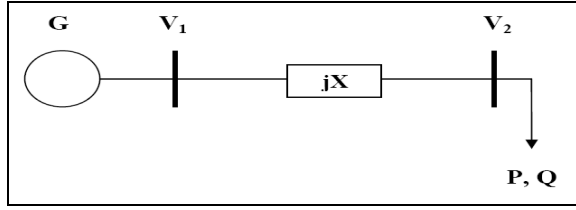


Figure 1. Bus simple test system

Active and reactive power delivered to load bus can be written as

$$P = \frac{V_1 V_2}{X} \sin \delta \quad (1)$$

$$Q = \frac{V_1 V_2}{X} \cos \delta - \frac{V_2^2}{X} \quad (2)$$

Eliminating δ and solving Equation 1 and 2 for V_2 yields Equation

$$V_2 = \sqrt{\frac{V_1^2}{2} - QX \pm X \sqrt{\frac{V_1^2}{4X^2} - P^2 - Q} \frac{V_1^2}{X}} \quad (3)$$

In order to attain a real solution for V_2 Equation 3 should be satisfied.

$$\frac{V_1^2}{4X^2} - P^2 - Q \frac{V_1^2}{X} \geq 0 \quad (4)$$

substitute the short circuit power at the receiving end,

$$S_{sc} = \frac{V_1^2}{X} \left(\frac{S_{sc}}{2} \right)^2 \geq P^2 + Q S_{sc} \quad (5)$$

The maximum possible transfer of active power is $\frac{S_{sc}}{2}$

(for $Q=0$) and the maximum possible transfer of

reactive power is $\frac{S_{sc}}{4}$ (for $P=0$). Since

$\left(\frac{S_{sc}}{2} \right) > \left(\frac{S_{sc}}{4} \right)$, it can be accomplished that transfer

of reactive power is more complicated than transfer of active power and as it is observed from Equations 1 and 2 transfer of power is inversely proportional to line reactance.

Overhead lines either absorb or supply reactive power, depending on the load current. They generate reactive power under light load since their production due to the line shunt capacitance exceeds the reactive power requirement in the transmission line due to the line impedance. Under heavy load, they absorb more reactive power than they produce.

Underground cables produce reactive power since the power requirements never exceed the production due to

their high shunt capacitance under all operating conditions. Since they produce reactive power, a definite amount of reactive power demand of loads is met by the power produced by underground cables. Thus, the possibility of seeing voltage stability problem in buses decreases.

3. Voltage Collapse

Voltage collapse is the process by which the sequence of events accompanying voltage instability leads to a low unacceptable voltage profile in a significant part of system.

When a power system is subjected to a sudden increase of reactive power demand, the required demand is met by the reactive power reserves supplied from generators and compensation devices. Most of the time, this can be achieved since there are sufficient reserves. Sometimes, it is not possible to meet this rapid increase in demand due to combination of events and system conditions. Thus, voltage collapse and a major breakdown of part or all of the system may occur.

Typical scenario of a voltage collapse can be summarized as follows:

- Some of the large generating units near load centers can be out of service due to abnormal operating conditions. This reduces reactive power supplied and some transmission lines are heavily loaded so as to carry sufficient reactive power to problematic parts of the grid.
- Loss of a heavily loaded transmission line due to a fault causes additional loading on the remaining adjacent lines. This increases the reactive power requirement in lines since reactive power requirement increases rapidly for loads above surge impedance loading. Thus, reactive power demand in the system augments.
- The load voltages decrease because of extra reactive power demand. This causes a decrease in load demand. The voltage control system of generators restores terminal voltage by increasing field excitation. The additional reactive power flow through transformers and transmission lines causes increased voltage drop across each of these elements.
- As a result of tap changing operations, the reactive power output of generators increase. When the generator hits the reactive power capability limit, the terminal voltage decreases. Its sharing of reactive power is transferred to other generators, leading to overloading of more generators. The process eventually leads to voltage instability and voltage collapse.

Therefore, it is very important to analyze the underlying principle of voltage stability in every power system.

In assessing voltage security of power systems, we deal with P-V and Q-V curves. The methods of P-V and Q-V curves are widely accepted tools; they can provide real and reactive power margins, respectively. Variations in P and Q affect the voltages at the load buses. P-V and Q-V curves are generated by series of power-flow solutions.



3.1 Importance of PV Curve

The process of voltage stability analysis involves the transfer of P from one region of a system to another, and monitoring the effects to the system voltages V. This type of analysis is commonly referred to as a P-V study.

The P-V curves, real power- voltage curve, are used to determine the MW distance from the operating point to the critical voltage. A typical P-V curve is shown in Figure 2.

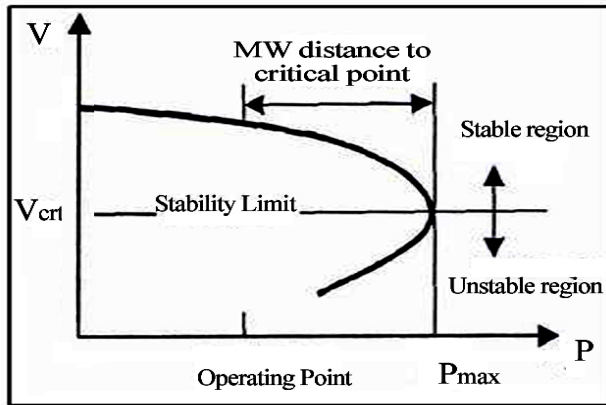


Figure 2.Importance of P-V Curve

Consider a single, constant power load connected through a transmission line to an infinite-bus. Let us consider the solution to the power-flow equations, where P, the real power of the load, is taken as a parameter that is slowly varied, and V is the voltage of the load bus. The three regions shown in Figure 2 are related to the parameter P. In the first region, the power flow has two distinct solutions for each choice of P; one is the desired stable voltage and the other is the unstable voltage. As P is increased, the system enters the second region, where the two solutions intersect to form one solution for P, which is the maximum. If P is further increased, the power-flow equations fail to have a solution. This process can be viewed as a bifurcation of the power-flow problem. The method of maximum power transfer determines critical limits on the load bus voltages, above which the system maintains steady-state operation.

The P-V curve is drawn for the load bus and the maximum transmissible power is calculated. Each value of the transmissible power corresponds to a value of the voltage at the bus until $V = V_{crit}$ after which further increase in power results in deterioration of bus voltage.

The top portion of the curve is acceptable operation whereas the bottom half is considered to be the worsening operation. The risk of voltage collapse is much lower if the bus voltage is further away, by an upper value, from the critical voltage corresponding to P_{max} . Hence, the P-V curve can be used to determine the system's critical operating voltage and collapse margin.

3.2 Importance of QV-Curve

The Q-V curves, reactive power- voltage curve, are used to determine the Mvar distance from the operating point to the critical voltage. A typical Q-V curve is shown in Figure 5.3. It shows the sensitivity and variation of bus voltages with respect to reactive power injections or

absorptions. As a traditional solution in system planning and operation, the voltage level is used as an index of system voltage instability. If it exceeds the limit, reactive support is installed to improve voltage profiles. With such an action, voltage level can be maintained within acceptable limits under a wide range of MW loadings. In reality, voltage level may never decline below that limit as the system approaches its steady state stability limits. Consequently, voltage levels should not be used as a voltage collapse warning index.

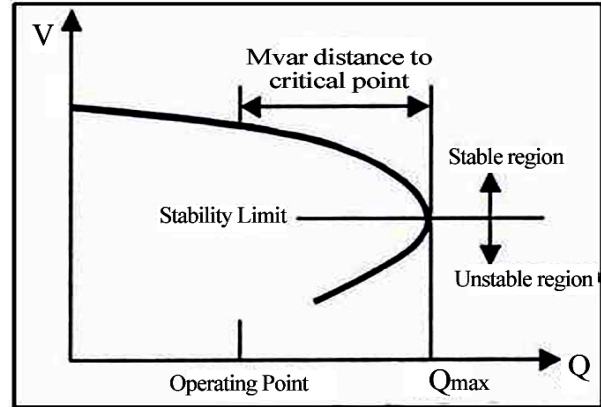


Figure 3.Importance of Q-V Curve

In Figure 3, the Q axis shows the reactive power that needs to be added or removed from the bus to maintain a given voltage at a given load. The reactive power margin is the Mvar distance from the operating point to the bottom of the curve. The curve can be used as an index for voltage instability. Near the nose of a Q-V curve, sensitivities get very large and then reverse sign. Also, it can be seen that the curve shows two possible values of voltage for the same value of power.

The power system operated at lower voltage value would require very high current to produce the power.

That is why the bottom portion of the curve is classified as an unstable region; the system cannot be operated, in steady state, in this region. The top portion of the curve represents the stability region while the bottom portion from the stability limit indicates the unstable operating region. It is preferred to keep the operating point far from the stability limit.

The control of voltage levels is accomplished by controlling the production, absorption, and flow of reactive power at all levels in the system. The devices used for this purpose may be classified as follows

- Sources or sinks of reactive power, such as shunt capacitors, shunt reactors, synchronous condensers, and static var compensators (SVCs)
- Line reactance compensators, such as series capacitors.
- Regulating transformers, such as tap-changing transformers and boosters.

A static var system is ideally suited for applications requiring direct and rapid control of voltage.

4. FACTS Controllers

4.1 Static VAR Compensator (SVC)

According to IEEE-CIGRE co-definition, a static var compensator is a static var generator whose output is



varied so as to maintain or control specific parameters (e.g. voltage or reactive power of bus) of the electric power system.

SVC is a first generation FACTS controller that is already in operation at various places in the world. Static VAR Compensator (SVC) is a shunt connected FACTS controller whose main functionality is to regulate the voltage at a given bus by controlling its equivalent reactance as shown in Fig. 4.

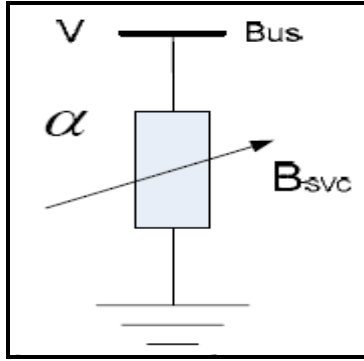


Figure 4. SVC Model

The reactive power injected into the bus due to SVC can be expressed as

$$Q_{SVC} = B_{SVC} V_i^2 \quad (6)$$

Where V_i is the voltage magnitude of the bus at which the SVC is connected.

This thesis provides information on the SVC total susceptance model required to achieve a given level of compensation.

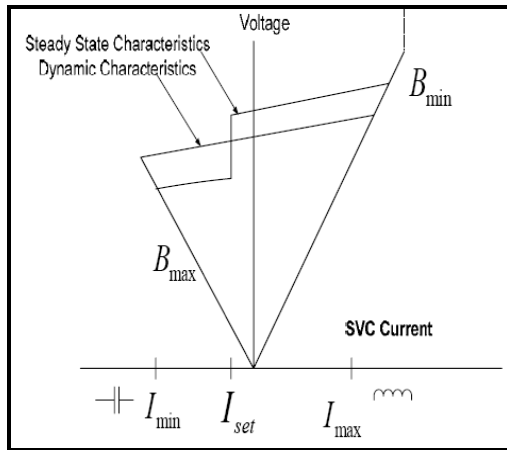


Figure 5. Voltage-Current Characteristics of SVC

Figure 5 shows the steady-state and dynamic voltage-current characteristics of the SVC. In the active control range, current/susceptance and reactive power is varied to regulate voltage according to a slope (droop) characteristic. The slope value depends on the desired voltage regulation, the desired sharing of reactive power production between various sources, and other needs of the system. The slope is typically 1-5%. At the capacitive

limit, the SVC becomes a shunt capacitor. At the inductive limit, the SVC becomes a shunt reactor.

4.2 Thyristor Controlled Phase Angle Regulator

TCPAR is identical with a phase shifting transformer with a thyristor type tap changer and plays an important role in increasing loadability of the existing system and controlling the congestion in the network. FACTS device like TCPAR can be used to regulate the power flow in the tie-lines of interconnected power system.

This is also known as Static Phase Shifter (SPS) and phase shift with respect to the bus voltage is achieved by adding or subtracting a variable voltage component in quadrature with the bus voltage. The quadrature voltage is injected in series with the transmission line by a boosting transformer. The basic arrangement is shown in figure 4.

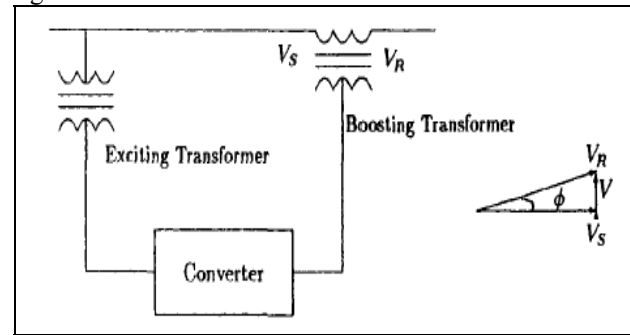


Figure 4 Shows Static Phase Shifter

5. Optimal Location Based on Sensitivity Approach for TCSC & SVC

5.1 Optimal Location of Static Var Compensator

For computing the loss sensitivity index with respect to SVC an exact loss formula has been used, which expresses Q_L as,

$$C_i = \frac{dQ_L}{dQ_i} = 2 \sum_{j=1}^n (\alpha_{ij} Q_i + \beta_{ij} P_j) \quad i=1, \dots, n \quad (8)$$

where α_{ij} and β_{ij} are the loss coefficients defined as,

$$\alpha_{ij} = \frac{r_{ij}}{V_i V_j} \cos(\delta_i - \delta_j) \quad (9)$$

$$\beta_{ij} = \frac{x_{ij}}{V_i V_j} \sin(\delta_i - \delta_j) \quad (10)$$

$P_i + jQ_i$ is the complex injected power at bus i and X_{ij} is the imaginary part of the ij^{th} element of $[Z_{bus}]$.

The SVC should be placed at a bus i having most negative sensitivity index (C_i). The placement of SVC has been considered at load buses only.



5.2 Optimal Location of TCPAR

Here, a method based on the sensitivity of the total system reactive power loss (Q_L) with respect to the control variables of the FACTS devices

1. Loss sensitivity with respect to control parameter θ_{ij} of TCPAR placed between buses i and j ,

$$b_{ij} = \frac{dQ_L}{d\theta_{ij}}$$

2. Phase shift (α_{ij}) for a TCPAR placed between buses i and j . In that line θ_{ij} is the net phase shift in the line and includes the effect of the TCPAR. The loss sensitivities with respect to X_{ij} and θ_{ij} can be computed as:

$$b_{ij} = \frac{dQ_L}{d\theta_{ij}} = [-2aV_iV_jB_{ij}\sin\theta_{ij}] \quad (11)$$

5.3 Selection of Optimal Placement of FACTS Devices

Using the loss sensitivities as computed in the previous section, the criteria for deciding device location might be stated as follows:

1. SVC should be placed at a bus i having most negative sensitivity index (C_i)
2. TCPAR must be placed in the line having the highest absolute value of loss sensitivity index (b_{ij})

6. Contingency

The operation of a power grid requires unplanned component outages could lead to dramatic and costly blackouts. Planning and operating criteria are designed in such a way that “the interconnected power system shall be operated at all times as a result of any single contingency or multiple contingencies.

6.1 Critical Contingency Screening

A suitable location of FACTS devices will be that which would give best performance in most of the operating conditions. To find out the severe line outage contingencies, a real power flow performance index (PI) has been used as defined in the following:

$$PI = \sum_{m=1}^N \frac{w_m}{2n} \left(\frac{P_{LM}}{P_{LM}^{MAX}} \right)^{2n} \quad (12)$$

Where P_{LM} is the real power flow

P_{LM}^{MAX} is the rated capacity of line- m ,
 n is the exponent and

W_m a real nonnegative weighting coefficient

which may be used to reflect the importance of lines.

PI will be small when all the lines are within their limits and reach a high value when there are overloads. Thus, it provides a good measure of severity of the line overloads for given state of the power system. By most of the operational standards, the system with one huge violation is much more severe than that with many small violations.

In this study, the value of exponent has been taken as 2 and $w_i=1$.

7. Results & Discussions

The Proposed methods for optimal placement of TCPAR and SVC for voltage stability improvement are tested on IEEE 9 bus system. The Computation of power flow is carried out by using Power world simulator to calculate the bus voltages. The Critical contingency screening is performed using Performance index using MATLAB programming.

7.1 System Model

This system consists of 9 buses, 9 line sections, 3 generator buses and 3 load buses.

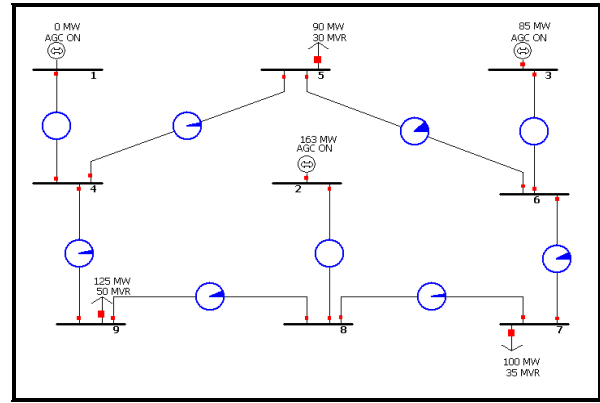


Figure .8 Single line diagram of IEEE 9 bus System

7.2 Sensitivity Index

Table 1. Var loss sensitivity index of IEEE – 9 bus system

Line No. (K)	From- To Bus	Loss Sensitivity	
		TCPAR (b_{ij})	SVC (C_{ij})
1	1-4	1.441	-3.4022
2	8-2	-3.26	-3.438
3	3-6	1.696	-3.263
4	4-5	0.588	4.1572
5	9-4	-0.752	0.4279
6	5-6	-1.19	0.9455
7	6-7	0.4486	-2.4924
8	7-8	-1.513	-1.6932
9	8-9	1.679	-3.9318

For this system, from Table1,

1. Optimal location of TCPAR for an IEEE 9 bus system based on loss sensitivity analysis the line having the highest absolute value of loss sensitivity index b_{ij} index is chosen for placement of the TCPAR device. Hence bus 3 is selected.
2. Optimal location of SVC for an IEEE 9 bus system based on loss sensitivity analysis is the lines having the highest negative sensitivity index is chosen for



placement of the SVC device. Hence bus 9, a load bus is selected.

The optimal locations considered are line3 (3-6) for TCPAR with a phase shift of 2.9 degrees and unity tap ratio and bus 9 for SVC with a nominal value of 50 Mvar.

Modified IEEE 9bus system incorporating TCAPAR,SVC shown in Figure.9

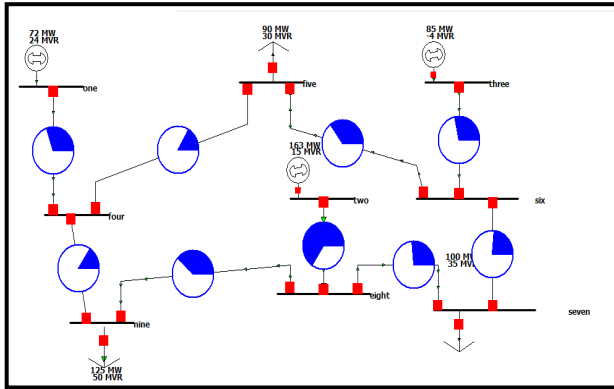


Figure.9 Single line diagram of IEEE 9 bus System with FACTS devices

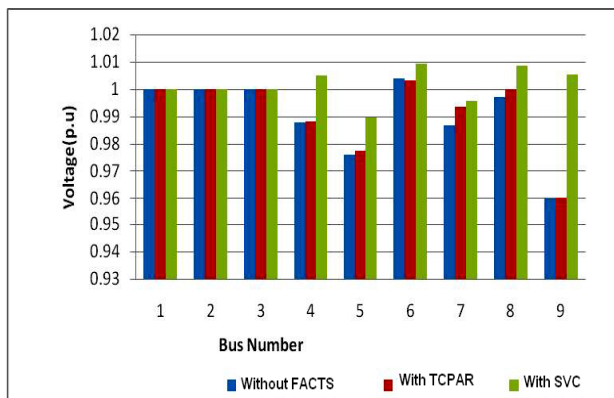


Figure. 10 Comparison of voltages for 9 bus system at base case

Figure 10 shows the comparison of voltages for an IEEE 9 bus system without and with FACTS devices under normal conditions. It is observed that by placing SVC at bus 9 the voltage is more improved than by placing TCPAR line3 (3-6)

The critical contingency (line outage) ranking using the PI values, are computed for each single line outage case. The ten critical lines at the base case loading, in the order of relative severity are given in the Table.2 By observing the Table .2, line 9(8-9) is the most critical line for outage as contingency which is having the highest PI index.

The voltage profile at each bus by placing TCSC and SVC for single outage of line at line 9(8-9) is shown in Fig.10. It is observed that by placing SVC at bus 9 the voltage is more improved than by placing TCPAR line3 (3-6) even at single outage of line.

Table 2. Single Outage Contingency Ranking for IEEE 9 Bus System

S.No	Line No	End Buses	PI Index
1	Intact Case	-	0.504
2	1	1-4	0.86
3	2	8-2	0.87
4	3	3-6	0.97
5	4	4-5	0.81
6	5	9-4	0.83
7	6	5-6	1.41
8	7	6-7	0.69
9	8	7-8	0.844

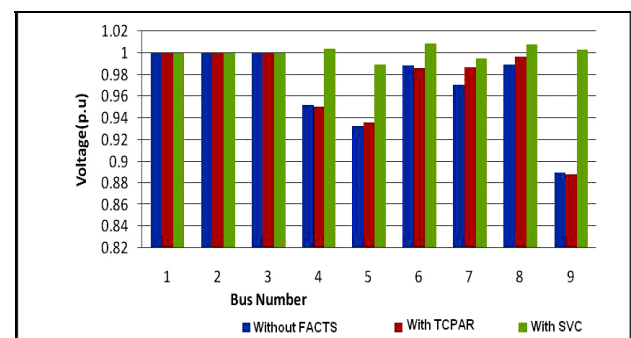


Figure.10 Comparison of voltages for 9 bus system at single outage (8-9)

Table 3. Double Line Outage Contingency Ranking for IEEE 9 Bus System

S.No	Line No	End Buses	PI Index
1	Intact Case	-	0.504
2	9,6	8-9,5-6	1.24
3	9,3	8-9,3-6	0.974
4	9,2	8-9,8-2	0.884
5	6,3	5-6,3-6	0.67
6	6,2	5-6,8-2	0.942
7	3,2	3-6,8-2	1.72

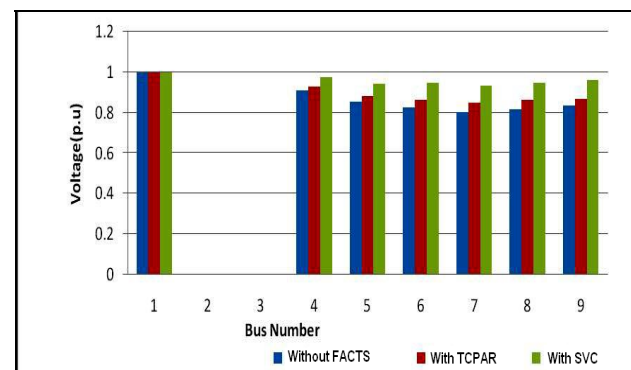


Figure.11 Comparison of voltages for 9 bus system at double outage (3-6, 8-2)



From Table 3, the top five locations are selected and PI values are calculated for the different combinations of top five locations to find the severity of the system with double outages. Table 3 shows the double line outage contingency ranking for an IEEE 9 bus system. By observing the Table 3, line 3(3-6) and line 2(8-2) are the most critical lines for double outages as contingency having the highest PI index.

The voltage profile at each bus by placing TCPAR and SVC for double outage of lines at line 3(3-6) and line 2(8-2) is shown in Fig.11. It is observed that by placing SVC at bus 9 the voltage is more improved than by placing TCPAR in line (3-6) even at double outage of line.

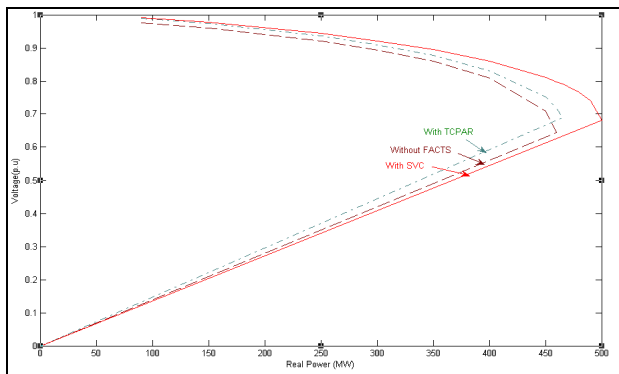


Figure.12 PV Curve at bus 5 for 9 bus system

Fig12. shows the PV curve at bus 5 for an IEEE 9 bus system without and with FACTS Devices. From the Fig.5.9, it is observed that the voltage stability margin has been more improved by placing SVC at bus 9 than by placing TCPAR line3 (3-6).

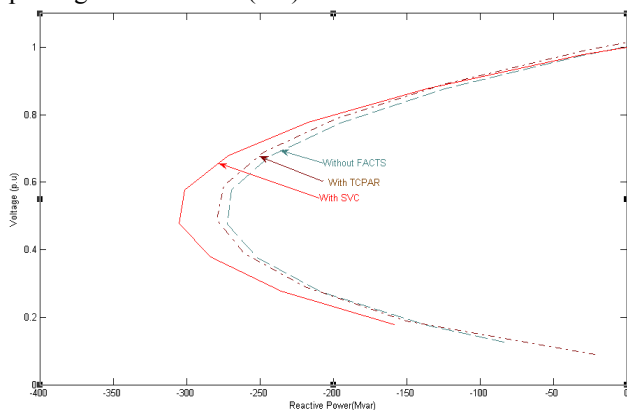


Figure.13 QV Curve at bus 5 for 9 bus system

Figure 13. shows the QV curve at bus 5 for an IEEE 9 bus system without and with FACTS Devices. From the figure 13, it is observed that the voltage stability margin has been more improved by placing SVC at bus 9 than by placing TCPAR line3 (3-6).

8 Conclusion

In power system environment voltage stability plays major role, it is integral part of the power system stability. In general Voltage stability problems occur more frequently in a heavily loaded system.

Lack of voltage stability may develop severe problems in the power system, which might lead to system black out in the form of sudden voltage dips at the load buses. The cause of voltage instability could be numerous. The control of voltage levels can be accomplished using FACTS Controllers like Static Var Compensator.

It is observed that the SVC consistently gives the better performance than the TCPAR in all case studies conducted, also giving better voltage stability margin.

9 Acknowledgement

I author, very grateful to my GOD **Dr. J. AMARNATH** Professor Department of EEE,JNTU college of Engineering, Hyderabad Without his assistantship the work could not be completed

10 References

- [1] Thierry Van Cutsem, Costas Vournas, "Voltage Stability of Electric Power Systems".
- [2] Hingorani, N.G, Gyugyi, L, "Understanding FACTS: Concepts and Technology of Flexible AC Transmission Systems", Institute of Electrical and Electronic Engineers Press, New York, 2000.
- [3] H O Bansal, H P Agrawal, S Tiwana, A R Singal And L Shrivastava, "Optimal Location of FACT Devices to Control Reactive Power", International Journal of Engineering Science and Technology Vol. 2(6), 2010, 1556-1560
- [4] G. MadhusudhanaRao, P. Vijaya Ramarao, T. Jayanth kumar, "Optimal Location of TCSC and SVC for Enhancement of ATC in a De-Regulated Environment using RGA", IEEE Transactions on Power Systems,2010.
- [5] Mohammed Osman Hassan, S. J. Cheng, Zakaria Anwar Zakaria, "Steady-State Modeling of SVC and TCSC for Power Flow Analysis", Proceedings of the International MultiConference of Engineers and Computer Scientists 2009 Vol II, IMECS 2009, March 18-- 20, 2009, Hong Kong.
- [6] Maciej Pikulski, "Controlled Sources Of Reactive Power Used For Improving Voltage Stability", Electrical Power Systems and High Voltage Engineering, Aalborg University , Aalborg, June 2008.
- [7] Bansilal, D Thukaram and K Parthasarathy, "An expert system for power system voltage stability improvement", *Electrical Power & Energy Systems*, Vol. 19, No. 6, pp. 385-392, 1997.
- [8] G. Singh, S. N. Singh, and S. C. Srivastava, "An Approach for Optimal Placement of Static VAR Compensators Based on Reactive Power Spot Price", IEEE Transactions On Power Systems, Vol. 22, No. 4, November 2007.
- [9] Abdelaziz Laïfa and Mohamed Boudour, "Optimal Location of SVC for Voltage Security Enhancement using MOPSO", Journal of electrical systems, pp:73-78, November 2009.
- [10] Preecha Preedavichit , S.C. Srivastava, "Optimal reactive power dispatch considering FACTS devices", *Electric Power Systems Research* 46 (1998) 251–257.



Biographies



N. Sambasiva Rao received the B.Tech degree in Electrical & Electronics Engineering and M. Tech in Electrical Power Engineering from JNTU Hyderabad, India. He has 12 years experience in teaching. He is perusing his Ph.D from JNTU,

Hyderabad, India. He published a 7 research papers in various International Journals and 2 research papers in National Conferences. He is the Member of International Association of Engineers (IAENG) and Life member of ISTE. He is currently working as Associate Professor and Head of the department in Electrical & Electronics Engineering at NRI Institute of Technology, Agiripalli, India. He got ***“Best Achiever award of Andhra Pradesh “By NCERT, New Delhi, India.*** His Areas of interest include Electrical Machines, FACTS and power System Deregulation.



J. Amarnath obtained the B.E degree in electrical engineering from Osmania University, Hyderabad, A.P. India in 1982 and the M.E. degree in power systems from Andhra University, Visakhapatnam in 1984. He worked in Tata Electric

Company, Bombay during 1985-1986. In 1987 he was a Lecturer in Andhra University for a period of 2 years and then he joined in Nagarjuna University for a period of 4 years as Lecturer. In 1992 he joined JNTU College of Engineering, Kukatpally, Hyderabad. Presently he is professor and head of the department of Electrical and Electronics engineering department, JNTU, Hyderabad, A.P. He presented more than 250 research papers in national and international conferences. His research interests includes high voltage engineering, gas insulated substations, industrial drives, power electronics, power systems, microprocessors and microcontroller applications to power systems and industrial drives.



V. Purnachandra Rao obtained the B.E degree in electrical engineering from Govt college of Engineering, Kakinada, A.P. India in 1962, M.E. degree in power systems from BHU, Varanasi in 1964 and Ph.D from BHU in 1972. He worked as

Lecturer Associate Professor in BHU varanasi during 1964-1979. He worked as Associate Professor, Professor, Head of the Department in Andhra University from 1979-2000. He presented more than 50 research papers in national and international conferences. His research interests includes high voltage engineering, gas insulated substations, industrial drives, power electronics, power systems, microprocessors and microcontroller applications to power systems and industrial drives.





Suppression & Comparison of Magnetizing Current of a Transformer with PWM Voltage Source Converter

Sridevi Tirunagari, Ramesh Reddy Kolli

G.Narayanamma Institute of Technology & Science, Hyderabad, India.

sridi_t@yahoo.com, kollirameshreddy@yahoo.com

<http://www.gnits.ac.in>

Abstract

This paper presents inrush current phenomenon in a single phase and 3-Phase transformer. This is initially done in the absence of any inrush current suppressing device and then with Pulse Width Modulated (PWM) voltage source converter. Finally it is compared with other technique having DC voltage regulation using PI controller. In both the proposed techniques main transformer is connected in series to a PWM voltage source converter through a matching transformer to the source. As the PWM converter is connected in series to the source it acts as a resistor for the source current there by producing no inrush phenomenon. Inrush current suppression principles for both methods were discussed with the help of block diagrams. Variation of magnetizing current with varying control gains is discussed in both cases and the results were shown to confirm the validity. Both methods were developed & simulated in MATLAB/SIMULINK environment.¹

Keywords : *Inrush current, PWM converter, PI Controller, DC regulation.*

Nomenclature

V_{ref}	Reference output signal for converter
K	Control gain
I_s	Source current
V_{trab}	Main transformer line to line voltage
V_0	Voltage across converter
V_{tr}	Voltage across transformer
I_{sa}	'a' phase source current
V_{oa}	Voltage across PWM converter for 'a' phase

1. Introduction

Switching of the transformers will be done in many times during a day especially when the transformers are used in industrial facilities. It is well known that each

energization of the transformer will generate a transient inrush current even if the transformer carry no load. These inrush currents cause mal-operation of the protective relays which needs to be avoided. If it is a single phase transformer, inrush phenomenon can be avoided easily by simply connecting the transformer to the source at closing angle of 90 or 270 degrees. But, in 3-phase circuits, the inrush phenomenon cannot be avoided by simply adjusting the closing angle since the phase angles of the source voltages differ from each other by 120 degrees. Inrush phenomenon can be avoided by connecting series resistors which needs to be shorted before loading the transformer on the secondary side. But this method may cause re-inrush phenomenon with increased losses [1]. A PWM Converter can be connected in parallel which acts as a inrush current sinker on the source side but requires a large rating for the PWM Converter [2].

In the present work, proposed method of Suppressing the magnetizing current with series connected voltage source PWM converter is verified and extension of the method with dc voltage regulation using PI controller was discussed. With series connected voltage-source PWM converter the required rating of the PWM converter is about 0.25% of the main transformer in single phase circuits and it is less than 0.1 % in 3-phase circuits illustrating that it is useful for practical applications [3].

The rest of the paper is organized as follows; section 2 explains the inrush current of transformers. Section 3 presents suppression of inrush current using PWM converter. Section 4 introduces inrush current suppression with DC voltage regulation. Finally section 5 is the conclusion.

¹ This study has been implemented and both the methods were developed & simulated in MATLAB/SIMULINK environment



2. INRUSH CURRENT OF TRANSFORMERS

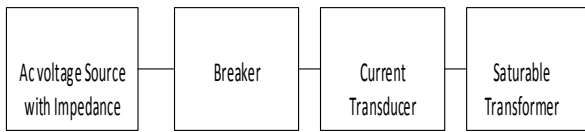


Figure 1 Constructed transformer model for 1-phase.

A 1-phase 200V, 60Hz, 6KVA base transformer is connected to an AC voltage source consisting of resistive impedance through a breaker & current transducer as shown in Figure 1. Breaker implements a Circuit breaker opening depending upon the external control of switching times.

In the present work a resistive snubber is considered. With the help of the current transducer, inrush current is measured and the results were shown for both closing angles of 0 degrees & 90 degrees. It was observed that high inrush current (53A) occurred when the transformer is connected with a closing angle of zero degrees & the inrush current is having less magnitude (0.5A) when the transformer is connected with a closing angle of 90 degrees. Figure 2 and Figure 3 represents Inrush Current of single phase transformer with closing angle of zero and 90 degrees respectively.

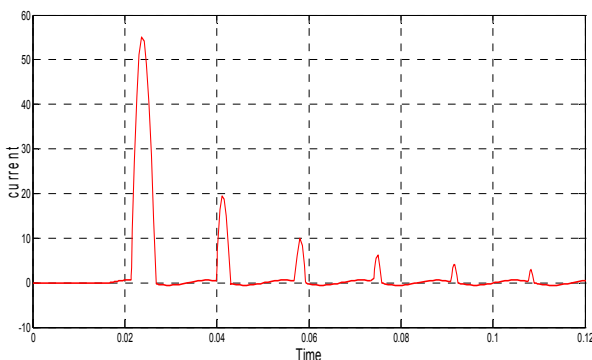


Figure 2. Inrush Current of transformer with closing angle of 0°

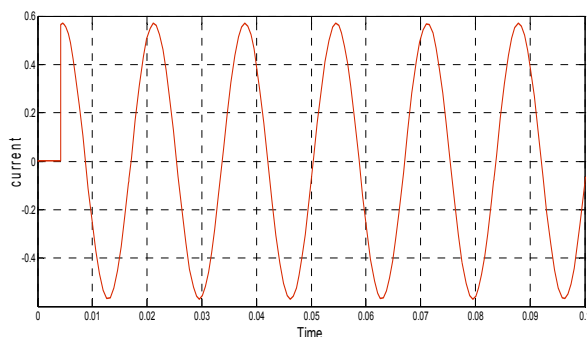


Figure 3. Inrush Current of transformer with closing angle of 90°

The same basic model is extended for 3-Phase circuits and the source current waveforms on the primary side of the 3-phase transformer are shown. As the voltages of

all the 3-phases differ with an angle of 120 degrees, with closing angle adjustment, we cannot avoid inrush current. It was observed that even with closing angle of 90 degrees, there is a flow of inrush current (120 Amps) in all the phases unlike single phase transformer circuits, where it was observed as 0.5Amp'

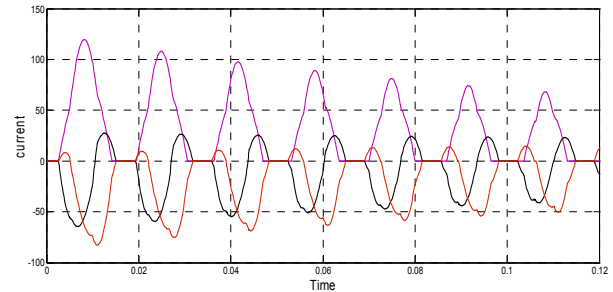


Figure 4. Three Phase Inrush Currents of transformer with closing angle of 90 degrees

3. SUPPRESSION OF INRUSH CURRENT USING PWM CONVERTER

1. A series voltage source PWM converter is connected through a matching transformer between source and main transformer where actual inrush phenomenon occurs.

2. In order to suppress the switching ripples caused by switching action, on ac side of the converter LC filter is connected.

3. The Control gain of PWM converter will be multiplied by the primary side source current of the transformer in order to obtain the reference output signal for the converter which means voltage source PWM converter is acting as a resistor of $K[\Omega]$ for the source current is $I_{s.}$

$$V_{ref} = K \cdot I_s \quad (1)$$

4. In the present work, for generation of gate pulses to PWM converter, sine triangular intercept technique is used. The primary side source current after passing through the low pass filter is treated with the triangular wave depending upon the required variation of control gain of PWM Converter.

Initially with the help of switch 1 main transformer is connected to the source at zero output voltage. Voltage source PWM converter will act as a resistor in order to suppress the inrush current. Finally after suppressing inrush current, switch 2 will be closed which results zero output voltage for PWM converter that is PWM converter is disconnected from the main circuit.

Even at closing of Zero or 180 degree where high magnitudes of inrush current results, we have to design in a manner such that the source current does not exceed the open circuit current. With open circuit current & voltage of the transformer we can get resistance value that is required for the PWM converter. The control gain K is determined as 765Ω considering modulation index



of 0.8. Data in Table-2 represents the values of the circuit constants used in calculations & simulations.

Turn Ratio	1:1
Open Circuit Current	0.2A
Open Circuit Power	25W
Short Circuit Power	116W
Source Voltage	200V
Source Frequency	60Hz
Control gain	765 Ω
DC Capacitance	500 μ F
Initial Vol. of DC capacitance	270V

TABLE I: DATA OF 1- ϕ 200V, 50 HZ, 6KVA TRANSFORMER

In 3-Phase circuits, three individual circuits will be connected as shown in Figure 6. The same concept of inrush current suppression is used by placing 3-phase PWM converter between the source voltage and the 3-phase transformer. Individual gains will be calculated and as the large control gain K of the voltage source PWM converter is effective for reducing the settling

time of magnetic flux of core, large control gain of 765 Ω is used in the present work to reduce the operating time. Longer operating times results larger amount of active power flow into the dc capacitor.

Single phase and three phase circuits were observed for different variations of control gain of PWM converter. With control gain suddenly made Zero i.e. removing the pulses to the converter suddenly at a particular instant is leading to re- inrush current phenomenon, with re-inrush current magnitude of 2.45 Amps for a while then to 0.35 amps at the primary or source side. Here in this case, the pulses are supplied till 0.15 sec and after 0.15 sec, converter was switched off suddenly. It was also observed that at 0.15 sec, even after removing the pulses a small voltage of 5V was observed across switch 2 which may be because of breaker resistance. Figure 7 Illustrate the simulated waveforms when the voltage source PWM converter is suddenly stopped in single phase circuits. In all the cases V_{tr} represents the voltage across the transformer, I_s represents the source current of the transformer and V_0 represents the voltage across PWM converter.

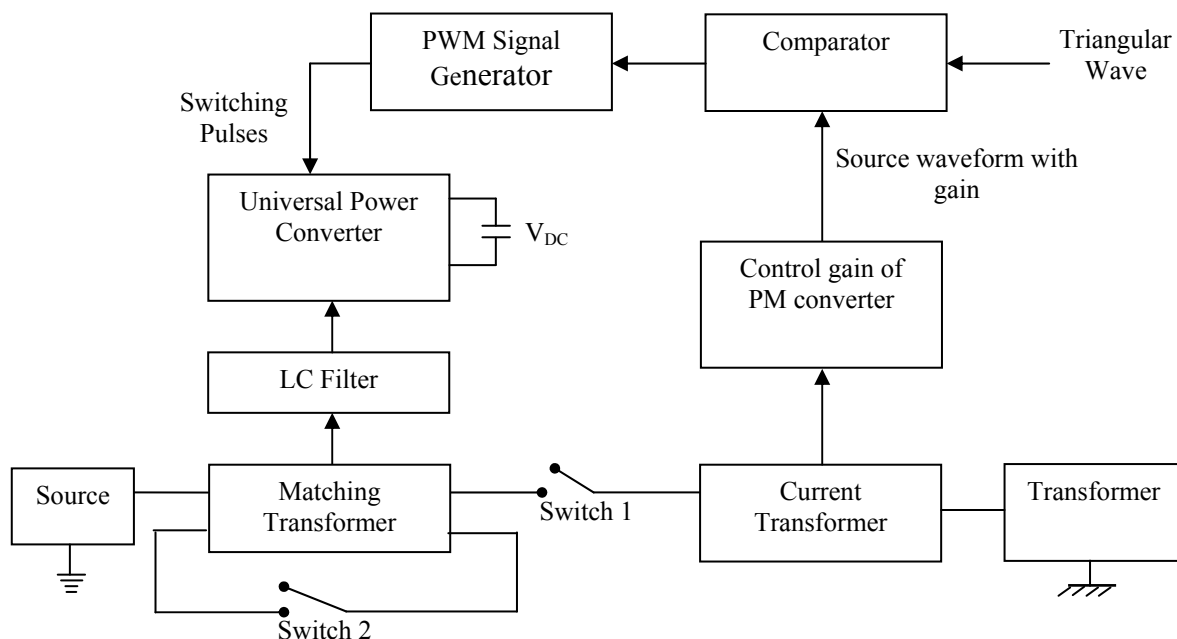


Figure 5. Inrush Current suppressor with PWM converter in 1- phase circuits.



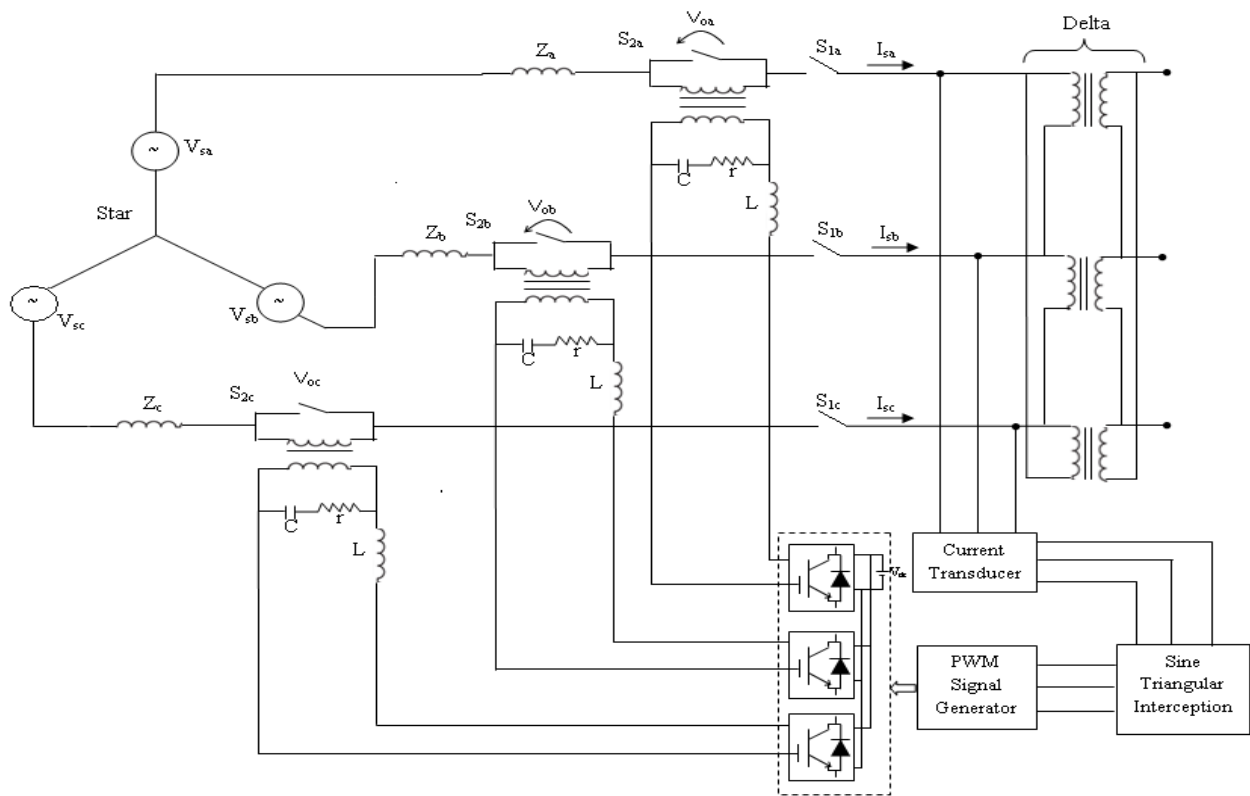


Figure 6. Inrush Current suppressor with PWM converter in 3- phase circuits

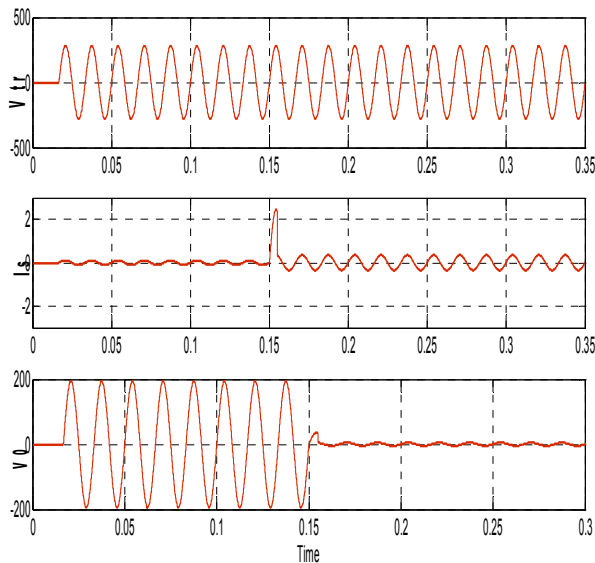


Figure 7. Re-inrush phenomenon when suddenly K made zero

Figure 8 represents the waveforms when the control gain of the PWM converter after 0.15 sec is gradually decreased over a period of 40ms from its initial constant value using ramp signal prevents re-inrush phenomenon and source current is observed with a magnitude of 0.35 Amps. It was also observed that with gradual decrement of control gain before stopping the voltage source PWM converter results zero output voltage across converter in addition to the suppression of re-inrush phenomenon.

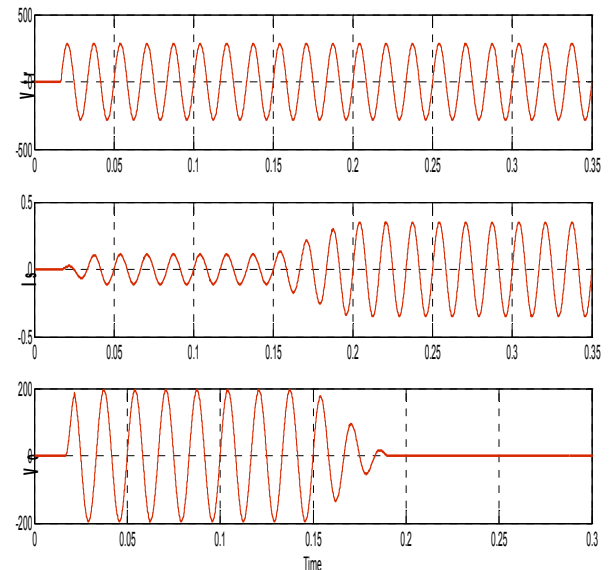


Figure 8. 1-φ output waveform's with gradual decrement of control gain

Inrush current suppressor is applied for 3-Phase circuits, and the simulation waveforms are shown in Figure 9. with gradual decrement of control gain of voltage source PWM Converter. 'a' phase voltages and currents are represented in Figure 9. V_{trab} is the line to line voltage between a & b phases at the main transformer terminals. I_{sa} is the 'a' phase primary side current and V_{oa} is the voltage across the PWM Converter. We observed that the series connected PWM converter suppressed the inrush



current perfectly in both single phase & 3-phase circuits. It was also observed that without series voltage source PMW converter active power is high and with PWM converter it was low.

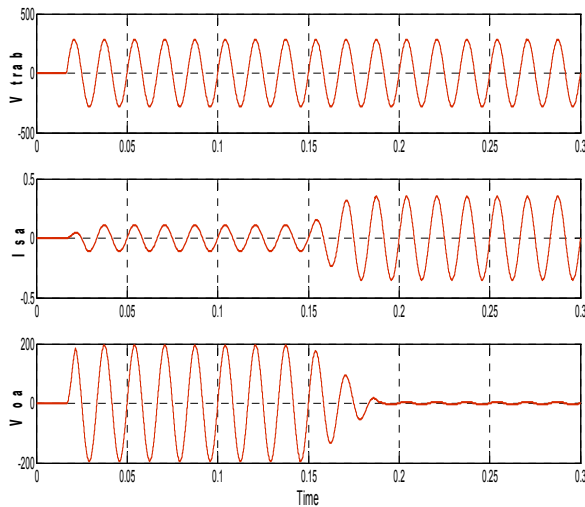


Figure 9. Waveform's with gradual decrement of control gain in 3-Phase Circuits.

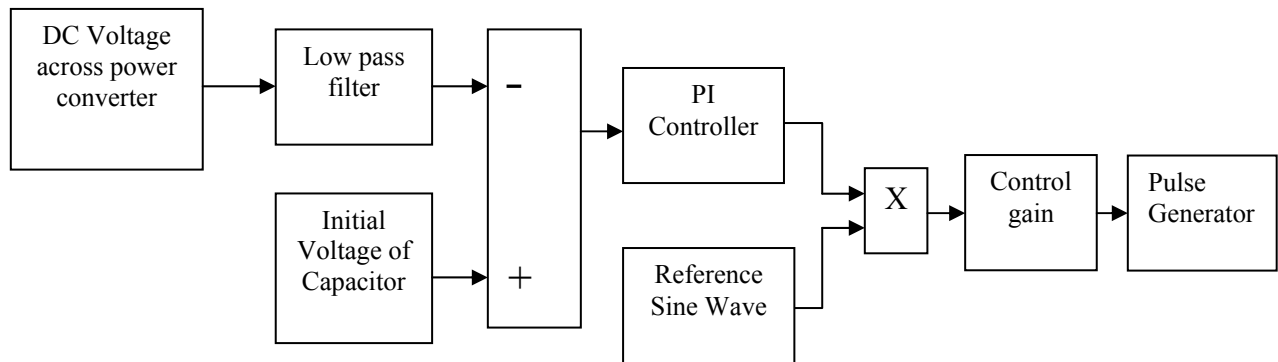


Figure 10 .Block Diagram for pulse generation using V_{dc}

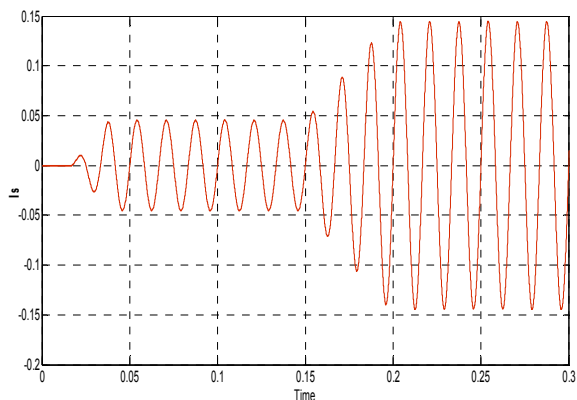


Figure 11. Inrush current with gradual decrement of K

When the pulses were suddenly stopped at 0.15 sec, a re-inrush phenomenon was observed with re-inrush current magnitude of 1.05Amp and magnetizing current magnitude of 0.15 Amps. Figure 12 represents the primary current when K is suddenly stopped.

4. INRUSH CURRENT SUPPRESSION WITH DC VOLTAGE REGULATION

For the same circuit another method is proposed to reduce the inrush current by using dc voltage regulation. Pulses are generated considering the voltage across the capacitor of the converter. By treating V_{dc} with low pass filter and using PI controller the pulses are generated. Control gain of the converter is considered as 765 and the initial voltage of DC capacitor as 270V. Figure 10 represents the block diagram approach for pulse generation using V_{dc} .

In order to match the digital & analog signals an integrator used with these pulses. It was observed that with gradual decrement of control gain, about 40 ms after 0.15 sec, the magnitude of inrush current was 0.15 Amps as shown Figure 11 where as with the first method it was 0.45 Amps.

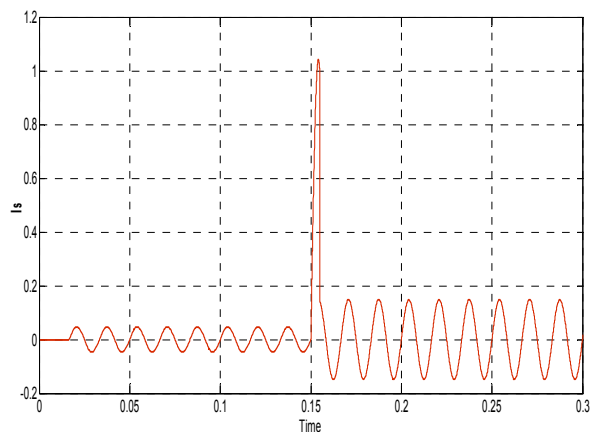


Figure 12. Inrush current when K suddenly stopped

By using the first method, re-inrush current magnitude is 2.45 Amps & inrush current magnitude 0.35 Amps, shows that proposed method is having best results than first method.



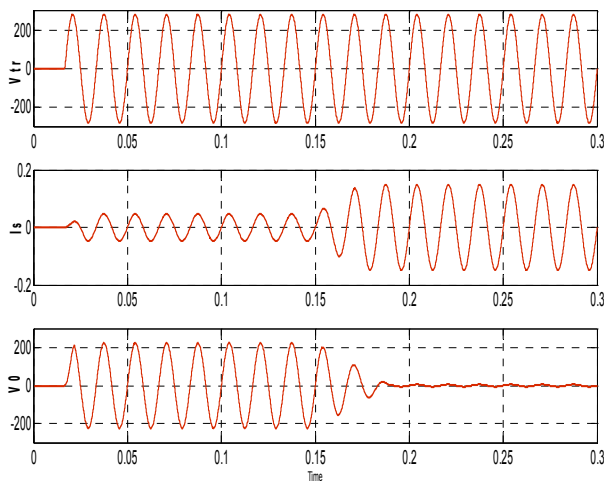


Figure 13. Output wave forms for 3-phase circuits with gradual decrement of K .

Figure 13 shows waveforms for 3-phase circuits with DC regulation and gradual decrement of control gain of voltage source PWM converter. Phase voltages and currents are shown in Figure 13. V_{tr} is the line to line voltage between a & b phases at the transformer terminals. I_s is inrush current per phase and V_0 is the voltage across the series connected PWM Converter. Without DC voltage regulation primary side source current was observed as 0.35 Amps and with dc voltage regulation it was observed as 0.15 Amps. Reactive and active power waves forms also observed for all the cases.

5. CONCLUSIONS

In this paper, the confirmation of the inrush phenomenon was done for a single and 3-phase transformer models using MATLAB/SIMLINK environment. It was observed that by changing the closing angle of circuit breaker we can control the magnetizing current in single phase transformers and it is not possible for the 3-phase transformers. Validation of inrush current suppression with series connected PWM converter was done with variations in control gain of converter in both single and 3-phase circuits. It was observed that with gradual decrement in control gain before stopping the pulses to series voltage source PWM converter results zero output voltage across the converter in addition to the suppression of re-inrush phenomenon.

A new technique was proposed to suppress the inrush current with DC voltage across the capacitor. With DC voltage regulation and variation in control gains there is a further decrement in the magnitude of inrush current which shows that it is more effective technique than series connected voltage source PWM converter technique. The proposed method applied to 3-phase circuits also and satisfactory results were obtained.

Active and reactive power for all the cases were observed. It can be concluded that the proposed method is superior than the method using series connected voltage source PWM converter.

6. REFERENCES

- [1] K.Shinohara, K.yamamoto, K. limori, Y.minari O sakata & M.Miyake "Compensation for magnetizing inrush currents in a transformer using PWM inverter" IEEJ Trans on industry applications, Vol. 121-D, PP. 730-738 , 2001.
- [2] K Mizuno, a Ogowa, K. Ike, S.Tanaka " Development of a transformer with the inrush current suppresser using the series connected resistors" The papers of technical meeting on static apparatus, IEE Japan SA-94-29, 1994.
- [3] Hiroaki yamoda, Eiji Hiraki, " A Novel method of suppressing the inrush current of transformers using a series connected vol-source PWM converter ", IEEE PEDS 2005.
- [4] Brunkle, J.H & Frohlich, K.J " Elimination of transformer inrush current by controlled switching, part – I Theoretical considerations " IEEE Trans. Power delivery vol:16 pp 276-280, 2001
- [5] Brunkle, J.H & Frohlich, K.J " Elimination of transformer inrush current by controlled switching, part – II Application and performance considerations " IEEE Trans. Power delivery vol:16 pp: 281-285, 2001
- [6] Wang J. Hamilton R. "Analysis of transformer inrush current and comparison of harmonic restraint methods in transformers protection", // 61st Annual Conference for Protective Relay Engineers. – April, 2008. – P. 142–169
- [7] Chen S. D., Lin R. L. " Magnetizing inrush model of transformers based on structure parameters", // IEEE Trans.Power Delivery. – July, 2005. – Vol. 20. – No. 3. – P. 1947–1954.
- [8] M. Jamali, M. Mirzaie, S. Asghar Gholamian "Calculation and Analysis of Transformer Inrush Current Based on Parameters of Transformer and Operating Conditions", ELECTRONICS AND ELECTRICAL ENGINEERING. ISSN 1392 – 1215 2011. No. 3(109).
- [9] Yabe, K., "Power differential method for discrimination between fault and magnetizing inrush current in transformers", IEEE Transactions on , Volume: 12 , Issue: 3 , July 1997 Pages:1109 – 1118.
- [10] R.Rahnavard, M.Valizadeh, S.H.Hosseini "Analitical analysis of transformer inrush current and Some new techniques for its reduction",
- [11] T.Sridevi, K. Ramesh Reddy, N. Leela Jaya Syamala "Harmonic Analysis of Inrush Current



using Fast Fourier Transform”, 2013 International Conference on Power, Energy and Control (ICPEC) ISBN 978-1-4673-6029-6

- [12] T.Sridevi, K. Ramesh Reddy “Unbalance and Harmonic Analysis in a 15-bus Network for Linear and Nonlinear Loads”, 2012 International Conference on Information Technology and Electrical Engineering (CITEE) ISSN: 2088-6578.

- [13] T Sridevi, K.Ramesh Reddy “Harmonic Mitigation & Comparison in a 15-bus network with Combined Hybrid Active Filter using SRF and pq-algorithms”, International Review of Automatic Control (I.R.E.A.CO.), Vol.7, N.2 March 2014, ISSN 1974-6059.

Biographies



Sridevi Tirunagari born in India in 1978. she received B.Tech in EEE from Nagarjuna University in 1999, M.Tech in Power systems from Jawaharlal Nehru Technological University, Anantapur, India in 2005 and presently pursuing Ph.D from

J.N.T.U Hyderabad. Currently she is working for G.Narayanamma institute of Technology & Science and she is a PhD student of J.N.T.U Hyderabad Under the supervision of Dr Kolli Ramesh Reddy. Six conference papers and One International Journal paper are at her credit.

She is a member of ISTE and IEEE. Her research and study interests include Power quality, Modeling of power system components and Harmonics in power systems.



Dr. Ramesh Reddy Kolli born in India in 1968. He received B.Tech in EEE from Nagarjuna University, Nagarjuna nagar, India in 1985. M.Tech in Electrical Engineering from N.I.T (Formerly Regional Engineering College) Warangal,

India in 1989 and Ph.D from S.V University Tirupathi, India in 2004. He is an author of 25 journal and conference papers and author of two text books. He is a member of IEEE, IE(I), WASET & NAFEN. Presently he is a member of technical committee of International Association of Science and Technology Education Development(IASTED) conference, Calgary, Canada. He is a reviewer for the International Journal of IEEE Transactions on Power Delivery and National Journal of Institution of Engineers - kolkata. His research and study interests include Power quality, Harmonics in power systems and multi phase systems..







Nonlinear State Control Optimized by Lyapunov and Riccati via Piecewise Linear Transformations Applied to Transmission Torque Converter Clutches

T. A. Perkins*, M.A. Zohdy**

Department of Electrical and Computer Engineering, Oakland University, Rochester, Michigan, U.S.A.

taperkin@oakland.edu*, zohdyma@oakland.edu**

<http://www.oakland.edu/ece>

ABSTRACT

Although the modern torque converter (TC) has many functions, this paper focuses on its ability to transmit torque while allowing the engine and gearbox to slip or rotate at different speeds. While this slipping greatly improves drivetrain feel, it can also reduce driveline efficiency due to friction. To improve efficiency, modern torque converters include a bypass Torque Converter Clutch (TCC), which allows the slipping to be reduced or eliminated at various operating conditions. This paper will investigate how to apply Piecewise Linearization to the plant model, so it can be controlled by switched gain controllers. These controllers are tuned by both Lyapunov and Riccati methods, and their performance evaluated against the conventional PID controlled model in terms of settling time, response and performance robustness.

Keywords: *Lyapunov; Riccati; Control theory; Torque Convert Clutch; Piecewise Linear; Measurement disturbance; Estimation methods.*

Nomenclature: *TC - Torque Converter; TCC - Torque Converter Clutch; AMT – Automated Manual Transmission; DCT - Dual Clutch Transmission; PID – Proportional Integrated Differential; PWL – Piecewise Linearization; State matrixes A, B, C, D; X – system states; Y – system outputs; R, Q and γ – tuning parameters for Riccati method*

1. INTRODUCTION

Automatic transmissions have been the choice of many drivers for their smooth operation since their introduction. Much of their smooth gear changes and isolation from engine vibrations is accomplished by fluid coupling in the torque converter between the engine and the gearbox. With increasing demand for vehicle gas mileage and efficiently, much attention has been directed to improving driveline efficiencies. One area to improve driveline efficiency is in

automatic transmissions. To address these new demands on automotive transmissions, modern vehicles have begun to adopt new types of technology, such as automated manual transmission (AMT), a subclass of AMTs the dual clutch operated transmission (DCT), and the constant velocity transmission (CVT) into the marketplace alongside traditional hydro-mechanical fixed-ratio gear gearboxes with TC. Although transmission efficiencies in AMT have been greatly increased by replacing TCs with friction clutches, their smoothness has gone down significantly because of the quantitative nature of friction clutch engagement. Much work has been done to control TC engagement by improving the driveline feel, but AMT are still no match for traditional TC equipped vehicles. [1,2,3,4,5] The objective of the powertrain designers is to control the drive clutch engagement to mimic the smooth and overdamped response of TC equipped vehicle with the underdamped nonlinear system behavior. Fuzzy Logic, optimal control and Kalman Filters control schemes have been used in an attempt to replace look up tables to achieve the desired smooth underdamped response however this paper will investigate using switched gain linear controllers. [6,7,8] CVTs, on the other hand, are known for their ultra-smooth underdamped operation, but their lack of torque capacity, “mush box” reputation and high cost have limited their penetration into the market place. [9]

To keep costs low and to maintain the current automatic transmission shift quality, most manufacturers have chosen to improve the efficiency of the more common torque converter/fixed ratio transmission found in most new vehicles sold in the United States by improving the TCC control. This paper discusses the advantages of improved dynamic modeling and control of these transmissions.



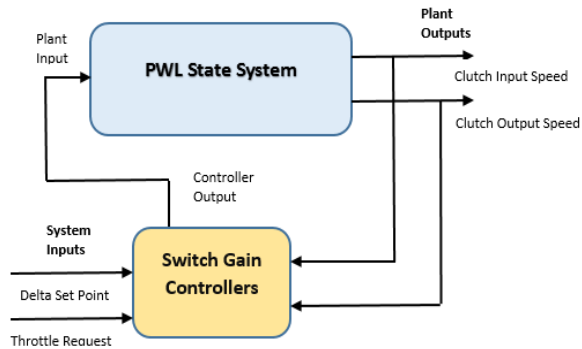


Figure 1 - 2 input, 2 output PWL plant model with Switch Gain Controller

In fixed-ratio automatic transmissions, one of the most important components is the torque converter and its fluid coupling between the engine output and the gear box input. This fluid coupling is necessary to allow the engine and transmission to turn at different speeds when the transmission is changing gears or when the vehicle is stopped. A secondary benefit of this slip, the speed differential between the clutch's input and output, is that it multiplies the engine torque as the slip speed increases. A third and less studied benefit of this slip is that it provides engine isolation from the drive train by absorbing the engine's rotational accelerations, or roughness, at low engine speeds.

Like all systems, there are tradeoffs; torque converters reduce driveline efficiency by diverting input power into heating the transmission fluid whenever the torque converter is slipping. TCCs reduce the slipping by bypassing the TC with a mechanical clutch as shown in figure 2. Although the TCCs improve efficiency, they do it at a cost: increased driveline harshness. [10,11] This harshness comes in two primary ways; the jerk 1) from locking up the clutch and 2) by transmitting underdamped engine vibrations. This paper focuses on the latter and how vibrations at lower engine RPMs are transmitted to the rest of the driveline. Although locking up the clutch improves efficiencies by eliminating torque converter slip and allowing the engine to run at a lower speed, this reduced internal combustion engine (ICE) often creates rotation speed fluctuations. These speed fluctuations are created when the individual cylinders ignite during their power stroke creating torque impulses. On a 4 cylinder four stroke ICE, there are two power strokes per revolution. With a typical lockup speed around 1500 RPM, this is a noticeable 50 Hz/second torque impulse causing fluctuations in engine speed. These speed fluctuations are dampened by the TC and to a lesser extent other driveline components. However, when the TC is bypassed, much of it is directly transmitted to the drivetrain, which increases vehicle vibration and noise. [10,12]

Clutch slipping control is a technique in which a partially engaged TCC is allowed to slip a limited amount thus preserving the damping between the ICE

and gear box while retaining most of the benefits of a locked up TCC. By keeping the slip to one or two hundred RPM, the ICE's speed variations can be absorbed by the slipping TCC, allowing it to be applied in a wider range of conditions while still meeting comfort objectives.

While the mechanics of how clutches slip and how they are controlled in this region of operation are well documented [13,14,15,16,17], this paper discusses how Piecewise Linear (PWL) plant models are used to design switched gain controllers. These controllers are then optimized to create faster and more robust systems than the current nonlinear models controlled with PID controllers.

This paper discusses piecewise linearization in section 2 and applies it to the nonlinear SimuLink model in section 3. Section 4 presents the baseline results compared with a new State controlled switched gain controller, shown in figure 1, for its settling time and robustness to model speed measurement noise. The new controller was optimized using two different methods, Lyapunov and Riccati, and their results compared to baseline model results. Section 5 presents the analysis of the findings and conclusions.

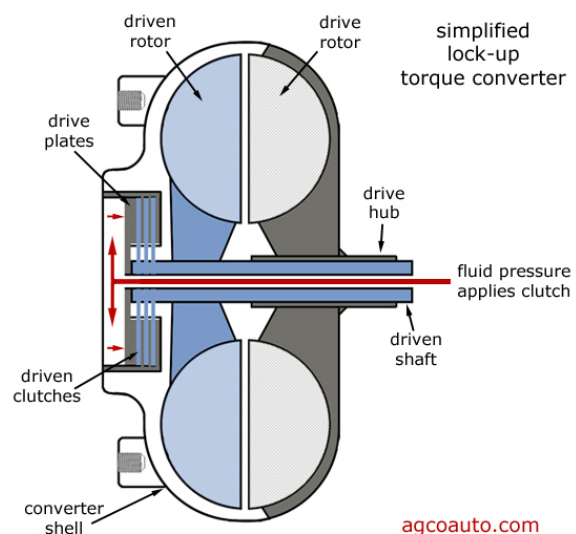


Figure 2 - Torque Converter Clutch Diagram

2. PIECEWISE LINEARIZATION (PWL) OF MIMO MODELS

One of the most difficult aspects of modeling complex, multi input multi output (MIMO) systems, such as an automobile's drive train, is classifying the relevant system states and the individual subsystem transfer functions. This paper addresses these challenges by creating a PWL model of the system and implements a controller for each segment's range of operation. Using the Lijun/Nianjiong/Daojun [10] description of the slipping control area, we can make assumptions that throttle input and vehicle speed



remain relatively constant in the slipping control area while clutch control input nonlinearly affects the amount of slip. [11] For simplicity, this paper does not address other slowly changing dynamic factors, such as fluid heat, clutch wear and vehicle load, which are dealt with in other papers. [18,19,20] The system in question can be described as follows:

$$\begin{aligned}\dot{\mathbf{x}}(t) &= \mathbf{f}(\mathbf{x}, \mathbf{u}) \\ \mathbf{y}(t) &= \mathbf{h}(\mathbf{x}, \mathbf{u}),\end{aligned}\quad (1)$$

where the input is \mathbf{u} (clutch control input), the states are TCC input acceleration, or engine acceleration, and TCC output acceleration, or transmission input acceleration, and are defined as $\dot{\mathbf{x}}$ and the output of the system is \mathbf{y} (TCC input speed and TCC output speed).

Then states \mathbf{x} and output \mathbf{y} are approximated by PWL estimates and represented by $\tilde{\mathbf{x}}$ and $\tilde{\mathbf{y}}$, respectively. These estimates are calculated by choosing an operating point of the function, finding its 1st derivative and using these to generate an estimate using the following form:

$$\tilde{\dot{\mathbf{x}}} = \tilde{\mathbf{f}}'(\mathbf{x}) * \mathbf{x} + \mathbf{b}.$$

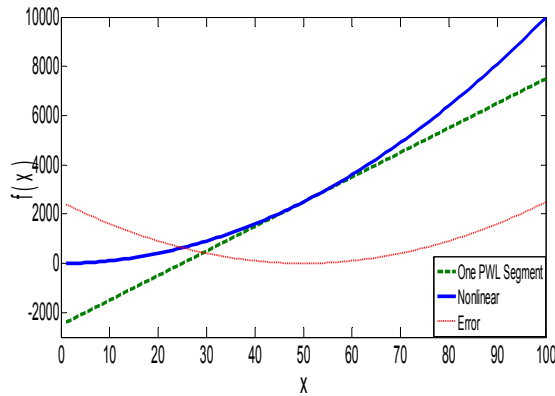


Figure 3 - PWL Estimation of $f(x)$ with 1 Segment

When this is expanded into segments, it is represented by:

$$\tilde{\dot{\mathbf{x}}} = \tilde{\mathbf{f}}'_i(\mathbf{x}) * \mathbf{x} + \mathbf{b}_i$$

where it is indexed by $i = 1, 2, 3, \dots, q$ for each segment and q is the number of segments. This method models the nonlinear function $\tilde{f}(x_1(t), x_2(t), \dots, x_n(t))$ as a collection of linear functions in the form:

$$\tilde{f}'(x_1(t), x_2(t), \dots, x_n(t)) = m_{i1}x_1(t) + b_i m_{i2}x_2(t) + \dots + m_{in}x_n(t) + b_i.$$

The resulting PWL state space equations are:

$$\dot{\tilde{\mathbf{x}}}(t) = \mathbf{A}_i \tilde{\mathbf{x}}(t) + \mathbf{B}_i \mathbf{u}(t) \text{ and} \quad (2)$$

$$\tilde{\mathbf{y}}(t) = \mathbf{C}_i \tilde{\mathbf{x}}(t) + \mathbf{D}_i \mathbf{u}(t), \quad (3)$$

with \mathbf{A}_i , \mathbf{B}_i , \mathbf{C}_i and \mathbf{D}_i representing the system, input, output and feed forward matrices.

An ideal example is the nonlinear electrical energy required to move the hydraulic solenoid actuating the clutch. Knowing that $W = i^2 * R$, where W the electrical power in watts, i is current and R is electrical resistance of the solenoid, it can be seen that the clutch force is nonlinearly proportional to the current. In this example, the nonlinear part of the

power equation is a function of $f(i) = i^2$. By inspection of $f(i)$, it is apparent that if $f(i)$ is linearized around $i = 1$, then a good estimate is $\tilde{f}(i) = i$. However, if it is linearized around $i = 10$, then the reader quickly sees $\tilde{f}(i) = i * 10$. Depending upon many factors, including application, observability of the function, noise, and robustness of the control, this error can quickly destabilize the controller. To reduce the error, the function can be broken into segments with each segment having its own linear model. Even with little practical experience, it is clear that as the number of segments, q , increases, the error of $\tilde{f}(i)$ becomes smaller. Following the processes described by Lowe (5), $\tilde{f}_i(i) = m_i x(t) + b_i$ with $i = 1, \dots, q$, (4) will be linearized from 0 to 100. Some rules that must be observed during PWL estimations are:

- The function must be differentiable.
- The center point of each segment must be found.
- Discontinuities should be avoided.
- A larger value of q equates to smaller estimate errors.

Example 1 with $q=1$

With only 1 segment, the center point is at $t = 50$. Differentiating $f(i)' = 2 * i$ and substituting $i = 50$ gives $f(i)' = 100$. Then calculate the value of f at the center point: $f(50) = 50^2$. The error we want to minimize is defined as $error = |\tilde{f}(i) - f(i)|$. From (4) $\tilde{f}(i) = f(i)' * x(i) + b$ and when solved for $i=50$, $b = -2500$. The linear estimate with $q=1$ of $f(i)$ is as follows:

$$\tilde{f}(i) = 100 * x(i) - 2500. \quad (5)$$

The results of the nonlinear response vs. the PWL model with one segment is shown in Figure 3.

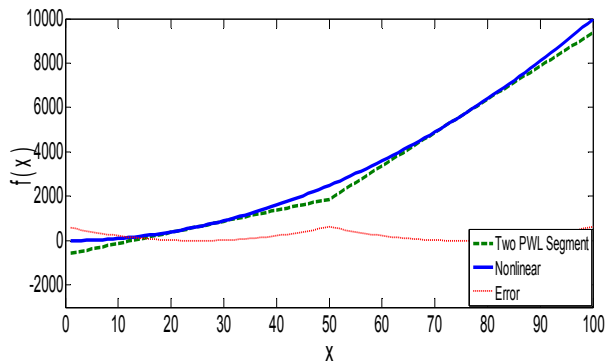


Figure 4 - PWL Estimation of $f(x)$ with 2 Segments

Example 2 with $q=2$

Similarly, if the t segment is divided into two segments, the center points are 25 and 75 yielding $\tilde{f}_1(i) = 50 * x(i) - 625$ for $0 < i \leq 50$ and $\tilde{f}_2(i) = 150 * x(i) - 5625$ for $50 < i \leq 100$ and is plotted as follows:

It can be shown that as q approaches infinity, the linearization error approaches 0 for all values of i . In the next section, apply this to the Torque Converter



Clutch model. The results of the nonlinear response vs. the PWL model with two segment is shown in Figure 4.

3. PIECEWISE LINEARIZATION OF CLUTCH MODELS

This paper's nonlinear TCC is modeled in MatLAB/Simulink in Figure 5. The Inputs are engine torque request and clutch engagement control, while the outputs are engine output speed and transmission input speed. From these outputs, clutch delta, vehicle speed and vehicle acceleration can be easily calculated.

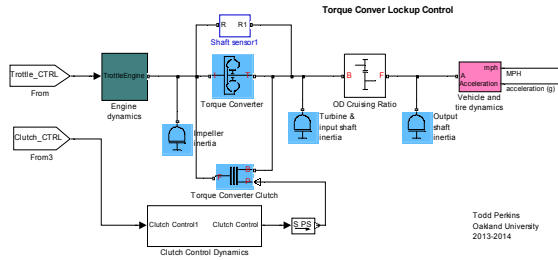


Figure 5 - Simulink Model of Nonlinear Drive train

For simplicity, this paper holds the throttle input constant at 4.5%. Because the nonlinear transfer function of the clutch control, system input, to the slip speed, system output, is not fully known, the TCC input and outputs at various steady state where recorded to create the data map in Table 1. This table plots the normalized Clutch Input (Column 1), Throttle Input (Column 2), TCC Input speed (Column 3), TCC Output speed (Column 4), and the assigned Segment number for the data range TCC Input speed (Column 5). These 35 data points were broken into operational segments and numbered 1 through 7. It should be noted that the difference between the engine speed and transmission input speed is the slip speed and is controlled by the clutch, creating a single input two output system.

The typical engine speed, TCC input, and transmission input speed, TCC output, are plotted against the normalized clutch control, the system input, in Figure 6.

For computation efficiencies and to exploit the common linear techniques, many methods have been used to estimate the response of these systems linearly [21,22]. This paper approximates the nonlinear function by dividing the function into linear segments using the Lowe/Zohdy method [23]. The superiority of this method over others is that any linear control design method may be used as long as it is continuous, thus eliminating the necessity of finding derivatives. By setting the output of the system, $\tilde{y}(t)$, equal to $\hat{x}(t)$, $C = \begin{bmatrix} 1 & 0 \\ 0 & 1 \end{bmatrix}$ and

$D = \begin{bmatrix} 0 \\ 0 \end{bmatrix}$ and $\hat{x}(t) = \hat{f}(u(t)) = m * u + b$ results in the new state equations:

$$\begin{aligned} \dot{\hat{x}}(t) &= A_i * (m_i * u + b_i) + B_i * u \\ \text{and } \tilde{y}(t) &= m_i * u + b_i \end{aligned} \quad (6)$$

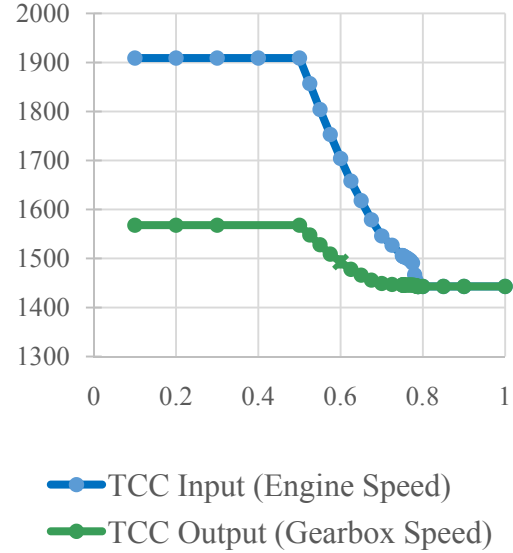


Figure 6 - Normalized Clutch Input vs. TCC Speeds (RPM)

where A_i and B_i are the PWL segmented state and input matrices segmented by $i = 1, 2, 3, \dots, q$, where q is the number of segments, and $m_i * u + b_i$ is the segmented linear approximation of x as a function of u . Where $\hat{f}(x_1(t), x_2(t), \dots, x_n(t))$ is a collection of linear functions and takes the form:

$$\begin{aligned} \hat{f}(x_1(t), x_2(t), \dots, x_n(t)) &= m_{i1}x_1(t) + b_i \\ &+ m_{i2}x_2(t) + \dots + m_{in}x_n(t) + b_i \end{aligned}$$

where f , m_i and b_i are independent for both the engine function and the transmission function yielding

$$\begin{aligned} f_{engine}(u) &= m_{engine_i} * u + b_{engine_i} \\ \text{and} \\ f_{trans}(u) &= m_{trans_i} * u + b_{trans_i} \\ i &= 1, 2, \dots, q. \end{aligned}$$

Observing the segmenting guidelines described in the Lowe/Zohdy paper, the nonlinear transfer function was segmented into 7 pieces indexed by q and linearized using the least squares error, LSE, method. When the original engine and transmission speed derivatives, \dot{x}_{engine} and \dot{x}_{trans} , are overlaid with their PWL estimations it is shown that the RPM error is within an acceptable few percent over most of the operating range of clutch control inputs in Figure 7. By linearizing the speeds in figure 1 as $\tilde{x} = m_x * u + b_x$ and substituting into equation (2), a new equation for their acceleration is:

$$\ddot{\tilde{x}} = A_i * (m_{x_i} * u + b_{x_i}) + B_i * u. \quad (7)$$

Setting this equal to the PWL estimations of the accelerations in figure 2, $\ddot{\tilde{x}} = m_{\ddot{x}} * u + b_{\ddot{x}}$, the state space matrix A_i and B_i can be solved algebraically as:



$$A_i = \frac{b_x}{b_x} \text{ and } B_i = m_x - \left(\frac{b_x}{b_x}\right) * m_x. \quad (8)$$

Using these State matrixes, a PWL model of the nonlinear drive trains was created. The results of both the nonlinear system and this model controlled by the original PID controller are shown in figure 8.

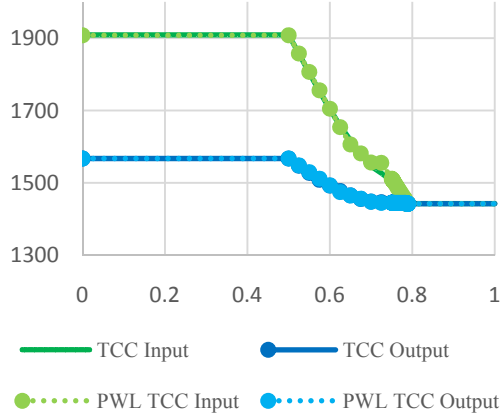


Figure 7 - Normalized Clutch Input vs. Nonlinear and PWL TCC Speeds (RPM)
PID Controlled Nonlinear and PWL Model

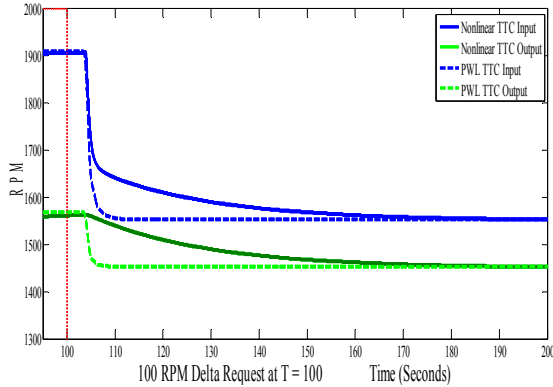


Figure 8 - Nonlinear and PWL Delta Speed Request Response w/PID Controller

LYAPUNOV OPTIMIZED CONTROLLER

Lyapunov optimized control schemes have been the primary technique used for controlling nonlinear systems since its adoption to computers over 30 years ago. [24,25,26] The basic principle behind Lyapunov's closed loop control law is that if the system can be defined in such a way that its energy is decreasing, a controller can be designed to make it stable at all times. This hinges on defining the energy as a positive and forcing its derivative to be negative definite or negative semi-definite thus ensuring the values are positive, decreasing and limited, creating an asymptotically stable response to any input.

Expanding on (1) above, we are replacing the input with $u = u(x)$, giving the following:

$$\dot{x}(t) = f(x, u(x)). \quad (6)$$

By restricting $u(x)$ to scalar gain k of the state, the input becomes

$$u = -kx \quad (7)$$

and the system of equation

$$\dot{x}(t) = Ax + Bu \quad \text{becomes} \quad (8)$$

$$\dot{x}(t) = Ax + B(-kx) \quad (9)$$

By setting (8) and (9) equal, we have derived a new closed-loop model system

$$\dot{x}(t) = A_m x \text{ with } A_m = A - Bk. \quad (10)$$

In practice, it is often advantageous to calculate the open loop system poles, the eigenvalues of A , to determine its stability, and then choose the closed loop system poles, the eigenvalues of A_m , to be 2 to 4 times faster, making sure they are all ≤ 0 to ensure closed loop stability.

The system's stability is ensured by the following Lyapunov equation:

$$PA_m + A_m^T P = -Q$$

Given any Q , a symmetric positive-definite matrix, there exists a symmetric positive-definite matrix P . The solution for finding P can be found in the literature [27,28].

The simulation results of this method to a 100 delta slip speed request are shown in figure 9.

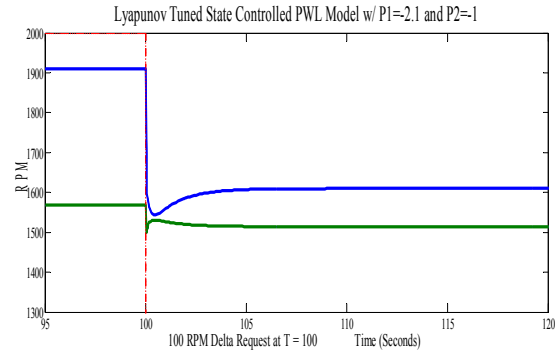


Figure 9 - Lyapunov Optimized Controller

RICCATI OPTIMIZED CONTROLLER

Another well-known approach to determining the state-variable feedback (SVFB) control gain k is the Riccati method to optimize the linear quadratic equation (LQE) by minimizing the cost function [24,25]:

$$J = \int_0^\infty \left[x^T \frac{Q}{2} x + \frac{1}{2\gamma} u^2 \right] dt. \quad (12)$$

This method differs from the Lyapunov method by not manually selecting poles by selecting tuning weight parameters Q , for system stability, and R , sometimes referred to as $\frac{1}{2\gamma}$, for input control effort.

Using these parameters and minimizing the cost function minimize the error thus creating a stable system. For simplicity, Q can be set to the I matrix of the appropriate size and R , or γ , adjusted to give the desired results [21,25]. Substituting the input from equation (7) yields:

$$J = \frac{1}{2} \int_0^\infty \left[x^T (Q + K^T \frac{1}{\gamma} K) x \right] dt. \quad (13)$$

This equation is used to optimize the controller, thus minimizing the error and ensure stability. Suppose there exists a matrix P that satisfies the following equity:

$$\frac{d}{dt} (x^T P x) = -x^T (Q + K^T \frac{1}{\gamma} K) x. \quad (14)$$

Substituting of (14) into (13) yields:

$$J = x^T(0) P x(0) \quad (15)$$



where the closed loop system's stability is assured by P remaining constant and $x(t)$ going to zero as t goes to infinity. By differentiating (14) substitution into (9) and algebraic manipulation, the algebraic Riccati equation (ARE) is found:

$$A^T P + P A + Q - 2\gamma P B B^T P = 0. \quad (14)$$

By selecting γ and Q is positive definite matrices and solving for the P matrix, the system is guaranteed asymptotic stable in its closed loop operation with a gain of $K = 2\gamma B^T P$. These results are shown in figure 10.

4. RESULTS

Figure 11 shows the results of the nonlinear model with PID control (a), the PWL model with PID (b), the PWL model with Lyapunov tuned poles at -1 and -2 (c) and the PWL model with Riccati tuned poles with $R=0.001$ (d). As shown in Figure 3, (a) and (b) are very similar, with only a few RPMs of error across the operating range and a settling time of about 5 seconds. Run (c) with the Lyapunov tuned poles controller reduces the settling time to about 2 seconds, but there is a significant amount of overshoot during the first second, which causes the clutch rapidly lockup and then release, causing a significant amount of driveline shock. The Riccati tuned controller in run (d) showed the best results with near instantaneous response to the control input and less than $\frac{1}{2}$ % of overshoot. This superior performance comes at a cost. The closed loop feedback gains are in the 10,000s. Depending upon the application and hardware, this may not be possible, resulting in a slower response with the gains in the 10s and 100s.

ROBUSTNESS

Another area evaluated in this paper is the controller's robustness to noise and changing inputs. The various controllers' ability to track are shown in figure 12 (25%) and figure 13 (45%) with noise at $\frac{1}{2}$ Hz added to the measurement of the output speed sensors. It is clearly seen in all figures that the PID controller is too slow to react to the RMS of the added noise but rather compensates for the minimum values of the combined inputs. This anomaly exaggerates the error, causing poor system performance, while the Lyapunov and Riccati controllers are able to react to the RMS of the signal thus minimizing the effect on the system's output. Figure 10 (c) shows the system has reached the limit where switch gain controllers can operate and they become unstable at these high noise levels

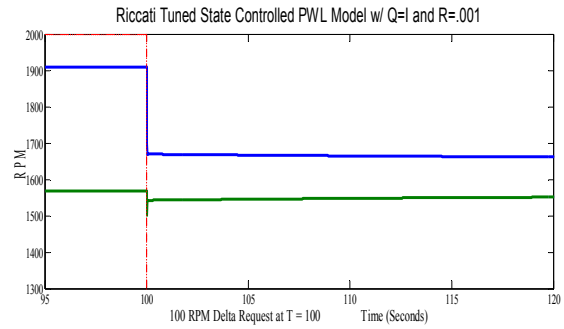


Figure 10 - Riccati Optimized Controller

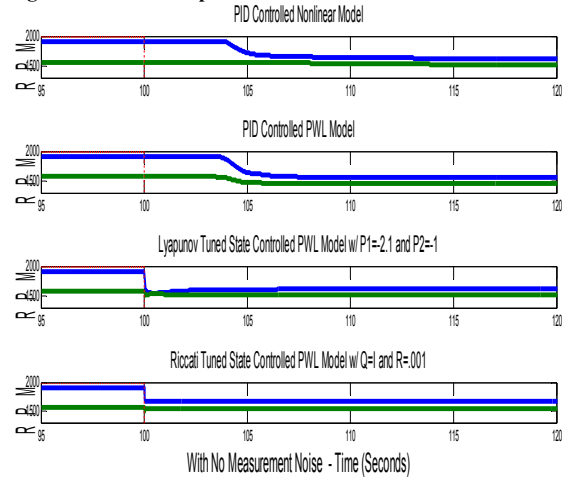


Figure 11 - TCC Input and Output Speeds Response to 100 RPM Delta Target:

a) PID Controlled Nonlinear Model, b) PID Controlled PWL Model, c) Lyapunov Optimized PWL Model, and d) Riccati Optimized PWL Model

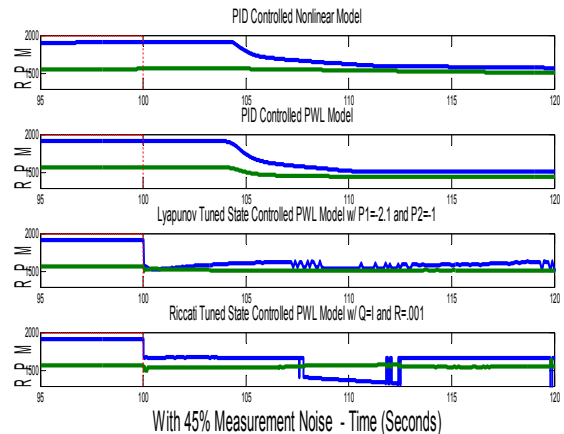


Figure 12 - TCC Input and Output Speeds Response to 100 RPM Delta Target with 25% Measurement Noise:

a) PID Controlled Nonlinear Model, b) PID Controlled PWL Model, c) Lyapunov Optimized PWL Model, and d) Riccati Optimized PWL Model



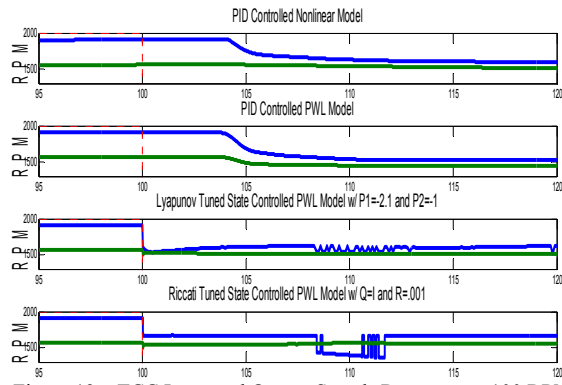


Figure 13 – TCC Input and Output Speeds Response to 100 RPM Delta Target with 45% Measurement Noise:

a) PID Controlled Nonlinear Model, b) PID Controlled PWL Model, c) Lyapunov Optimized PWL Model, and d) Riccati Optimized PWL Model

Clutch Control	Throttle %	TCC Input	TCC Output	Segment
0.1	4.5	1909	1568	1
0.2	4.5	1909	1568	1
0.3	4.5	1909	1568	1
0.4	4.5	1909	1568	1
0.5	4.5	1909	1568	1
0.525	4.5	1857	1548	2
0.55	4.5	1804	1528	2
0.575	4.5	1753	1509	2
0.6	4.5	1704	1493	2
0.625	4.5	1658	1478	2
0.65	4.5	1618	1466	3
0.675	4.5	1579	1456	3
0.7	4.5	1546	1449	3
0.725	4.5	1527	1447	3
0.75	4.5	1506	1446	3
0.751	4.5	1505	1446	4
0.752	4.5	1505	1446	4
0.753	4.5	1505	1446	4
0.754	4.5	1504	1446	4
0.755	4.5	1503	1446	4
0.76	4.5	1502	1446	5
0.765	4.5	1499	1446	5
0.77	4.5	1496	1446	5
0.775	4.5	1491	1446	5
0.78	4.5	1467	1445	5
0.7825	4.5	1457	1444	6
0.785	4.5	1450	1444	6
0.7875	4.5	1445	1443	6
0.788	4.5	1445	1443	6
0.7885	4.5	1444	1443	6
0.789	4.5	1443	1443	7
0.8	4.5	1443	1443	7
0.85	4.5	1443	1443	7
0.9	4.5	1443	1443	7
1	4.5	1443	1443	7

Table 1 – Nonlinear Model Response and PWL segments

5. CONCLUSIONS

Our results show that high order nonlinear system can be modeled using Piecewise Linearization with high degrees of accuracy and robustness. We also found that State controllers require fewer segments to accurately model and to control a PWL model in part because the PWL model segments where each tuned there specific operation regions and also because of the way the segments where selected caused general linearness between them. The advantage of the Riccati tuned controller over typical Lyapunov pole place controllers was shown by fast reactions to this high order nonlinear system. In practice, it may not be possible to duplicate the full benefit of this controller in a TCC because it requires higher gains in the 10,000s to overcome the 5 order electro-hydraulic control circuit in addition to the nonlinear clutch action. The rapid response of the Riccati controller may also be undesirable because its near infinite slope will create driveline shocks similar to the original quantitative state lockup TCC.

A separate area of mixed results is the controllers' robustness to noise. State optimized controllers do an excellent job responding to noise when the signal bounds keep the controller within the same operating segment, however significant state errors can be generated when the controller output or model when they are required to rapidly oscillate between segments to react to the noisy signal.

6. Reference

- [1] K. van Berkel, T. Hofman, A. Serrarens and M. Steinbuch, "Fast and smooth clutch engagement control for dual-clutch transmissions," *Control Eng. Pract.*, vol. 22, pp. 57-68, 1, 2014.
- [2] H. -. Jo, Y. -. Park, J. -. Lee, W. -. Jang, J. -. Park and W. -. Lim, "Study on the improvement of the shift characteristics for the passenger car automatic transmission," *Int. J. Veh. Des.*, vol. 23, pp. 307-328, 2000.
- [3] Y. Liu, D. Qin, H. Jiang and Y. Zhang, "Shift control strategy and experimental validation for dry dual clutch transmissions," *Mechanism and Machine Theory*, vol. 75, pp. 41-53, 5, 2014.
- [4] Dutta, B. Depraetere, C. Ionescu, G. Pinte, J. Swevers and R. De Keyser, "Comparison of two-level NMPC and ILC strategies for wet-clutch control," *Control Eng. Pract.*, vol. 22, pp. 114-124, 1, 2014.
- [5] J. Gauthier and P. Micheau, "A model based on experimental data for high speed steel belt CVT," *Mechanism and Machine Theory*, vol. 45, pp. 1733-1744, 11, 2010.
- [6] Chen Ran, C. Ran, S. Dongye and Sun Dongye, "Fuzzy neural network control of AMT clutch in starting phase," in 2008, pp. 712-715.
- [7] P. Dolcini, C. Canudas de Wit and H. Béchart, "Lurch avoidance strategy and its implementation in AMT vehicles," *Mechatronics*, vol. 18, pp. 289-300, 2008.



- [8] Q. Niu, "Clutch control during starting of AMT," *Procedia Engineering*, vol. 7, pp. 447-452, 2010.
- [9] N. Srivastava and I. Haque, "A review on belt and chain continuously variable transmissions (CVT): Dynamics and control," *Mechanism and Machine Theory*, vol. 44, pp. 19-41, 1, 2009.
- [10] Qian Lijun, Q. Lijun, Yang Nianjiong, Y. Nianjiong, W. Daojun and Wu Daojun, "Simulation of clutch slipping control of automatic transmission," in 2010, pp. 235-238.
- [11] M. Osawa, R. Hibino, M. Yamada, K. Kono and Y. Kobiki, "Application of h_{∞} control design to slip control system for torque converter clutch," in *Advances in Automotive Control 1995*, U. KIENCKE and L. GUZZELLA, Eds. Oxford: Pergamon, 1995, pp. 157-162.
- [12] Anonymous "Patent Issued for Hydrodynamic Torque Converter," *Journal of Technology*, pp. 2197, 2013.
- [13] J. Horn, J. Bamberger, P. Michau and S. Pindl, "Flatness-based clutch control for automated manual transmissions," *Control Eng. Pract.*, vol. 11, pp. 1353-1359, 12, 2003.
- [14] Y. Kamada, N. Wang, T. Kotanigawa, J. Kawabata, M. Araki and K. Mukaida, "Wet friction materials for continuous slip torque converter clutch — Fuel economy improvement of passenger cars equipped with automatic transmission —," *Tribology Series*, vol. 34, pp. 527-533, 1998.
- [15] P. Ompusunggu, P. Sas and H. Van Brussel, "Modeling and simulation of the engagement dynamics of a wet friction clutch system subjected to degradation: An application to condition monitoring and prognostics," *Mechatronics*, vol. 23, pp. 700-712, 9, 2013.
- [16] P. Ompusunggu, "On the derivation of the pre-lockup feature based condition monitoring method for automatic transmission clutches," *Mechanical Systems and Signal Processing*, vol. 46, pp. 114-128, 5/3, 2014.
- [17] J. D. Van de Ven and J. Cusack, "Synthesis and baseline testing of a digital pulse-width-modulated clutch," *Mechanism and Machine Theory*, vol. 78, pp. 81-91, 8, 2014.
- [18] M. Li, M. M. Khonsari, D. M. C. McCarthy and J. Lundin, "Parametric analysis for a paper-based wet clutch with groove consideration," *Tribol. Int.*, vol. 80, pp. 222-233, 12, 2014.
- [19] N. Lingesten, P. Marklund, E. Höglund, M. Lund, J. Lundin and R. Mäki, "Apparatus for continuous wear measurements during wet clutch durability tests," *Wear*, vol. 288, pp. 54-61, 5/30, 2012.
- [20] F. Riddar, Å. K. Rudolphi and S. Hogmark, "Wear study of field worn clutch actuators and evaluation of a model test," *Wear*, vol. 267, pp. 2269-2277, 12/1, 2009.
- [21] G. K. Lowe, "Nonlinear state estimation using piecewise linear modeling with simple and complex applications in electro-mechanical systems," 2011.
- [22] S. Omekanda, "Nonlinear control of multivariable modern powertrain systems using piecewise linear and extended observers," 2014.
- [23] M. A. Z. G.K. Lowe, "Modeling nonlinear systems using multiple piecewise linear equations," *Nonlinear Analysis: Modelling and Control*, , , , 451-458, vol. Vol. 15, pp. 451-458, 2010.
- [24] S. Ge, "Lyapunov design," in *Control Systems, Robotics and Automation*, Vol. XIII ed. Anonymous
- [25] R. Padhi, "Pole Placement Control Design," Indian Institute of Science - Bangalore, Dept. of Aerospace Engineering, Lecture - 21
- [26] Marinescu, "Output feedback pole placement for linear time-varying systems with application to the control of nonlinear systems," *Automatica*, vol. 46, pp. 1524-1530, 9, 2010.
- [27] V. Kucera, "A review of the matrix Riccati equation," *Institute of Information Theory and Automation AS CR*, vol. Vol. 9, pp. 61, 1973.
- [28] F. L. Lewis, "Linear Quadratic Regulator (LQR) State Feedback Design, EE 4343/5329 - Control System Design Project Lecture 11," University of Texas Arlington, 2008, 1998.



Biographies:



TODD A. PERKINS is a Ph.D. student in the Electrical and Computer Engineering department. He earned his B.S. in Electrical Engineering at Howard University. After spending nearly 20 years in the broadcast, automotive and telecommunications

industry, he left to pursue a M.S. and Ph.D. at Oakland University so he could teach engineering. Under the 'coaching' of Dr. M.A. Zohdy, his working dissertation title is *Adaptive Nonlinear Control of Clutch Engagement in Modern Automotive Transmissions*. His current research includes piecewise linear (PWL) modeling, State Space modeling, nonlinear Adaptive Controls and Simulink modeling. Todd enjoys working as a Teaching Assistant and teaching *Science, Technology, Engineering and Math* (STEM) outreach camps to K-12 students. In this spare time -- as if Ph.D. students have any -- Todd enjoys traveling, DJing house music, motorcycles and anything automotive related.



Mohamed A. Zohdy was born in Caro, Egypt. He received a B.Sc. degree in Electrical Engineering from Cairo University, Egypt, in 1968. He received his M.S. and Ph.D. degrees in Electrical Engineering from the University of Waterloo, Canada, in 1974, and 1977 respectively. He is currently a Professor at Oakland University in Rochester Hills, Michigan, U.S.A. His research interests are in areas of Controls and Soft Computing.







Dynamics of Metallic Particle movement in a Gas Insulated Substation Employing SF₆/N₂, SF₆/CO₂ and SF₆/Air Dielectric Gas Mixtures

Mr. P Srinath Rajesh¹, Dr.J Amarnath²,

¹ Department of EEE, Adams Engineering College, Paloncha, India.

² Department of EEE, JNTUH College of Engineering, Hyderabad, India.

¹ srinathrajesh@gmail.com, ² amarnathjinka@yahoo.com,

Abstract

From the past studies the breakdown strength of SF₆ is exceptionally subjected to nonlinear electric fields in conjunction with metallic particles, consequently this effects provokes drop in the breakdown strength beyond its limits. In addition to this the SF₆ gas is a hothouse gas rouse the global warming, employing this gas is extremely undesirable. As a consequence there is a need to find alternate solution to this gas one such alternative is to use gas mixtures such as SF₆/N₂, SF₆/Air, SF₆/CO₂, SF₆/Kr, SF₆/Ar having supreme dielectric characteristics. In this paper Metallic Particles movement is analyzed, compared and presented the results of SF₆/N₂, SF₆/CO₂ and SF₆/Air gas mixtures in a Single Phase Gas Insulated Substation.

Keywords: Gas Insulated Substation, gas mixture, metallic particle, hothouse gas.

1. Introduction

In the early stages of nineteen seventies the gas insulated substation were made available to the end users to get the advantage of its size and inconsiderateness to atmospheric circumstance. The gas insulated substation has outstanding reliability and had given solutions to worlds power conveyance challenges [7]. SF₆ gas is commonly used in the high-voltage electrical engineering for the reason that it is a praiseworthy dielectric and has a tremendous electrical arc interrupting characteristic, making it the most suitable gas for substation applications. However, there is just one difficulty; it is a hothouse gas with a lofty Global Warming Potential GWP [1].

Diluting SF₆ gas mixtures are of specific interest as assured reduction of the environmental effects can be achieved. Various characteristic of the insulation behavior of SF₆ and N₂ mixtures have been published [6]. So much of research has been done on sf₆ gas mixtures for replacing the sf₆, some of those mixture gas had given better dielectric characteristics the sf₆ but they are toxic in nature. Examinations were done on SF₆/N₂ gas mixture with lower proportion of SF₆ and higher proportion of N₂. The most favorable process was needed

to find the optimum solution for fixing the percentage of the SF₆. some author had stated that with 12-25% of SF₆ in a gas mixture can give same insulating capabilities of 75-85 % of pure SF₆.

It is identified that the dielectric strength of the gas insulated substation is affected by the presence of metallic particles which are free to move due to applied electric field in the compressed gas. These particles may have insulating or conducting characteristics which are originated during the transportation, assembling of substation or during switching actions. Movement of the insulating particles does not affect the dielectric strength of the gas but the movement of conducting particles leads to micro discharges and electric stress of high magnitude [3-6] which leads to breakdown of the system.

The work stated in this paper deals the dynamic of behaviour of metallic particles in a gas insulated substation with various SF₆ gas mixtures. A software program is developed for computing the conducting particle movement for different proportions of gas mixture at a specific electric field using an advanced C++ language. In a single phase gas insulated substation a fixed geometry of copper and aluminium particles of wire type were considered to determine the radial movement of the particle. To solving the motion equation analytical method has been adopted for various gas mixtures.

2. Modelling Technique

The figure 1 shows the parallel conductor bus of gas insulated substation enclosed in an enclosure packed with mixture of SF₆ and other gas is considered for the study.

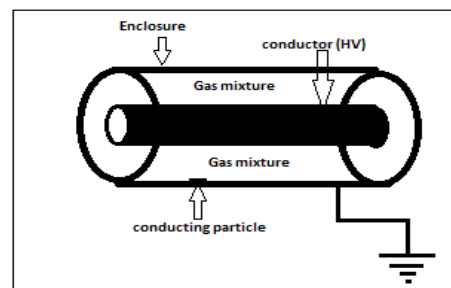


Figure 1



A conducting particle of wire type is supposed to be at rest on the surface of the enclosure till a sufficient voltage is applied to pick up the conducting particle. After gaining sufficient charge and surmounting its own weight and drag forces, conducting particle winches up and progress in the direction of the applied field. Numerous of parameters were considered to determine the particle motion equation, for instance restitution coefficient, Reynolds number, drag coefficient, viscosity of gas and so on. though several authors have expression for wire like particles but the equations are taken from the work of Felici [2].

When a conducting particle is subjected to the electric field in a gas insulated substation it attains an electric charge and undergoes an electrostatic force. If this force surpasses the gravitational force, the conducting particle is picked up from the enclosure and a zig zag movement is detected[8].

Ignoring the image charges due to the existence of enclosure grounding, the electrostatic force F_e is proportional to the charge

$$F_e = Q_w \cdot E_f \quad 1$$

For a wire like particle resting on the surface of the enclosure [5, 6, 7], for $l \gg r$, the charge Q_w is

$$Q_w = \frac{\pi \epsilon_0 l^2 E_f}{\ln \frac{2l}{r} - 1} \quad 2$$

A conducting free particle moving in the applied electric field is subjected to Electrostatic force (F_e), force due to drag (F_d) and force due to gravitation of earth (F_g). The free conducting particle motion of mass (m) is computed using the equation of motion

$$m \frac{d^2 y}{dt^2} = F_e - F_d - F_g \quad 3$$

The Reynolds number and the viscosity of the two gas mixture is required for calculating the motion equation. The above equation (3) leads to non-linear equation which is solved using iterative technique such as Runge-Kutta fourth Order Method.

3. Simulation of Particle motion

Analytical method is used for calculating electric field and charge acquired using equation (1.1) and (1.2) based on work of [2, 5 and 8]. The free conducting particle movement given in equation (1.3) is simulated using the analytical method. Using advanced c++ programming, simulation of motion equation of free conducting wire particles with 15mm length and 0.5mm radius is carried out in gas insulated substation for 132 kV, 145kV and 220 kV applied voltages. The enclosure radius of 88 mm and conductor radius of 33 mm is considered for the simulation. It is assumed that Aluminum and Copper particles of wire type were present in the gas insulated substation

4. Results and Discussion

From the figures 2 and 3 the maximum movement of Aluminum and Copper particles for 20% SF6 in SF₆/N₂,

SF₆/CO₂ and SF₆/Air mixture for 132 KV, 145KV and 220KV can be known. The maximum movement obtained for Al particles and Cu particles for 132 kV is 11.876097, 11.627509, 11.889343 and 2.220426, 2.227485, 2.250473. The maximum movement obtained for Al particles and Cu particles for 145 kV is 14.608354, 15.656908, 14.845436 and 2.778246, 2.778473, 2.832792. The maximum movement obtained for Al particles and Cu particles for 220 kV is 29.648418, 30.830299, 30.822065 and 9.44219 and 9.558602.

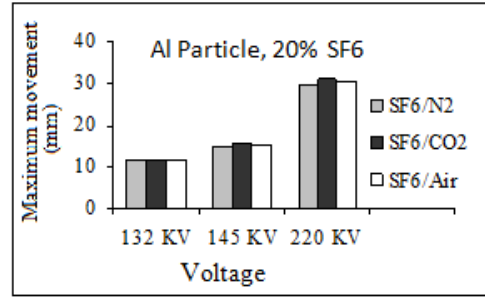


Figure 2

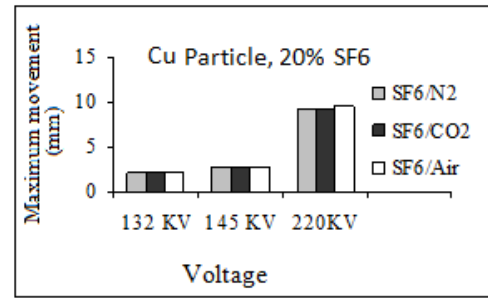


Figure 3

From the figures 4 and 5 the maximum movement of Aluminum and Copper particles for 40% SF6 in SF₆/N₂, SF₆/CO₂ and SF₆/Air mixture for 132 KV, 145KV and 220KV can be known. The maximum movement obtained for Al particles and Cu particles for 132 kV is 12.087142, 11.644285, 12.737603 and 2.219076, 2.287596, 2.209517. The maximum movement obtained for Al particles and Cu particles for 145 kV is 15.698053, 14.822464, 14.63584 and 2.843645, 2.783404, 2.788052. The maximum movement obtained for Al particles and Cu particles for 220 kV is 30.600975, 30.605444, 30.880322 and 9.540246, 9.581879 and 5.644269

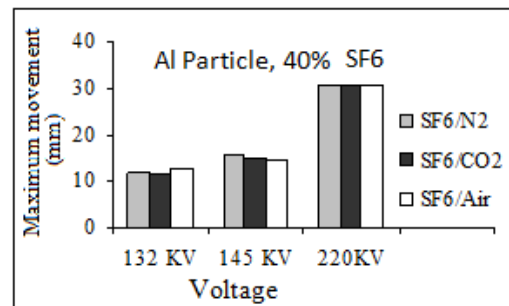


Figure 4



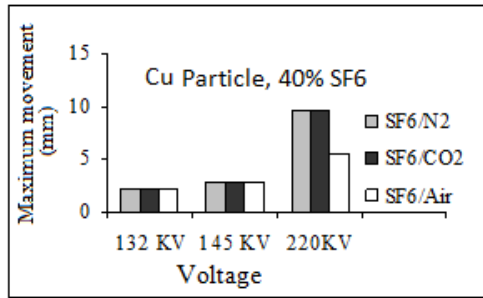


Figure 5

30.666139, 31.39572 and 9.552808, 8.310761 and 9.587192.

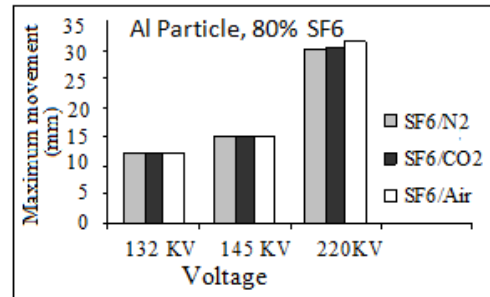


Figure 8

From the figures 6 and 7 the maximum movement of Aluminum and Copper particles for 60% SF6 in SF₆/N₂, SF₆/CO₂ and SF₆/Air mixture for 132 KV, 145KV and 220KV can be known. The maximum movement obtained for Al particles and Cu particles for 132 kV is 11.897035, 11.897187, 11.892382 and 2.224117, 2.224119, 2.220146. The maximum movement obtained for Al particles and Cu particles for 145 kV is 15.126985, 14.842751, 14.844956 and 2.833687, 2.806137, 2.778574. The maximum movement obtained for Al particles and Cu particles for 220 kV is 31.564141, 31.100422, 31.222407 and 9.631787, 9.473286 and 9.354718

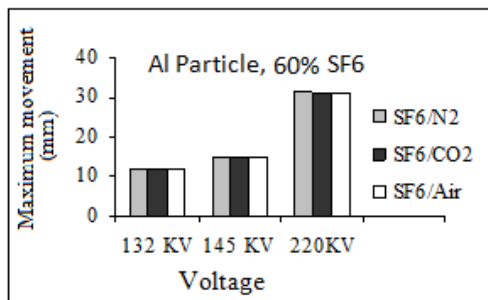


Figure 6

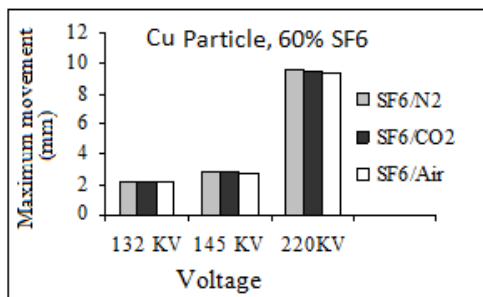


Figure 7

From the figures 8 and 9 the maximum movement of Aluminum and Copper particles for 80% SF6 in SF₆/N₂, SF₆/CO₂ and SF₆/Air mixture for 132 KV, 145KV and 220KV can be known. The maximum movement obtained for Al particles and Cu particles for 132 kV is 11.935179, 12.140633, 11.979409 and 2.22292, 2.23103, 2.288991. The maximum movement obtained for Al particles and Cu particles for 145 kV is 14.939284, 14.873562, 14.988114 and 2.837505, 2.831574, 2.841872. The maximum movement obtained for Al particles and Cu particles for 220 kV is 30.314663,

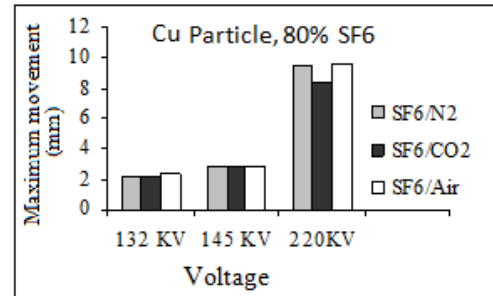


Figure 9

From the figures 10 and 11 the maximum movement of Aluminum and Copper particles for 100% SF6 in SF₆/N₂, SF₆/CO₂ and SF₆/Air mixture for 132 KV, 145KV and 220KV can be known. The maximum movement obtained for Al particles and Cu particles for 132 kV is 11.95468 and 2.192154. The maximum movement obtained for Al particles and Cu particles for 145 kV is 14.939284 and 2.834764. The maximum movement obtained for Al particles and Cu particles for 220 kV is 31.384289 and 9.595386.

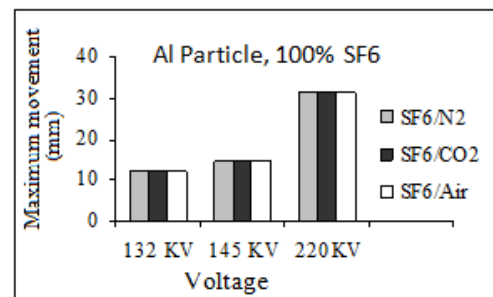


Figure 10

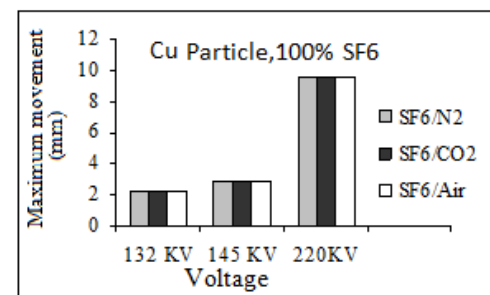


Figure 11



5. Conclusion

It is observed that, as the applied voltage increases the particle movement increases. It is also observed that the Aluminum and Copper particles movement is almost identical for 20%, 40%, 60%, 80% SF₆ and 100% SF₆ in gas mixtures mentioned. In order to reduce the environmental effects occurred due to SF₆ gas utilization in electrical industry as insulating medium particularly in Gas insulated substations, 20% SF₆ in gas mixture can be used as insulating medium in the gas insulated substation. Among the gas mixtures given above SF₆/N₂ gives the better results in terms of economy, dielectric capability and environment issues.

6. Acknowledgements

The authors are very much thankful and gratified to the authorities of JNTUH, Hyderabad, and Adams Engineering College, Paloncha, India for their kind support and encouragement

7. References

- [1] United Nation Framework Convention on Climate Change, UNFCCC"IPCC Second Assessment Report", 1966.1
- [2] N.J.Felici; "Forces et charges de petits objets en contact avec une electrode affectee d'un champ electrique"; Revue generale de l' electricite, pp. 1145-1160, October 1966
- [3] A.H. Cookson, P.C. Bolin, H.C. Doepken, R.E. Wootton, C.M.Cooke and J.G.Trump, "Recent Research in the United States on the Effect of Particle Contamination Reducing the Breakdown Voltage in Compressed Gas Insulated System", Int. Conf. On Large High Voltage System; Paris, 1976.
- [4] J. R. Laghori and A. H. Qureshi, "A review of particle contaminated gas breakdown. IEEE Transactions on Electrical Insulation, Vol. EI- 16 No. 5, October 1981
- [5] H.Anis and K.D. Srivastava, "Breakdown Characteristics of Dielectric Coated Electrodes in Sulphur Hexafluoride Gas with Particle Contamination", Sixth Intern. Sympos High Voltage Engineering, Paper No. 32.06, New Orleans, LA, USA. 1989.
- [6] L.G. Christophorou, R.J. Brunt; ".SF₆/N₂ mixtures, Basic and HV Insulation properties, IEEE Transactions, Dielectrics and Electrical Insulation 2 (5), October 1995 pp952-1002.
- [7] E. Mikes, Ch. Tschannen, et al. "GIS substation extensions and upgrades "CEPSI Paper T1-068, 2000, Manila, Philippines.
- [8] G.V.Nagesh Kumar J.Amarnath, B.P.Singh,K.D.Srivatsava., "Influence of Power frequency and Impulse voltages on Particle movement in Gas Insulated Bus duct (GIB) with epoxy coatings". at National Seminar on Insulating materials for the Power Industry, organized by Central Power Research Institute, Bangalore during 26-27th August, 2004

Biographies



P.Srinath Rajesh graduated from J.N.T. University, Hyderabad in 2003 and post graduated from ANU, Guntur in 2006. Presently he is pursuing Ph.D from J.N.T. University, Hyderabad. Presently he is working as Associate Professor in Adams Engineering College, Paloncha, India. His research area includes Power system Operation and control, High Voltage Engineering, FACTS, Renewable energy sources.



J.Amarnath graduated from Osmania University in the year 1982, M.E from Andhra University in the year 1984 and Ph.D from J.N.T. University, Hyderabad in the year 2001. He is presently Professor in the Department of Electrical and Electronics Engineering, JNTU College of Engineering, Hyderabad, India. He presented more than 60 research papers in various national and international conferences and journals. His research areas include Gas Insulated Substations, High Voltage Engineering, Power Systems and Electrical Drives.



Table1: Particle movement for 0% sf6 in gas mixture for different voltages

S. No	0% SF ₆		132 KV		145 KV		220KV	
			AL	CU	AL	CU	AL	CU
1	Particle movement in mm	SF ₆ /N ₂	11.949015	2.221941	14.966857	2.843424	31.320617	9.621646
2		SF ₆ /CO ₂	12.192864	2.232327	15.120603	2.751012	30.707943	5.653463
3		SF ₆ /Air	11.918994	2.226604	14.432084	2.787783	31.2009	9.615728

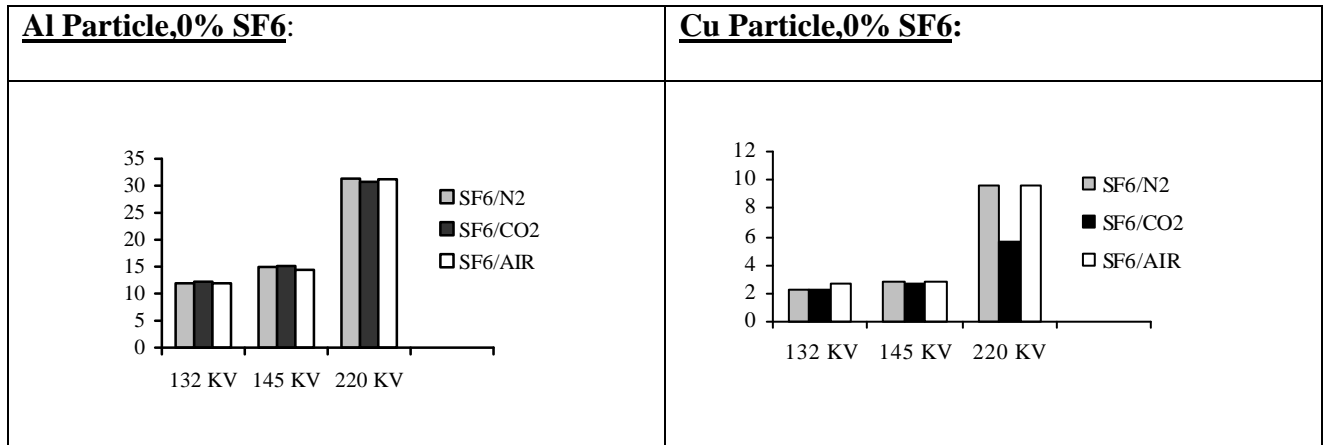


Table 2: Particle Movement for 20% sf6 in gas mixture for different voltages

S. No	20% SF ₆		132 KV		145 KV		220KV	
			AL	CU	AL	CU	AL	CU
1	Particle movement in mm	SF ₆ /N ₂	11.876097	2.220426	14.608354	2.778246	29.648418	9.429732
2		SF ₆ /CO ₂	11.627509	2.227485	15.656908	2.778473	30.830299	9.444219
3		SF ₆ /Air	11.889343	2.250473	14.845436	2.832792	30.822065	9.558602

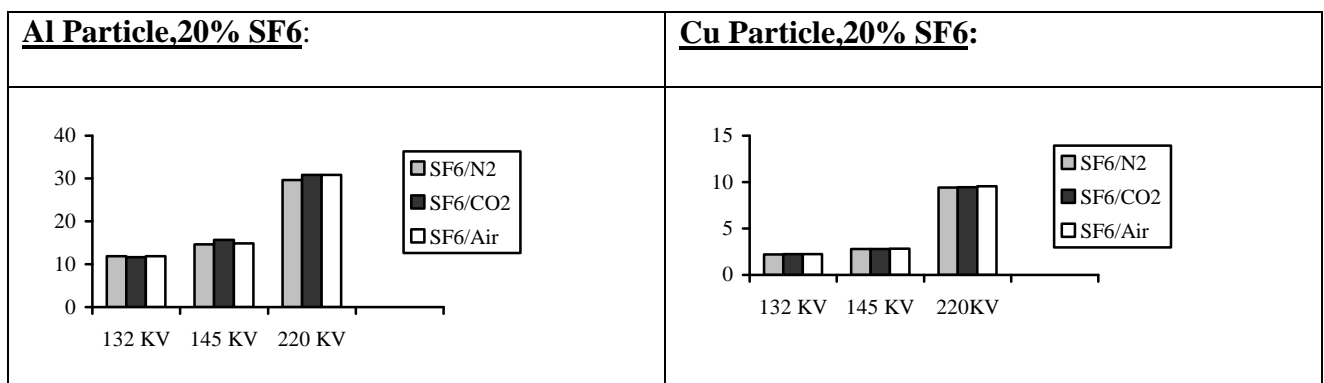


Table 3: Particle movement for 40% sf6 in gas mixture for different voltages

S. No	40% SF ₆		132 KV		145 KV		220KV	
			AL	CU	AL	CU	AL	CU
1	Particle movement in mm	SF ₆ /N ₂	12.087142	2.219076	15.698053	2.843645	30.600975	9.540246
2		SF ₆ /CO ₂	11.644285	2.287596	14.822464	2.783404	30.605444	9.581879
3		SF ₆ /Air	12.737603	2.209517	14.63584	2.788052	30.880322	5.644269



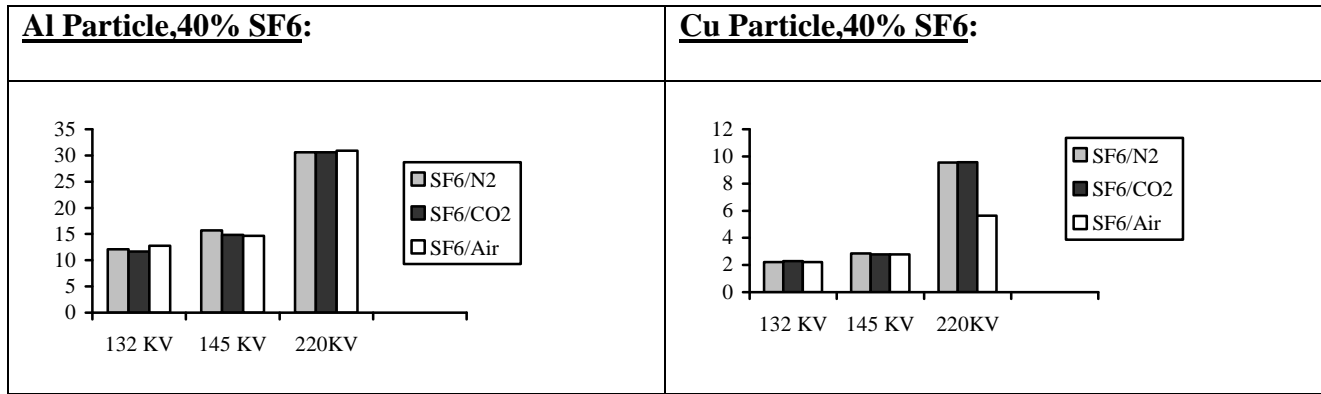


Table 4: Particle movement for 60% sf6 in gas mixture for different voltages

S. No	60% SF ₆		132 KV		145 KV		220KV	
			AL	CU	AL	CU	AL	CU
1	Particle movement in mm	SF ₆ /N ₂	11.897035	2.224117	15.126985	2.833687	31.564141	9.631787
2		SF ₆ /CO ₂	11.897187	2.224119	14.842751	2.806137	31.100422	9.473286
3		SF ₆ /Air	11.892382	2.220146	14.844956	2.778574	31.222407	9.354718

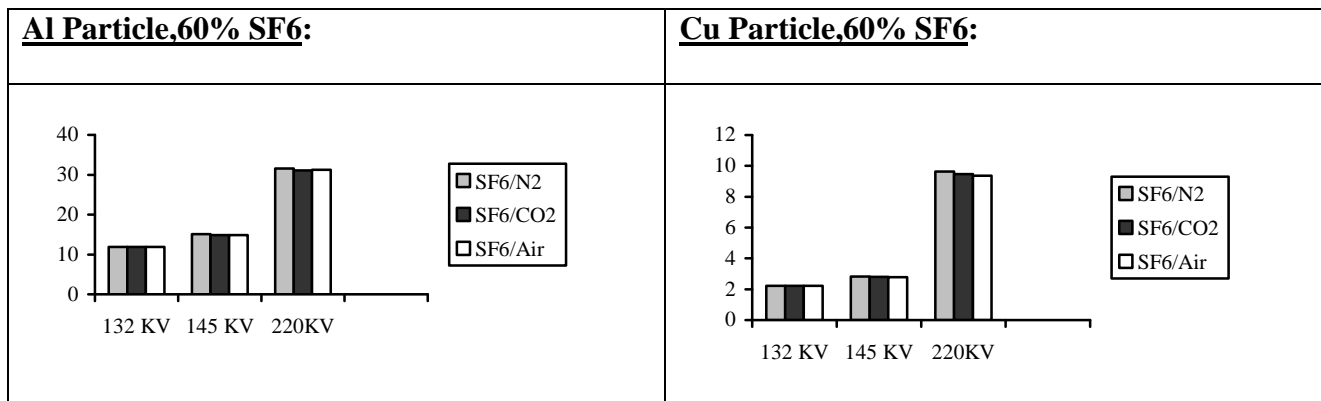


Table 5: Particle movement for 80% sf6 in gas mixture for different voltages

S. No	80% SF ₆		132 KV		145 KV		220KV	
			AL	CU	AL	CU	AL	CU
1	Particle movement in mm	SF ₆ /N ₂	11.935179	2.22292	14.939284	2.837505	30.314663	9.552808
2		SF ₆ /CO ₂	12.140633	2.23103	14.873562	2.831574	30.666139	8.310761
3		SF ₆ /Air	11.979409	2.288991	14.988114	2.841872	31.39572	9.587192

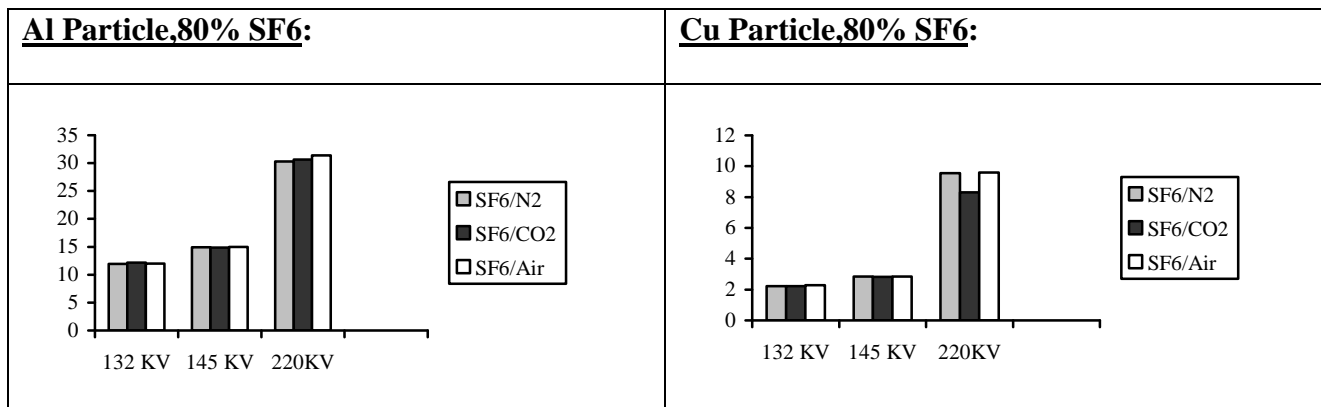
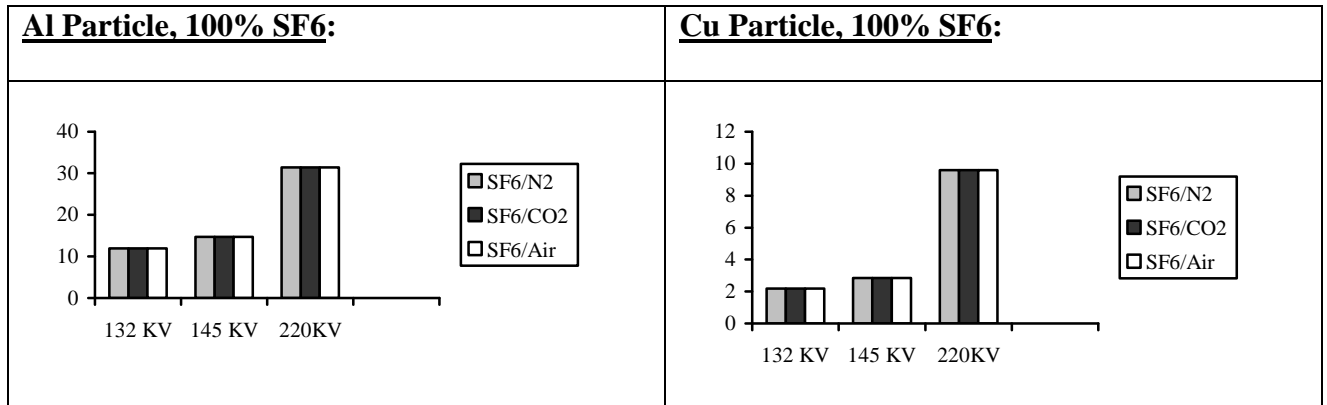


Table 6: Particle movement for 100% sf6 in gas mixture for different voltages

S. No	100% SF ₆		132 KV		145 KV		220KV	
			AL	CU	AL	CU	AL	CU
1	Particle movement in mm	SF ₆ /N ₂	11.95468	2.192154	14.695567	2.834764	31.384289	9.595386
2		SF ₆ /CO ₂	11.95468	2.192154	14.695567	2.834764	31.384289	9.595386
3		SF ₆ /Air	11.95468	2.192154	14.695567	2.834764	31.384289	9.595386







Numerical Study of Auto-Control and Stabilization of Pulse Repetition Rate of Passively Q-Switched Laser Systems

Jala M. El-Azab Hamed M. Kandel and Mohamed A. Khedr
National Institute of Laser Enhanced Sciences, Cairo University, Egypt.
jala@niles.edu.eg

Abstract

In this work, a simplified technique to control and stabilize the passively Q-switched laser pulses is proposed and denoted by automatic pulsed pumping technique. The technique is applied to a diode-pumped Yb:YAG laser passively Q-switched by Cr⁴⁺:YAG as saturable absorber by numerically solving the coupled rate equations describing the system. The technique is based on the detection of the generated Q-switched pulses which alter the pumping power either to be switched off or set to a lower value depending on the selected modulation depth.

The system was pumped using different pumping techniques; continuous, pulsed pumping and automatic pulsed pumping in order to compare the time stability of the generated Q-switched pulses. The proposed technique has shown a good control of the pulse repetition rate of Q-switched pulses with high stability. The technique allowed high pulse repetition rate as similar to the pulsed pumping scheme while maintained the time stability of the continuous pumping scheme.¹

Keywords: *Q-switched lasers; pulse repetition rate; time stability; pulsed pumping.*

Nomenclature:

ϕ	the photon density in the laser cavity,
t_r	the cavity round-trip time,
σ	the stimulated emission cross-section of the laser crystal,
σ_g	the absorption cross-section of ground state of the saturable absorber,
σ_e	the absorption cross-section of the excited state,
N	the population inversion density of the gain medium,
n_g and n_e	the absorber ground state and excite state population density respectively,
n_{s0}	the total population density of the saturable

	absorber,
l	the length of the laser crystal,
l_s	the length of the saturable absorber,
l'	the optical length of the laser cavity,
R	the reflectivity of the output coupler,
L	nonsaturable intracavity round-trip dissipative optical loss,
W_p	the volumetric pump power,
c	the speed of the light,
γ	the inversion reduction factor,
τ	the lifetime of the upper laser level of the gain medium
τ_s	excited-state lifetime of the saturable absorber,
$W_{pn}(t)$	the normalized volumetric pump power ,
$\phi_n(t)$	the normalized photon density,
$N_n(t)$	the normalized population inversion density of gain medium,
md	the modulation depth of the pulsed pumping power,
T	the period of pulsed pumping power.

1. Introduction

Diode pumped Q-switched lasers are currently used to produce pulses with high peak power at high repetition rates and short nanosecond pulse widths. These types of lasers are used in different applications such as medicine, material processing and military.

Q-switching can be established by either active or passive techniques. Although the active Q-switching provides higher power extraction, higher control on the repetition rate and lower time jitter, it is more complex and expensive than the passive Q-switching [1].

In the past, passive Q-switch element was first implemented by organic dye cells [2]. Due to poor durability of dye cell (degradation of dye) and low thermal limit of plastic material, it was replaced by doped crystals which provide higher power and better reliability [3]. The first new material was F₂:LiF color center crystal [2]. Then, Cr-doped crystals showed more photochemical and thermal stability [4]. Different crystals were involved with Chromium ions (Cr⁴⁺) such as Cr⁴⁺:YAG, Cr⁴⁺:GSGG and Cr⁴⁺:YSO as they have favored

¹ This study has been implemented at National Institute of Laser Enhanced Sciences, Cairo University, Giza, Egypt.



characteristics such as large absorption cross section, low saturable intensity at the lasing wavelength. Therefore, the Cr-doped crystals became promising Q-switching elements due to their low cost, long life, compactness.

Cr⁴⁺:YAG is the most of attractive saturable absorber due to the favorable chemical, thermal and mechanical properties of YAG host as well as its high absorption cross section of laser wavelengths centered at 410, 480, 640 and 1050 nm [5-6].

Other solid-state saturable absorbers such as Semiconductor Saturable Absorber (SESAM), GaAs wafers, and Saturable Bragg Reflector (SBR), are also available and investigated in many previous works [7-8]. Thence, solid-state Q-switched lasers are a good candidate in many applications due to their compactness, flexibility and reliability.

Most of previous work have studied diode pumped Nd-based lasers using Cr⁴⁺:YAG as a Q-switch element. This passive Q-switching combination was very attractive due to their highly stable phototropic centers and thermal conductivity [9]. Lot of work have been reported for modeling of passively Q-switched lasers with Cr⁴⁺:YAG as saturable absorber to determine pulse energy, peak power, pulse width, polarization, and thermal behavior [4,10-14].

The stabilization of pulse to pulse time, also referred to as time jitter, is a crucial requirement for many applications such as remote sensors, range finders or three dimensional scanners, Laser Induced Breakdown Spectroscopy (LIBS), particle flow measurements and defense [3,5,9,15-18]. Therefore, different techniques have been proposed to minimize the time jitter. These techniques were either introducing different operating conditions for active medium, saturable absorber and cavity length or modifying the system configuration. These techniques will be discussed in more details in Section 2.

In the last decade, passively Q-switched Yb:YAG lasers using Cr⁴⁺:YAG have been reported due to its simple energy level scheme, long upper laser level lifetime (951μsec) [7,19] which is suitable for storing energy and Q-switched pulse generation. In addition, it has low quantum defects which decrease heat generation during lasing three times less than Nd-based laser systems [20] and hence higher pumping efficiency [5]. The lower stimulated emission cross section of Yb:YAG increases the saturation fluence and the stored energy required for bleaching the Q-switch element which yield to shorter pulse length higher energy pulse and higher extraction efficiency. Besides, the large absorption cross-section tolerates the pumping laser wavelength [5,21]. Q-switched Yb:YAG laser was also realized by using GaAs wafer as saturable absorber [7,22].

In this work, the Yb:YAG laser Q-switched by Cr⁴⁺:YAG as saturable absorber was numerically investigated. The coupled rate equations describing the photon density, population inversion density of the active medium and the ground state population density of the saturable absorber were solved using 4th order Runge-Kutta algorithm. Using both continuous and pulsed pumping (PP) techniques, the PRR and stability were determined. To control the PRR and maintain high stability of the Q-

switched pulses, an enhanced pulsed pumping technique was proposed to automatically control the pump power.

In section 2, the literature review of the studies discussing the different techniques to reduce the time jitter are presented. The rate equations of the Yb:YAG laser Q-switched by Cr⁴⁺:YAG as saturable absorber are provided in section 3. The results of continuous and pulsed pumping are discussed in Section 4. Then, the proposed technique of automatic pulsed pumping is represented as well as the resulting PRR and time jitter.

2. Literature Review

As it was mentioned in Section 1, many studies discussed the control of pulse repetition and time jitter through different techniques and schemes.

Many factors contribute to the pulse to pulse time jitter such as the environmental and pump instabilities including the intensity variations, changes in pump spatial and spectral properties as well as the spontaneous nature of passive Q-switching [1] [23]. The environmental and pump instabilities are contingent on the stability of the surroundings and the reliable pumping electronics and laser diodes. Environmental isolation can reduce the time jitter by factor of 5 in the range of μsec [24].

The spontaneous noise is also a major source of instability since the pulse formation depends on the spontaneous emitted photons when the photon flux is close to the lasing condition [3] [23]. For a stable pumping, the stimulated emission is more promoted over the spontaneous one. Therefore, for higher pumping power, the pulse generation can be more stabilized.

Lai et al. had studied the effect of slightly modulating the pump diode power [15]. The repetition rate of a Nd:YAG laser passively Q-switched by Cr⁴⁺:YAG was experimentally shown to reach a time stability of 10⁻⁶ over 10⁶ pulses, short-time period jitter about 1% in less than 1sec, and a slow variation of 6% over a few minutes due to environmental thermal drifts.

However, the modulation of pump power may result in some undesirable dynamical behavior such as periodic and chaotic oscillations [25]. The study carried out by K-G Hong et al, was based on Nd:YVO₄ laser passively Q-switched by Cr⁴⁺:YAG. The stabilization of pulse repetition rate and time jitter was controlled by careful selection of the modulation frequency to match the repetition rate of free running mode otherwise periodic and chaotic behavior may occur.

Also, the effect of modulating the pumping laser diode was also studied in microchip structured Yb:YAG Q-switched laser as well as introducing a Brewster polarizer in order to maintain linear polarization [5]. The time jitter was drastically decreased from μsec to nsec range.

An alternative technique to control the pulse repetition rate and time jitter was changing the transmission of the saturable absorber by optical bleaching. Klimov et al. [9] experiment were conducted using a diode pumped Nd:YAG laser while controlling the orientation of the Q-switch element around its optical axis.

Another technique of saturable absorber bleaching is applying external optical modulation to the saturable absorber [3]. The modulated output of 910 nm laser diode was injected into the Cr:YAG saturable absorber to alter



its population difference and hence its transmission. The modulation frequency has been chosen to match the free running repetition rate. The time jitter was reduced by a factor of 2.5.

Instead of applying optical modulation, a direct bleaching of the Cr:YAG saturable absorber was involved [1]. A 1036 nm laser diode bar was driven to trigger a 920 W bleaching pulse of 15 μ sec to turn the cavity loss of the saturable absorber to a lower lasing threshold. With careful selection of the triggering time, the time jitter was reduced by factor of 12 from 241nsec to 20 nsec.

Moreover, an active Q-switched laser bleaching the Cr:YAG saturable absorber of a passively Nd:YAG Q-switched laser has been reported [26]. Sub-nanopulses with 632 psec time jitter have been realized.

The previously mentioned techniques were based on either modulating the pumping laser diode or optical bleaching of the saturable absorber. S. Su [17] had proposed to merge the two techniques while considering the fast switching of the laser diode. Operating the laser diode in two conditions; less than and close to the threshold value as a prepumping of the active medium, the time jitter is reduced from the range of μ sec to 150 nsec.

The reflectivity and the length of the lasing cavity are of the design parameters that can contribute to the control of the Q-switched output pulse [23]. Kausas et al, have proposed to extend the lasing cavity with a coupled cavity of the same length of the initial cavity to match their free spectral range. The coupled cavity is realized by an additional mirror mounted on a piezoelectric transducer. By changing the position of the additional mirror, to switch the gain thresholds between high and low, the pulse generation can be controlled and hence the time jitter (from 190 nsec to 24 nsec).

The active medium of Q-switched lasers can play a role in the control of the output pulses. Some authors changed the host of active ions from Nd:YAG to Nd:YVO₄ [17] and from crystalline form to ceramic one [26,27]. In this work, Yb:YAG active lasing medium is chosen.

For further control of the pulse generation, the systems can migrate to more complicated configurations such as using master/slave lasing cavities [28], hybrid active and passive Q-switched lasers [17], mixing Q-switched with mode-locked mechanisms [29] and moving to optical fiber laser configurations [30].

3. Rate Equations

According to the passively Q-switched laser theory [4,10,31], the modified coupled rate equations of photon density and population inversion density of gain medium and the saturable absorber in the passively Q-switched resonator, which include the excited-state absorption of the saturable absorber, the pump term and the population reduction factor of the laser, are given by:

$$\frac{d\phi}{dt} = \frac{\phi}{t_r} \left[2\sigma N l - 2\sigma_g n_g l_s - 2\sigma_e n_e l_s - \ln\left(\frac{1}{R}\right) - L \right] \quad (1)$$

$$\frac{dN}{dt} = -\gamma \sigma c \phi N - \frac{n}{\tau} + W_p \quad (2)$$

$$\frac{dn_g}{dt} = -\sigma_g c \phi n_g + \frac{n_{s0} - n_g}{\tau_s} \quad (3)$$

$$n_g + n_e = n_{s0} \quad (4)$$

where ϕ is the photon density in the laser cavity,	
t_r the cavity round-trip time ($t_r = 2l/c$) of laser cavity of optical length l ,	
σ the stimulated emission cross-section of the laser crystal,	
σ_g the absorption cross-section of ground state of the saturable absorber,	
σ_e the absorption cross-section of the excited state,	
N the population inversion density of the gain medium,	
n_g and n_e the absorber ground state and excite state population density respectively,	
n_{s0} the total population density of the saturable absorber,	
l the length of the laser crystal,	
l_s the length of the saturable absorber,	
R the reflectivity of the output coupler,	
L the nonsaturable intracavity round-trip dissipative optical loss,	
W_p the volumetric pump power,	
c the speed of the light,	
γ the inversion reduction factor ($\gamma = 2$ for Yb ³⁺ -doped three-level solid state lasers),	
τ the lifetime of the upper laser level of the gain medium	
τ_s the excited-state lifetime of the saturable absorber.	

The relationship between the population density in the atomic level '1' (n_{s1}) and the total population density (n_{s0}) of the saturable absorber can be given by [4]

$$n_{s1}/n_{s0} = (N/n_i)^\alpha \quad (5)$$

where α describes the relative strength of the absorption transitions of the laser active medium and the saturable absorber ($\alpha = \sigma_e/\gamma\sigma$) and n_i is the threshold population inversion density in the active medium at which the Q-switched pulse is initiated, given by

$$n_i = \frac{\ln(1/R) + 2\sigma_g n_{s0} l_s + L}{2\sigma l} \quad (6)$$

By solving the rate equations altogether, the population inversion density (n_t) at peak power and the final population inversion density (n_f) of the obtained Q-switched pulse can be described by the following transcendental equations:

$$\frac{n_t}{n_i} = \frac{n_{t0}}{n_i} + \left(1 - \frac{n_{t0}}{n_i}\right) \left(\frac{n_t}{n_i}\right)^\alpha \quad (7)$$

$$1 - \frac{n_f}{n_i} + \frac{n_{t0}}{n_i} \ln\left(\frac{n_f}{n_i}\right) \left(1 - \frac{n_{t0}}{n_i}\right) \frac{1}{\alpha} \left(1 - \left(\frac{n_f}{n_i}\right)^\alpha\right) = 0 \quad (8)$$

where $\delta = \sigma_e/\sigma_g$ and n_{t0} is defined by

$$n_{t0} = \frac{\ln(1/R) + \delta \ln(1/T_0^2) + L}{2\sigma l} \quad (9)$$

The peak power $P(t)$ then can also be determined by

$$P(t) = \frac{h\nu A l}{\gamma \tau_r} \ln\left(\frac{1}{R}\right) \phi_{max} \quad (10)$$

While the laser pulse energy (E) is expressed as



$$E = \frac{h\nu A l}{\gamma \tau_r} \ln\left(\frac{1}{R}\right) \ln\left(\frac{n_i}{n_f}\right) \quad (11)$$

Thus, the pulse width can be calculated from

$$t_p = E/P(t) \quad (12)$$

By solving Equation (1) at steady-state, the total loss can be given by:

$$Loss = \frac{2\sigma_g n_g l_s + 2\sigma_e n_e l_s + \ln(1/R) + L}{2\sigma l} \quad (13)$$

In the case of continuous pumping, the pumping term W_p is considered as a constant value. While in the case of pulsed pumping, the pumping term will be modified to a rectangular pulse train as shown in Figure 1, where T is the period of pumping cycle, p_w is on duty time and md is the modulation depth. However, the continuous pumping can be regarded as a special case of pulsed pumping when $md=0$.

The time between two successive Q-switched pulses can be denoted by τ_{pp} . For N pulses, the PRR can be calculated from the average of these times τ_{av} as

$$PRR = \frac{1}{\tau_{av}} \quad (14)$$

The time jitter between pulses can be also obtained by calculating the time deviation of the generated Q-switched pulsed from the average time τ_{av} . The time jitter can be considered as an indication of the time stability of the generation of the Q-switched pulses.

$$jitter = \langle |\tau_{pp} - \tau_{av}| \rangle \quad (15)$$

Hence, the time instability can be determined by the ratio between the jitter and the average time,

$$instability = \frac{\langle |\tau_{pp} - \tau_{av}| \rangle}{\tau_{av}} \quad (16)$$

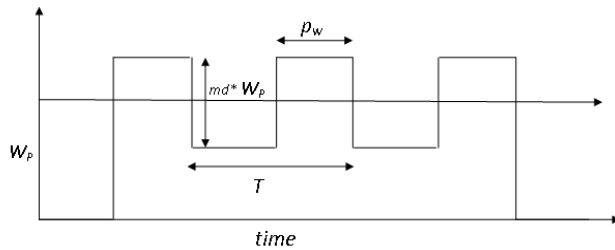


Figure 1. Rectangular Pulse train form of pulsed pumping in PP technique

4. Simulation Results

The coupled rate equations (1) to (3) are solved numerically using 4th order Runge–Kutta method. The spectral parameters of 10% at Yb:YAG passively Q-switched using Cr⁴⁺:YAG are listed in Table (1) [32]. Figure 2 shows the numerical stimulation results of the first four pulses. The first pulse was obtained after 197 μ sec, while the following pulses were generated with average time τ_{av} of 202 μ sec and the free running pulse repetition rate of 4.95 KHz. The peak power can be determined from Equation (12), where the pulse width is 15.2 ns (from Figure 3) and pulse energy is 117 μ J (from Equation (11)). Thus, the calculated peak power is 7.7 KW.

Figure 3 illustrates the first generated Q-switched laser pulse. When the photon density inside the laser cavity

increases, the loss decreases accordingly as a result of the bleaching effect of Cr⁴⁺:YAG saturable absorber. When the population inversion density becomes equal to the cavity loss, the photon density attains its peak value then decreases as long as the population inversion density is decreased. Figure 4 represents the normalized volumetric pump power ($W_{pn}(t)$), the normalized photon density ($\phi_n(t)$) and the normalized population inversion density of gain medium ($N_n(t)$) in the case of $md=0$, which corresponds to the continuous pumping case. The calculated PRR is ≈ 5 KHz while the jitter is 3.2×10^{-11} sec corresponding to time instability of 1.6×10^{-7} .

Table 1. The spectral parameters of Yb:YAG passively Q-switched using Cr⁴⁺:YAG.

Symbol	Value
σ	$2.3 \times 10^{-20} \text{ cm}^2 @ 1030 \text{ nm}$
l	0.4 cm
c	$3 \times 10^{10} \text{ cm/sec}$
σ_g	$3.2 \times 10^{-18} \text{ cm}^2 @ 1.06 \mu\text{m}$
σ_e	$4.5 \times 10^{-19} \text{ cm}^2 @ 1.06 \mu\text{m}$
l_s	0.94 mm
n_{s0}	$0.87 \times 10^{17} \text{ ions/cm}^3$
R	85%
T_0	97%
l'	5.2 cm
γ	2
W_p	$1.12 \times 10^{23} \text{ sec}^{-1} \text{ cm}^{-3}$
$h\nu_p$	$2.112 \times 10^{-19} \text{ Joule}$
τ	951 μ sec
τ_s	3.4 μ sec
$h\nu$	$1.93 \times 10^{-19} \text{ Joule}$
C_{yb}	$13.8 \times 10^{20} \text{ ions/cm}^3$ (10 at.%)
L	8%
α	10 cm^{-1}

The effect of pulsed pumping on the generation of output pulses is studied for different pumping parameters; the period T , the duty cycle p_w and the modulation depth md . Since the average time between pulses is larger than 200 μ sec, a pulsed pumping of period $T=300$ μ sec and duty cycle of 250 μ sec was first applied. Then, the period was fixed and the duty cycle was decreased to 200 μ sec then 175 μ sec. All the different cases are studied for different modulation depths $md=0.25, 0.5, 0.75, 1$. A special condition of modulation depth is when the pumping is operated in ON-OFF pumping scheme.

Figure 5.a shows the ON-OFF pumping case. Since the ON-time of the first period is 250 μ sec which is larger than the first Q-switched laser pulse produced in the continuous pumping case, the first generated pulse is also generated at 202 μ sec.

Due to the discontinuity of the pumping (OFF-time) during 50 μ sec, the next pulses are generated with τ_{av} 260 μ sec, PRR of 3.8 KHz and jitter 1.56×10^{-5} sec corresponding to time instability of 6%. Using different modulation depths, ($md=0.25, 0.5, 0.75$ and 1), it can be noticed that the PRR has increased up to its double value for $md=1$ while the stability has shown a degradation as the jitter increased by order of 6 with respect to continuous pumping



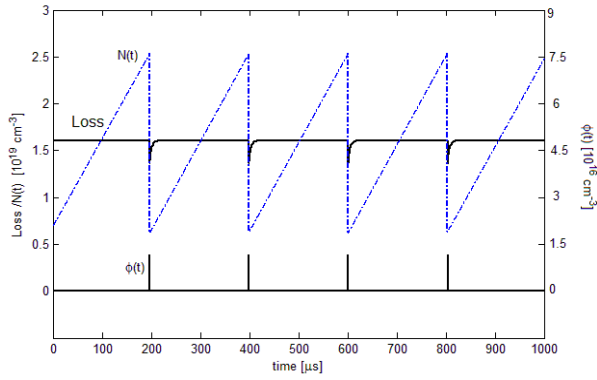


Figure 2. Population inversion density $N(t)$, total loss of laser cavity (Loss) and photon density ($\phi(t)$)

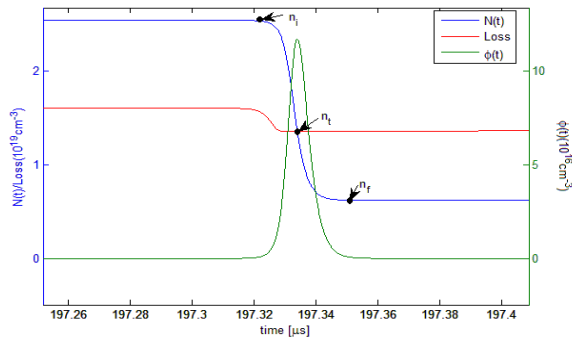


Figure 3. Population inversion density $N(t)$, total loss of laser cavity (Loss) and photon density, ($\phi(t)$) at the first Q-switched pulse.

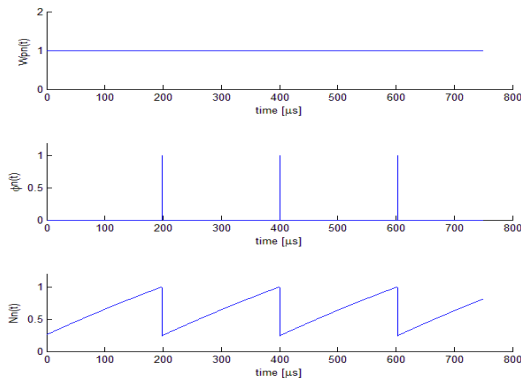


Figure 4. The normalized volumetric pump power ($W_p(t)$), the normalized photon density ($\phi_n(t)$) and the normalized population inversion density of gain medium ($N_n(t)$) in the case of continuous pumping ($md=0$)

The variation of PRR, jitter time and instability can be explained from the temporal behavior of population inversion density of gain medium $N_n(t)$ for each modulation depth, as shown in Figure 5.a After generation of the first Q-switched pulse, the remaining ON-time in the duty cycle allows the growth of the population inversion density but cannot acquire the threshold value (n_i) before the end of ON-time duration. During the OFF-time, the population remains almost constant until the beginning of the second period of the pumping and the population restarts to grow to generate the second Q-switched pulse.

The rate of increase of the population inversion density during the OFF-time is inversely proportional to the modulation depth; as the modulation depth increases, the value of the pumping is decreased. Therefore, the rate at which population inversion density increases is slower than that of the smaller modulation depths. The case of

ON-OFF pumping represents a special case of pulsed pumping, into which during the OFF-time, the pumping is turned off and the population inversion density decreases rather than increases as in other pulsed pumping cases in which the pumping is not turned off. Depending on the modulation depth of the pulsed pumping, the time required for the generation of the Q-switched pulse decreases with the increase of the modulation depth and the pulse repetition rate is increased. Therefore, the ON-time of the pumping may allow generating more than one Q-switched pulse in the same period.

Keeping the period of pulsed pumping $T=300\mu\text{sec}$, while varying the duty cycle from $250\mu\text{sec}$ to $200\mu\text{sec}$ then to $175\mu\text{sec}$, the PRR and time jitter have been studied and the results are shown in Figures. 6 and 7, respectively. It can be seen that PRR is proportional to the modulation depth as well as the duty cycle duration. On the other hand, the stability decreases drastically for ON-OFF pumping cases then becomes more stable in $md=0.25$ case and decreases again when $md=0.5, 0.75$ and 1 . However, the jitter increases with the decrease of the duty cycle time and the stability increases.

The effect of the period of the pulsed pumping has been also studied. The period is decreased from $300\mu\text{sec}$ to $150\mu\text{sec}$ with different duty cycles. The resulting PRR and time jitter values for all cases are summarized in Table 2.

It can be seen that within the same pump period, as the duty time decreases the PRR decreases due to decreasing of the pump time and results in the decrease of the amount of optical pumping delivered to the active medium during the pumping period, (i.e. decrease the average pump power). This occurs for all modulation depths. For example if the period is $250\mu\text{sec}$, and the modulation depth is 0.5 , the PRR decreases from 5.8 to 4.94 kHz as the duty time decreased from 200 to $125\mu\text{sec}$.

Also, it can be observed that within the same pumping period and the same duty cycle, the PRR increases with increasing the modulation depth since more pumping power is gained by the active medium. If $250\mu\text{sec}$ is chosen and $150\mu\text{sec}$ duty time, the PRR increases 5.1 to 5.78 kHz when increasing the modulation depth.

If the duty time is remained constant and the period is decreased, the PRR increases since the OFF-time decreases and the average pump power delivered to the active medium increases. For a $200\mu\text{sec}$ duty time and modulation depth 0.75 , the PRR is increased from 5.93 to 7 kHz as the period is decreased from 300 to $225\mu\text{sec}$.

On the other hand, if the time jitter is examined, it can be seen that with the same pump period the time jitter increase with decreasing the duty time which means that the system is less stable. This behavior is maintained for all modulation depths. While if the pump period and duty time are kept constant and time jitter increases with the increase of modulation depth. Keeping a constant duty time, the time jitter is decreasing with the pump period decrease for all modulation depths. In general, it can be seen that the minimum values of time jitter occur at modulation depth 0.25 while the PRR is close to the free running case. This can be explained that the change of



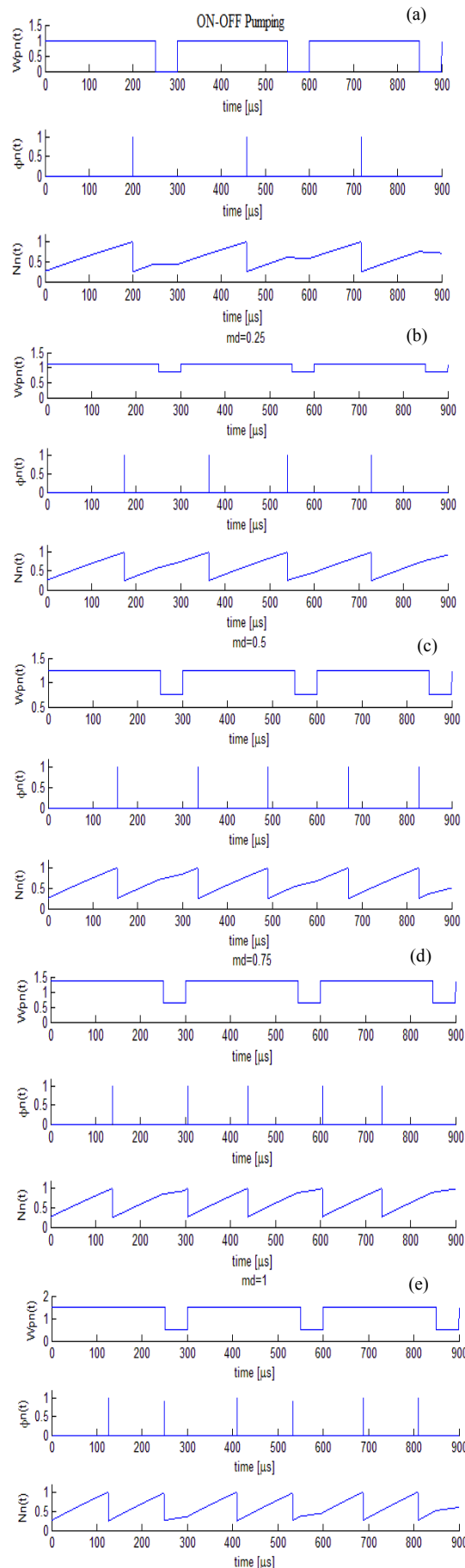


Figure 5. $W_{pn}(t)$, $\phi_n(t)$ and $N_n(t)$ in the case of pulsed pumping at $T=300$ μsec and 250 μsec duty cycle (a) ON-OFF pumping, (b) $md=0.25$, (c) $md=0.5$, (d) $md=0.75$, and (e) $md=1$.

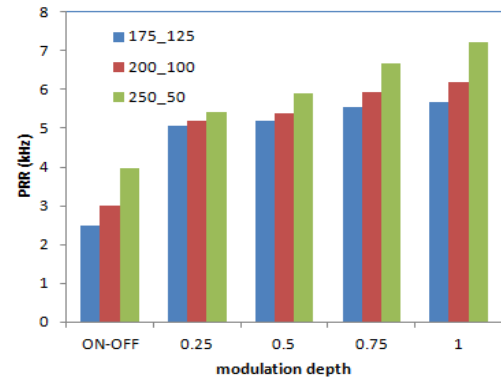


Figure 6. The PRR versus modulation depth ($T=300\mu\text{sec}$)

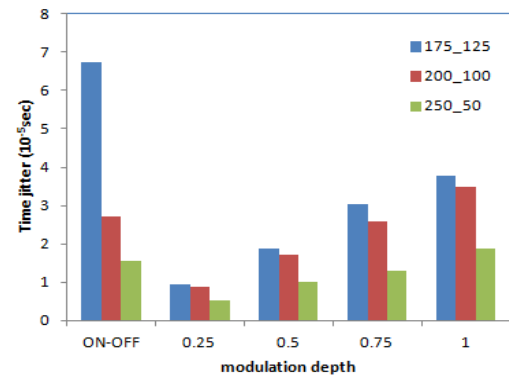


Figure 7. The time jitter versus modulation depth ($T=300\mu\text{sec}$)

The pumping power with small values keep the situation as close as the original case.

To summarize, the minimum time jitter was obtained with period 200 μsec , duty cycle 100 μsec and modulation depth $md=0.25$ corresponding to time instability of 5.5×10^{-4} , but the PRR is less than free running value. The highest PRR can be obtained when the pulsed pumping has period $T=225$ μsec , duty cycle 200 μsec and modulation depth $md=1$, however, the time jitter is increased to 9.27 μsec and corresponding instability 0.07.

Although the pulsed pumping technique can be used to increase the PRR, however, the degradation of the stability was a drawback. In order to increase the stability of the output pulses, we proposed a new scheme to control the pumping so that once the laser pulse is generated, it is detected and the pumping is stopped for a previously determined off time.

After the off time duration, the pumping is restarted to attain the required the population inversion density and the process of pulse generation is to recommence. This technique can be denoted by Automatic Pulsed Pumping (APP) technique as shown in Figure 8. Herein, a 10 μsec OFF-time is proposed and modulation depths vary from 0.25 to 1 by steps of 0.25. In addition, the ON-OFF pumping case is also considered.

In the first case of ON-OFF pumping, the first Q-switched laser pulse is generated at 217 μsec as shown in Figure 9.a. Once the pulse is detected, the pumping is switched off for the predetermined time (10 μsec) into which the detection and control times are considered. After the OFF-time, the pumping is switched ON to generate the next Q-switched pulse and the process will



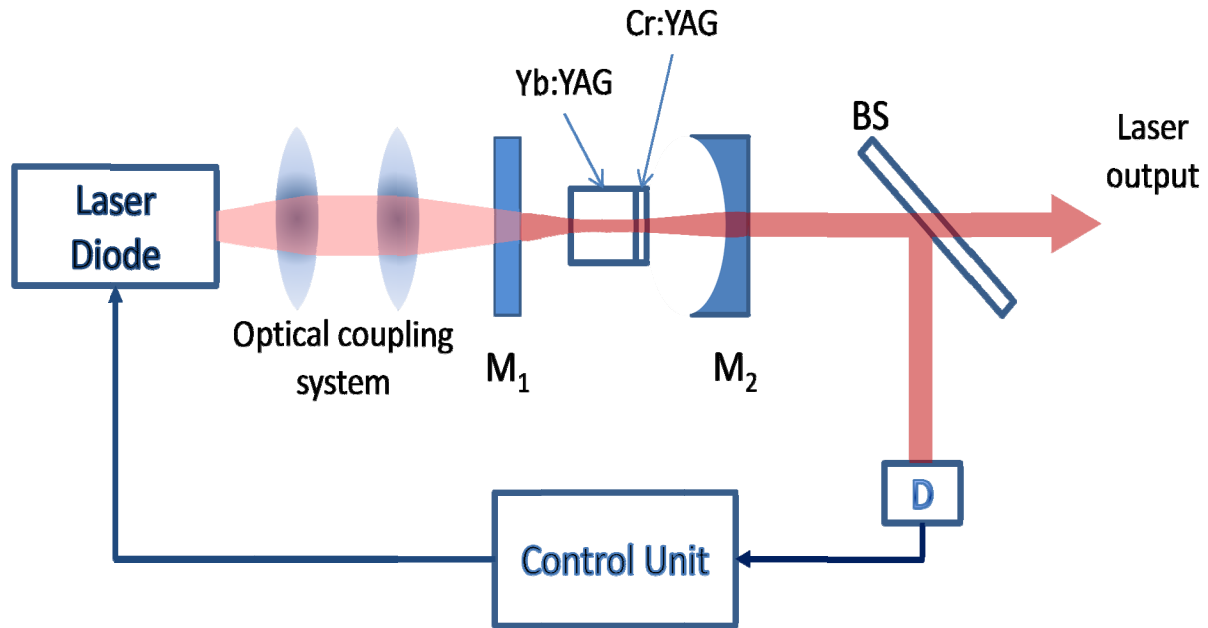


Figure 8. The proposed setup of automatic pulsed pumping system

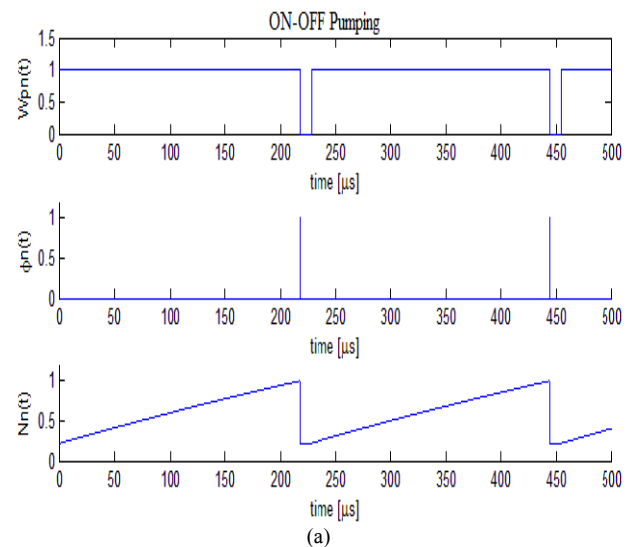
Table 2. The PRR and time jitter of pulsed pumping technique.

T (μ s)	Duty (μ s)	ON-OFF		md=0.25		md=0.5		md=0.75		md=1	
		PRR (kHz)	jitter (10^{-6})	PRR (kHz)	jitter (10^{-6})	PRR (kHz)	jitter (10^{-6})	PRR (kHz)	jitter (10^{-6})	PRR (kHz)	jitter (10^{-6})
300	250	3.96	15.6	5.43	5.35	5.9	10.2	6.67	13.1	7.23	18.6
	200	3	27	5.2	8.75	5.4	17	5.93	26	6.2	35
	175	2.5	67.5	5.06	9.3	5.2	18.8	5.55	30.3	5.68	37.6
250	200	3.78	9.1	5.4	4.2	5.8	8.75	6.58	13.8	7	16.3
	150	2.65	59.7	5.1	5.9	5.23	12.3	5.6	19.8	5.78	28.6
	125	2	2.1	4.95	5.9	4.94	11.7	5.13	18	5.15	26.7
225	200	4.3	3.75	5.5	1.91	6.1	4.1	7	6.7	7.6	9.27
	175	3.58	21.4	5.34	2.97	5.74	6.9	6.46	12.5	6.87	15.5
200	150	3.48	29.8	5.3	1.31	5.66	4.1	6.32	8.47	6.67	12
	100	2.02	67	4.99	0.11	5.03	1.27	5.01	2.45	5.02	4.9
150	100	2.98	24.7	5.2	3.65	5.42	6.2	5.94	7.48	6.21	5.68
	75	2.02	41.1	4.94	4.84	4.94	9.85	5.15	14	5.15	18.8

continue automatically. The PRR and the jitter of the generated Q-switched pulses are calculated. The PRR is 4.4 kHz and the jitter is about 2.1×10^{-11} sec. Although the PRR has been decreased, it can be seen that the time jitter is in the same order of the continuous pumping and the time instability is in the order of 10^{-7} .

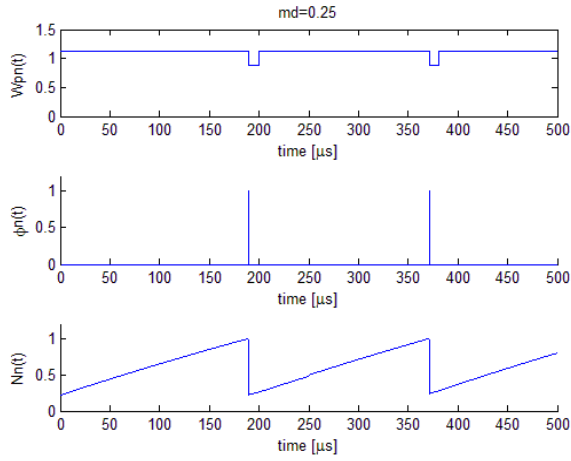
When the modulation depth of the automatic pulsed pumping varies from 0.25 to 1, the PRR is increased to 7.14 kHz as shown in Figure 10. On the other hand, the jitter is slightly affected but is maintained within the same order of 10^{-11} sec (Figure 11). Therefore, the automatic pulsed pumping has combined the advantages of controlling the PRR while keeping the system stability. This can be explained as during the ON and OFF timing of pulsed pumping, the photon flux and population inversion density are not starting and ending at the same values. While in the automatic pulsed pumping, the OFF-time starts just after the detection of the Q-switched pulse and dominates for a predetermined time. Thus, the population inversion density exhibits the same decay and growth before starting a new pumping period in the case of ON-OFF pumping or different modulation depths, respectively. Hence, each pulse is subjected to similar

initial conditions and exhibits the same response providing stable Q-switched pulses.

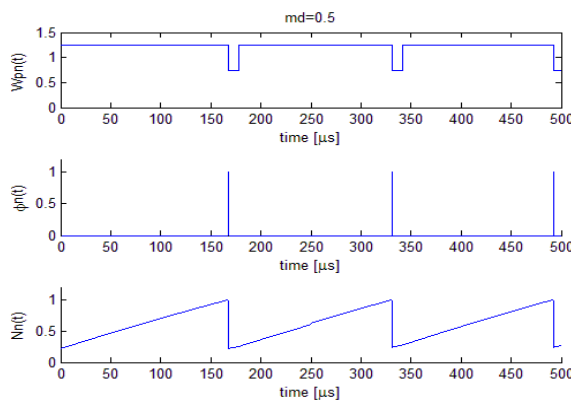


(a)

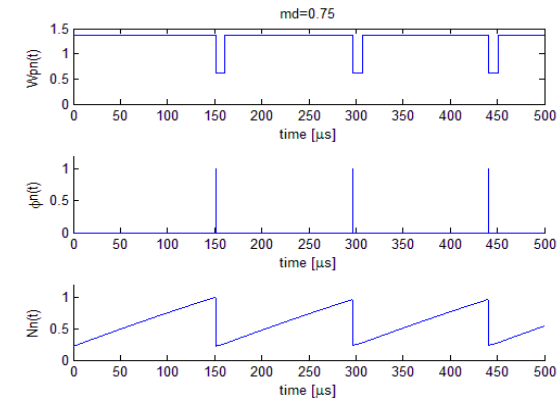




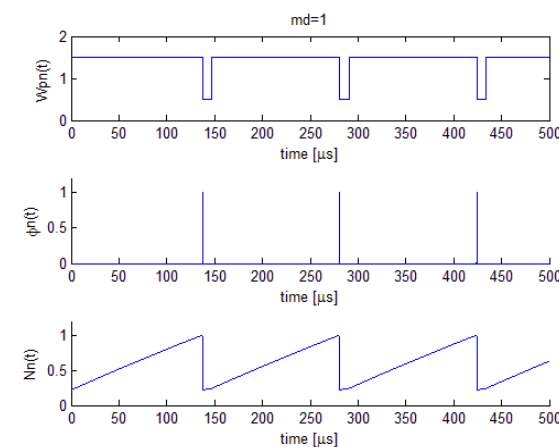
(b)

Figure 9. APP numerical result: (a) ON-OFF pumping, (b) $md=0.25$, (c) $md=0.5$, (d) $md=0.75$, and (e) $md=1$.

(c)



(d)



(e)

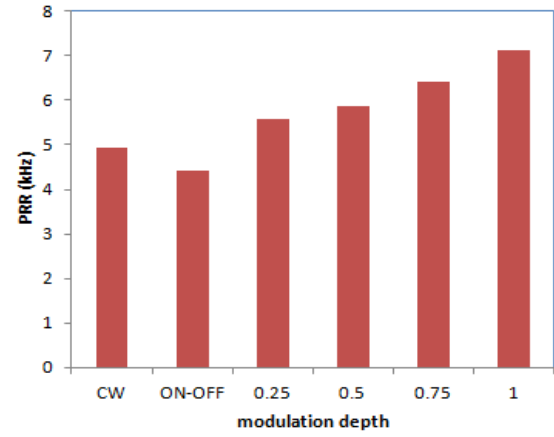
Figure 9. *cont.*

Figure 10. The PRR versus modulation depth.

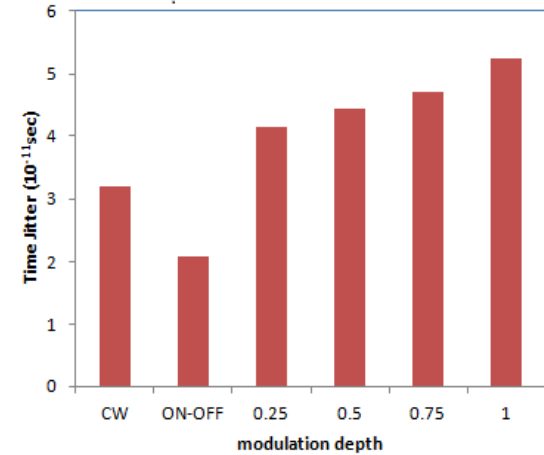


Figure 11. The time jitter versus modulation depth

5. Conclusion

In conclusion, the pulse repetition rate PRR, time jitter and the time instability of the Q-switched laser pulses have been numerically investigated when different pumping techniques are applied. The system under investigation was Yb:YAG laser passively Q-switched by Cr^{4+} :YAG as saturable absorber. The free running PRR is close to 5 kHz, the peak power 7.7 kW, pulse energy 117 μJ and pulse width 15.2 nsec.

The PRR can be controlled by using pulsed pumping technique. The PRR can be increased from 5 kHz in the case of continuous pumping to 7.6 kHz when different modulation depths are applied. However, the stability of the laser pulses has been decreased since the time jitter increased by order of 6 (from 10^{-11} to 10^{-5} sec).

A simplified technique has been proposed to control the PRR as well as keeping high stability. The technique is based on the automatic control of the pulsed pumping so that once the Q-switched pulse is generated, the system automatically switches the pump status. The pumping power is switched off in the case ON-OFF pumping or decreased according to the modulation depth which varies from 0.25 to 1. Hence, the technique can be nominated by automatic pulsed pumping technique. A PRR of 7.14 kHz has also been obtained while maintaining the time jitter in the order of 10^{-11} sec as in the continuous pumping case. Therefore, the system operates in high repetition rate while keeping the stability of pulse to pulse generation.



As future work, the numerical model can be extended to include the spatial distribution and the longitudinal variation of the photon density in order to investigate the thermal behavior for proposed pumping techniques and compare it with the previous work for continuous pumping. In addition, the automatic pulsed pumping technique can be experimentally implemented in order to validate the results of the numerical simulation.

6. References

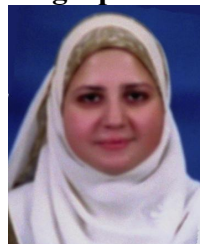
- [1] B. Cole, L. Goldberg, C. W. Trussell, A. Hays, B. W. Schillign and C. McIntoch, "Reduction of timing jitter in a Q-switched Nd:YAG laser by directly bleaching of a Cr⁴⁺:YAG saturable absorber", *Opt. Express*, Vol. 17, No. 3, pp. 1766-1771, Feb. 2009.
- [2] J. A. Morris, and C. R. Pollock "Passive Q switching of a diode-pumped Nd:YAG laser with a saturable absorber", *Opt. Lett.*, Vol. 15, No. 8, pp. 440-442, 1990.
- [3] S-L Hyang, T-Y Tsui, C-H. Wang and F-J. Kao, "Timing jitter reduction of a passively Q-switched laser", *Jpn J. Appl. Phys*, Vol. 38, Part. 2, No. 3A, pp. L239-241, 1999.
- [4] X. Zhang, S. Zhao, Q. Wang, Q. Zhang, L. Sun, S. Zhang, "Optimization of Cr⁴⁺-doped saturable absorber Q-switched lasers", *IEEE J. of Quantum Electron.*, Vol. 33, No. 12, pp. 2286-2294, 1997.
- [5] R. L. Schmitt and B. T. Do. "Design and performance of a high-repetition-rate single-frequency Yb:YAG microlaser", *Proc. of SPIE*. 6871, Solid State Lasers XVII: Technology and Devices, 687105, 2008.
- [6] J. Alcock, "The Cr⁴⁺:YAG Laser at 25 Years: A Review of the Promise, Progress, and Limitations of this Broad Gain Bandwidth 1.5 nm Laser Medium", *IEEE Photon. Soc. Lett.*, pp. 14-17, June 2013.
- [7] Q.-L. Zhang, B.-H. Feng, D.-X. Zhang, P.-M. Fu, Z.-G. Zhang, Z.-W. Zhao, P.-Z. Deng, J. Xu, X.-D. Xu, Y.-G. Wang, X.-Y. MA, "Diode-Pumped Passively Q-Switched Yb:YAG Microchip Laser with a GaAs as Saturable Absorber", *Chin. Phys. Lett.*, Vol. 20, No. 10, pp. 1741-1743, 2003.
- [8] W. Tian, C. Wang, G. Wang, S. Liu, and J. Liu, "Performance of diode-pumped passively Q-switched mode-locking Nd:GdVO₄/KTP green laser with Cr⁴⁺:YAG", *Laser Phys. Lett.*, Vol. 4, No. 3, pp. 196-199, 2007.
- [9] I. V. Klimov, I.A.Shcherbakov and V.B. Tsvetkov, "Control of the Nd-laser output by Cr-doped Q-switches", *Laser Phys.*, Vol. 8, No. 1, pp 232-237, 1998.
- [10] M. E. Jazi, M. D. Baghi, M. Hajimahmodzadeh, M. Soltanolkotabi, "Pulsed Nd:YAG passive Q-switched laser using Cr⁴⁺:YAG crystal", *Optics & Laser Technol.*, Vol. 44, pp. 522-527, 2012.
- [11] A. V. Kir'yanov, V. Aboites, and N. Il'ichev, "Neodymium laser Q-switched with a Cr⁴⁺:YAG crystal: control over polarization state by exterior weak resonant radiation", *Laser Phys.*, Vol. 10, No. 2, pp. 461-466, 2000.
- [12] M. Lu, C.R.Chatwin, R. C. D. Young, and P. M. Birch, "Numerical simulation of a CW-pumped Cr:YAG passively Q-switched Yb:YAG pulsed laser", *Opt. and Lasers in Engineer.*, Vol. 47, pp. 617-621, 2009.
- [13] T. Li, S. Zhang, S. Zhao, K. Yang, Z. Zhuo, "Thermal modeling of the continuous-wave end-pumped Q-switched lasers," *Optics Commun.*, Vol. 283, No. 15, pp. 3070-3075, 2010
- [14] J. M. El-Azab, H. M. Kandel, M. A.Khedr, and H. M. El-Ghandoor, "Numerical Study of Transient Temperature Distribution in Passively Q-Switched Yb: YAG Solid-State Laser", *Opt. and Photon. Journal*, Vol. 4, pp. 46-53, 2014.
- [15] N. D. Lai, M. Brunel, F. Bretenaker, and A. L. Floch, "Stabilization of the repetition rate of passively Q-switched diode-pumped solid-state lasers", *Appl. Phys.*, Vol. 79, pp. 1073-1075, 2001.
- [16] A. Sennaroglu. "Solid-state lasers and applications", CRC Press, USA, 2007.
- [17] S. Wu, "Accurate timing of passive Q-Switch lasers", *Proc. of SPIE* 6216, Laser Source and System Technology for Defense and Security II, 62160S, May 12, 2006.
- [18] K. Battou, O. Ziane, K. Ait-Ameur, "Modelling of a Nd:YAG laser Q-switched by a scanning interferometric mirror", *Opt. Commun.*, Vol. 281, pp. 696-704, 2008.
- [19] D.S. Sumida, T.Y. Fan, "Effect of radiation trapping on fluorescence lifetime and emission cross section measurements in solid-state laser media", *Opt. Lett.*, Vol.19, pp. 1343-1345,1994.
- [20] M. Tsunekane, and T. Taira, "High peak power passively Q-switched Yb:YAG/Cr:YAG micro-lasers", *IEEE J. Quantum Electron.*, Vol. 49, No.5, pp. 454 - 461, 2013.
- [21] S.L. Yellin, A.H. Shepard, R.J. Dalby, J.A. Baumaum, H. B. Serreze, T. S. Guide, R. Solarz, K. J. Bystrom, C. M. Harding, R. G. Walters, "Reliability of GaAs-based semiconductor diode lasers: 0.6-1.1 μm ", *IEEE J. Quantum Electron.*, Vol. 29, pp. 2058-2067, 1993.
- [22] H. Chu, S. Zhao, K. Yang, Y. Li, D. Li, G. Li, J. Zhao, W. Qiao, X. Xu, J. Di, L. Zheng, J. Xu. "Experimental and theoretical study of passively Q-switched Yb:YAG laser with GaAs saturable absorber near 1050 nm," *Optics & Laser Technol.*, Vol. 56, pp.398-403, 2014.
- [23] Q. Li, B. Feng, Z. Zhang, T. Zhang, "Direct numerical simulation of quasi-three-level passive Q-switched laser", *Optics Commun.*, Vol. 284, pp. 3391-3398, 2011.
- [24] A. Kausas and T. Taira, "Timing jitter control by scanning coupled cavity in passively Q-switched Nd:YVO₄/Cr:YAG laser", in *Advanced Solid State Lasers,OSA, Ath2A.40*, 2014.
- [25] M. W. Smillie, M.Silver, S. T. Lee, T.J. Cook, "High single pulse energy, passively Q-switched Nd:YAG laser for defence applications", *Proc. of SPIE*, 8959, Solid State Lasers XXIII: Technology and Devices, 89590Z, Feb. 28, 2014.
- [26] K.-G. Jong and M-D Wei, "Dynamical behavior in the passive Q-switched Nd:YVO₄ laser with pump



modulation”, International Symposium on Physics and Applications of Laser Dynamics 2012 (IS-PALD 2012), pp. 25-26, Nov. 7-9, 2012

- [27] H. Chan, S. Wang, S. Lin, and A. H. Kung, “Sub-Nanosecond Timing Jitter in a Passively Q-Switched Microlaser by Active Q-Switched Laser Bleaching,” in *CLEO Pacific Rim*, pp. 2–3, 2013.
- [28] Y. Tan, Q. Luan, F. Liu, F. Chen, and J.R. Vásques de Aldana, “Q-switched pulse laser generation from double-cladding Nd:YAG ceramics waveguides”, *Opt. Express*, Vol. 21, No. 16, pp. 18963-18968, Aug. 2013.
- [29] J. Dong, K. Ueda, A. Shirakawa, H. Yagi, T. Yanagitani, and A. A. Kaminskii, “ Composite Yb: YAG/Cr⁴⁺:YAG ceramics picoseconds microchip lasers”, *Opt. Express*, Vol. 15, No. 22, pp. 14516-14523, 29 Oct. 2007.
- [30] F. F. Wu, “A low jitter single frequency Q-switched laser from solid state to optical fiber configuration”, *Proc. of SPIE 85991, Solid State Lasers XXII: Technology and Devices*, 85991X, 2013.
- [31] F.J. Grawert, F. Ö. Ilday, D. F. Kielinski, J.T. Gopinath, G. S. Petrich, L. A. Kolodziejski, E. P. Ippen and F. X. Kärtner, “ Automatic feedback control of an Er-doped fiber laser with an intracavity loss modulator”, *Opt. Lett.*, Vol. 39, No. 9, pp.1066-1068, May 2005.
- [32] B. Dussardeier, J. Maria, P. Peterka, “Passively Q-switched Ytterbium and Chromium all-fibre laser”, 10th International Conference on Fiber Optics and Photonics, Guwahati, India, HAL- 00732319, Dec. 2010

Biographies



Jala El-Azab was born in Cairo, Egypt in 1975. Graduated from Faculty of Engineering, Electronics and Electrical Engineering Dept. , Cairo University. Received both the M.Sc. degree in nonlinear semiconductor laser diodes in 2002 and the Ph.D. degree in chaotic semiconductor laser engineering in 2006 from National Institute of Laser Enhanced Sciences, Cairo University. Working on modeling semiconductor laser diodes, chaotic optical communications, optical networks, photonic crystal fibers, optical logic gates and holography applications.



Hamed M. Kandel was born in Cairo, Egypt in 1980. Graduated from Faculty of Science, Chemistry & Physics Dept., Cairo University in 2001. Received both the M.Sc. degree in theoretical study of X-ray laser in 2008 and the Ph.D. degree in short pulse solid-state laser modeling in 2014 from National Institute of Laser Enhanced Sciences, Cairo University. Working on theoretical study of laser systems, ultra-short laser pulse generation and control, generation of new laser wavelengths in XUV and X-ray range.



Mohamed A Khedr was born in Kalubia, Egypt in 1956. Graduated from Faculty of Science, Physics Dept., Tanta University in 1978. Received both the M.Sc. in the physical phenomena of vacuum arc discharge in 1990 and Ph.D. degrees in the micro hollow cathode discharge using Laser and mass spectroscopy in 1995 from physics Dept., Faculty of science Cairo University. Working in the dept. of Laser Science and its Interaction with Matter National Institute of Laser Science Cairo University. Fields of interest; tunable ultrafast laser systems, optical parametric oscillators, thin films, infrared optical detectors, Laser plasma Acceleration.

